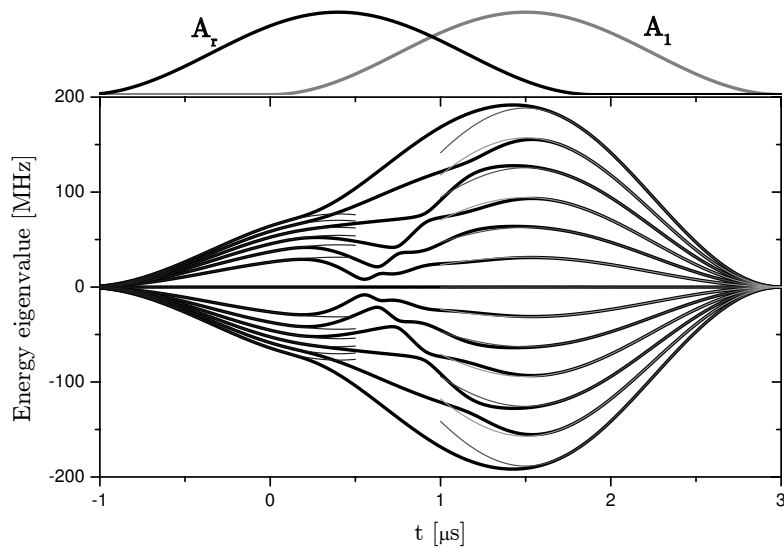


Adiabatic Processes in Quantum Computation

-Experimental and theoretical studies



Ditte Møller

PhD Thesis
May 2008

Lundbeck Foundation Theoretical Center for Quantum System Research
Department of Physics and Astronomy, University of Aarhus

This thesis is submitted to the Faculty of Science at the University of Aarhus, Denmark, in order to fulfil the requirements for obtaining the PhD degree in Physics. The studies were carried out under supervision of Associate Professor Lars Bojer Madsen and Professor Klaus Mølmer in the Lundbeck Foundation Theoretical Center for Quantum System Research at the Department of Physics and Astronomy.

Preface

This thesis is based on four years of PhD studies at the Department of Physics and Astronomy, University of Aarhus. The first years were spent in the Ion Trap Group under the supervision of Michael Drewsen and Jens Lykke Sørensen. The investigations considered quantum logic with trapped laser cooled $^{40}\text{Ca}^+$ -ions with the main focus on internal state detection using adiabatic processes. Theoretical studies of adiabatic processes were the subject of the final two PhD years and took place under the supervision of Lars Bojer Madsen and Klaus Mølmer. My supervisors deserve the greatest thank for sharing their insight in, and enthusiasm for the complexity of the quantum world.

I have had the privilege of being a part of the experimental ion trap group as well as the Lundbeck Foundation Theoretical Center for Quantum Research and I would like to thank all friends and colleagues at the Department for fruitful scientific discussions and excellent company. Finally, I would like to acknowledge Uffe Vestergaard Poulsen, Peter Fønss Herskind and Anders Peter Sloth for proofreading this thesis.

Ditte Møller
May, 2008

List of publications

- [I] Jens L. Sørensen, Ditte Møller, Theis Iversen, Jakob B. Thomsen, Frank Jensen, Peter Staantum, Dirk Voigt, and Michael Drewsen
Efficient coherent internal state transfer in trapped ions using stimulated Raman adiabatic passage.
New J. Phys. **8**, 261 (2006).
- [II] Ditte Møller, Lars Bojer Madsen, and Klaus Mølmer
Geometric phase gates based on stimulated Raman adiabatic passage in tripod systems.
Phys. Rev. A **75**, 062302 (2007).
- [III] Ditte Møller, Jens L. Sørensen, Jakob B. Thomsen, and Michael Drewsen
Efficient qubit detection using alkaline-earth-metal ions and a double stimulated Raman adiabatic process.
Phys. Rev. A **76**, 062322 (2007).
- [IV] Ditte Møller, Lars Bojer Madsen, and Klaus Mølmer
Geometric phases in open tripod systems.
Phys. Rev. A **77**, 022306 (2008).
- [V] Ditte Møller, Lars Bojer Madsen, and Klaus Mølmer
Quantum gates and multi-particle entanglement by Rydberg excitation blockade and adiabatic passage.
Phys. Rev. Lett. **100**, 170504 (2008).

Contents

1	Introduction	1
1.1	Quantum computation	1
1.2	Outline	5
2	Adiabatic processes	7
2.1	Geometric phases	8
2.2	Stimulated Raman adiabatic passage	11
2.3	Optimising the STIRAP efficiency	16
2.4	Summary	21
3	Geometric phase gates	23
3.1	Geometric phase and STIRAP	23
3.2	Geometric phase gates	24
3.3	Conclusion	36
4	Geometric phases of an open system	37
4.1	Evolution of an open system	37
4.2	Non-Hermitian no-jump evolution	40
4.3	Jump evolution	44
4.4	Fidelity of Hadamard gate	46
4.5	Conclusion	50
5	Entangling Rydberg atoms	51
5.1	Rydberg atoms	51
5.2	Entangling two atoms	55
5.3	Many-particle entanglement	60
5.4	Conclusion	64
6	Quantum computation with $^{40}\text{Ca}^+$	65
6.1	Requirements	65
6.2	Internal state detection	68
6.3	Summary	69

7	Experimental setup	71
7.1	Overview	71
7.2	Laser cooling of $^{40}\text{Ca}^+$	73
7.3	Photoionisation	75
7.4	Laser systems	76
7.5	Imaging system	82
7.6	Ion storage	82
7.7	Magnetic fields	87
8	STIRAP experiments	89
8.1	Optical pumping	89
8.2	Setup and timing of STIRAP experiments	91
8.3	Delay scan	93
8.4	Frequency scan	96
8.5	The first STIRAP process	97
8.6	Conclusion	98
9	Summary and Outlook	99
9.1	Dansk resumé	100
	Appendices	101
A	Principles of numerical simulations	103
A.1	The Schrödinger equation	103
A.2	Density matrix	105
B	Properties of $^{40}\text{Ca}^+$	109
B.1	Characteristics	109
B.2	Rabi frequencies	110
C	Measurements of laser phase fluctuations	113
	Bibliography	117

Chapter 1

Introduction

The non-local and non-deterministic nature of quantum mechanics challenges our classical intuition, but it also opens the door to a magically well-defined mathematical description of the microscopic world, and enables us to explain phenomena which can not be understood classically. Despite its success in describing what we measure in the laboratories, the counter-intuitive nature of quantum mechanics has provoked decades of debate about its interpretation. Experimentalists now perform experiments on small quantum systems like a single atom or photon and thereby investigate the intriguing quantum world. Recent progress is so great that the non-classical correlations of quantum mechanics can be exploited for a wide range of applications with impact outside the laboratories. Quantum cryptography guarantees secure exchange of information and quantum computation brings algorithms which outshine their classical counterparts. This first introductory chapter briefly presents the key concepts of quantum computation and describe the experimental and theoretical progress on implementations in various physical systems. Based on the introduction, we outline the contents of the thesis.

1.1 Quantum computation

While the computer industry is discovering the limits of classical computation, the quantum computer brings new and more efficient algorithms using the parallelism of quantum superposition. The development of quantum computers started in the nineteen-eighties with the first ideas for exploiting the parallelism of quantum mechanics for computations [1,2], and gained strength with the proposals of quantum algorithms which could outperform their classical counterparts [3,4]. During the last decades many different physical implementations of a large scale quantum computer have been suggested and experimental progress has been achieved in various schemes. Here, we give a brief introduction to the concepts, but a careful review of quantum computation can be found in [5].

1.1.1 Qubits, quantum gates and algorithms

The fundamental unit of information in a classical computer, the bit, is represented as either 0 or 1. In a quantum computer the bits are replaced by a quantum system with two states, $|0\rangle$ and $|1\rangle$, which for instance could be different energy levels in an atom. In a classical computer the bits are either 0 or 1, but quantum mechanics allows for the existence of superposition states $c_0|0\rangle + c_1|1\rangle$, where the coefficients are complex numbers that fulfill $|c_0|^2 + |c_1|^2 = 1$. The basic unit in quantum information is these superposition states, called qubits. They open for a dramatic increase in computational power because with N qubits the computer can be in a superposition of 2^N classical states which in principle can process in parallel.

The catch, though, is the read out of the qubit state. When we measure the state we will find that it is in either $|0\rangle$ or $|1\rangle$ with probability $|c_0|^2$ or $|c_1|^2$, respectively, and the system collapses onto the measured state. This implies that even though the N qubits allow for calculation with 2^N classical states simultaneously, a measurement collapses the system onto one of the 2^N states. In order to exploit the parallelism of quantum mechanics, algorithms must be

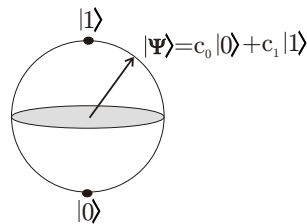


Figure 1.1: The state of the qubit, $c_0|0\rangle + c_1|1\rangle$, can be represented as an arrow on the Bloch sphere.

created in a clever way such that the power achieved by the parallelism is not lost when a result is read out of the computer. Today only a few efficient quantum algorithms have been proposed including the famous Grover search algorithm [3], which efficiently searches for elements in an unordered database, and Shor's algorithm for factorising large composite numbers into primes [4].

As in classical computation the quantum algorithms can be decomposed into gates acting on either one or two qubits. A set of gates, from which all algorithms can be created, is called universal and could for example consist of one-qubit phase gates, a one-qubit Hadamard gate and either a two-qubit controlled-NOT or a two-qubit controlled phase gate. The actions of these gates are sketched in Fig. 1.2.

1.1.2 Entanglement

The two-qubit gates rely on the existence of entanglement - a pure quantum resource. A composite quantum system of two qubits, A and B , is entangled

$$\begin{array}{ll}
 |0\rangle \rightarrow |0\rangle & |0\rangle \rightarrow \frac{1}{\sqrt{2}}(|0\rangle + |1\rangle) \\
 |1\rangle \rightarrow e^{i\varphi_1}|1\rangle & |1\rangle \rightarrow \frac{1}{\sqrt{2}}(|0\rangle - |1\rangle)
 \end{array}$$

(a) One-qubit phase gate.

(b) One-qubit Hadamard gate.

$$\begin{array}{ll}
 |00\rangle \rightarrow |00\rangle & |00\rangle \rightarrow |00\rangle \\
 |01\rangle \rightarrow |01\rangle & |01\rangle \rightarrow |01\rangle \\
 |10\rangle \rightarrow |11\rangle & |10\rangle \rightarrow |10\rangle \\
 |11\rangle \rightarrow |10\rangle & |11\rangle \rightarrow e^{i\varphi_2}|11\rangle
 \end{array}$$

(c) Two-qubit C-NOT gate.

(d) Two-qubit controlled phase gate.

Figure 1.2: Quantum gates in the one-qubit basis $\{|0\rangle, |1\rangle\}$ or two-qubit basis $\{|00\rangle, |01\rangle, |10\rangle, |11\rangle\}$.

when their wave function cannot be separated in a product of wave functions of each system, $|\psi\rangle_{AB} \neq |\psi\rangle_A |\psi\rangle_B$. Entanglement means a correlation between physical observables of the two qubits. As an example, the state $|\psi\rangle_{AB} = |0\rangle_A |0\rangle_B + |1\rangle_A |1\rangle_B$ is maximal entangled. If we measure the state of qubit A we will get either $|0\rangle_A$ or $|1\rangle_A$ with probability $1/2$ and the wave function of the composite system will collapse to $|0\rangle_A |0\rangle_B$ or $|1\rangle_A |1\rangle_B$. A subsequent measurement of the state of system B will with certainty yield the same outcome as the measurement of system A . These non-classical correlations are an essential property of quantum mechanics and have led to discussion within the physics community about the completeness of the theory. The studies of entanglement are of fundamental interest, and during the recent decades entanglement has also been used as a resource in many fields of physics, among others quantum cryptography, teleportation, metrology and computation [5].

1.1.3 Building a large scale quantum computer

Building a large scale quantum computer is not trivial, since it requires very precise control over small quantum systems. Various systems have been proposed and are being explored as physical implementations. These systems include nuclear-magnetic-resonances (NMR) [6, 7], linear optics [8], trapped atoms [9, 10] or ions [11] and solid states system including quantum dots [12] and super conducting devices [13]. To enable a comparison of the different systems David DiVincenzo defined five criteria, that a system must fulfil to

ensure implementation of quantum computation [14].

1. *A scalable system with well characterised qubits.*
2. *Ability to initialise the system in a fiducial state.*
3. *A universal set of quantum gates.*
4. *A coherence time of the qubit, which is much longer than gate operation times.*
5. *Qubit-specific measurement.*

	Qubit	Coupling	DiVincenzo Criteria				
			Scalable physical system	Initialisation	Long coherence time	Universal set of gates	Read out
Trapped Ions	Electronic or hyperfine states	Quantised vibrational or cavity field modes	☒	✓	✓	✓	✓
NMR	Nuclear spins of atoms in a designer molecule	RF pulses and chemical bonds between atoms	÷	☒	✓	✓	☒
Neutral Atoms	Hyperfine states	Dipole-dipole interaction or cavity field modes	☒	✓	✓	☒	☒
Linear optics	Polarisation of a single photon	Beam splitters and measurements	☒	☒	✓	☒	☒
Quantum dot	Electron spin	Magnetic field and columb blockade	☒	✓	☒	☒	✓
Super conducting	Quantised flux or charge in superconducting circuit	Currents and/or magnetic fields	☒	✓	☒	☒	✓

✓ Demonstrated experimentally ☒ Theory proposals available ÷ No proposals available

Figure 1.3: Scheme showing the present state of different physical implementations of quantum computation.

Fig. 1.3 shows the progress of some of the most advanced physical implementations. A more detailed discussion of the different implementations can be found in the quantum computation roadmap [15]. Each physical system has advantages and disadvantages. The implementations based on trapped atoms (ions or neutrals) have the advantage of isolated systems with long coherence time and gates with high fidelity are achieved in these well-controlled systems. However, the scaling is very challenging for trapped ions or neutrals. The solid state systems may be easier to scale, but there is at present problems achieving a sufficient coherence time. It is an open question which system will be superior and it is likely that a large scale quantum computer will be a combination of different physical systems.

1.2 Outline

This concludes the brief introduction to quantum computation. The topic of the thesis is adiabatic processes and the advances they may bring to quantum computation. A system controlled by slowly varying external parameters has time to adapt to the changes. A process fulfilling this is said to be adiabatic and in **chapter 2** we will describe the concept of adiabaticity more precisely and present a criterion for determining when a quantum process is adiabatic. Furthermore, the geometric phases acquired during an adiabatic evolution will be defined and the adiabatic process used throughout this thesis, stimulated Raman adiabatic passage (STIRAP), is described.

The first part of the thesis presents theoretical studies. **Chapter 3** shows how the geometric phase acquired by a quantum system subject to STIRAP can be used to create a universal set of quantum gates. In **chapter 4** one of these gates, the Hadamard gate, is considered when the quantum system is open and therefore subject to dephasing. In **chapter 5** we focus on a specific implementation of quantum computation and describe how neutral atoms with a highly excited electron, so-called Rydberg atoms, can be used for quantum computation. We present a method to create two-qubit gates as well as many-particle entanglement.

In the second part we turn to experimental studies and in **chapter 6** another candidate for implementation of quantum computation, namely trapped laser cooled ions, is presented. We describe a scheme for detection of internal spin states in $^{40}\text{Ca}^+$. The detection scheme is based on two STIRAP processes and the experimental studies in **chapter 7** and **8** show how one of these transfers population efficiently between two internal states. **Chapter 7** gives a view over the experimental setup and **chapter 8** presents the results.

The main ideas and results of the thesis are summarised in the conclusion and Danish summary (Dansk resumé) of **chapter 9**.

Chapter 2

Adiabatic processes

Adiabatic processes are investigated in many fields of physics, where the external perturbation of the system varies so slowly that the system has time to adapt to the changes in the perturbation¹. In general, a system defined by variables changing on a timescale T_i under influence of external variables changing on a timescale T_e undergoes adiabatic evolution when $T_i \ll T_e$ [16]. The Foucault pendulum, for instance, has an internal timescale given by its oscillation time. The earth slowly varies the position of the pendulum's support on a timescale which is much slower than the oscillation time of the pendulum. The motion of the pendulum is therefore not affected; only the oscillation plane changes gradually. If the earth starts rotating very fast or if you by hand rapidly shakes the support of the pendulum the adiabaticity will be broken and its motion will be altered.

In quantum mechanics, adiabatic processes are very interesting because they can be used to steer systems into desired states in a potentially robust manner. The first relevant question is of course, when the evolution of a quantum system is adiabatic. The answer is put forward in the adiabatic theorem [17] proved first in [18]. For non-degenerate eigenvalues it can be stated as,

A quantum system initially in an instantaneous eigenstate of a time-dependent Hamiltonian will remain in the same eigenstate, when the Hamiltonian varies slowly compared to the energy gap between eigenstates.

In terms of the instantaneous eigenstates $\psi_n(t)$ and their corresponding eigenvalues $E_n(t)$ the criterion for an adiabatic evolution can be written as [17],

$$\left| \left\langle \psi_m \left| \frac{d\psi_n}{dt} \right\rangle \right| \ll \frac{|E_n - E_m|}{\hbar} . \quad (2.1)$$

¹In thermodynamics a process is called adiabatic when no energy is transferred between the system and its environment

When the eigenvalues are degenerate, adiabaticity only ensures that the system stays within the eigenspace of the initial eigenvalue. The evolution within this eigenspace is then derived by applying the Schrödinger equation as discussed below.

2.1 Geometric phases

When the adiabatic criterion is fulfilled, the evolution of a quantum system with non-degenerate eigenvalues can be described by a following of the eigenstates and a calculation of the phases acquired by each eigenstate. In the degenerate case we must calculate the evolution within the eigenspace populated. In both scenarios, two contributions can be distinguished. Dynamic phases which depend explicitly on the time evolution of the Hamiltonian and geometric phases which depend on the geometry of the space spanned by the controlling parameters.

2.1.1 Non-degenerate eigenvalues

We first consider a system in an eigenstate $\psi_n(t)$ corresponding to the non-degenerate eigenvalue $E_n(t)$. The adiabatic theorem states that the system will remain in $\psi_n(t)$, but may acquire a phase. One contribution to this is the dynamic phase, which is simply given by the time integral of the energy,

$$\theta_n(t) = -\frac{1}{\hbar} \int_{t_i}^t E_n(t') dt'. \quad (2.2)$$

For adiabatic processes an additional geometric phase contribution was brought into focus in 1984 by M. Berry [19]. Berry proved its existence by assuming that a phase, $\gamma_n(t)$, is acquired in addition to the dynamic one,

$$\Psi(t_i) = \psi_n(t_i) \rightarrow \Psi(t) = \psi_n(t) e^{i(\theta_n(t) + \gamma_n(t))}. \quad (2.3)$$

The evolution is given by the Schrödinger equation,

$$\begin{aligned} H\psi_n e^{i(\theta_n + \gamma_n)} &= i\hbar \frac{d}{dt} \left(\psi_n e^{i(\theta_n + \gamma_n)} \right) \Rightarrow \\ E_n \psi_n e^{i(\theta_n + \gamma_n)} &= (i\hbar \dot{\psi}_n - \hbar \dot{\theta}_n \psi_n - \hbar \dot{\gamma}_n \psi_n) e^{i(\theta_n + \gamma_n)} \Rightarrow \\ E_n \psi_n &= (i\hbar \dot{\psi}_n - \hbar \dot{\theta}_n \psi_n - \hbar \dot{\gamma}_n \psi_n), \end{aligned} \quad (2.4)$$

where the dot denotes a derivative with respect to time. From (2.2) we find $\dot{\theta}_n = -E_n/\hbar$ and (2.4) reduces to,

$$\dot{\gamma}_n \psi_n = i\dot{\psi}_n. \quad (2.5)$$

Taking the inner product with ψ_n then yields,

$$\dot{\gamma}_n = i\langle \psi_n | \dot{\psi}_n \rangle. \quad (2.6)$$

If the inner product $\langle \psi_n | \dot{\psi}_n \rangle$ is non-zero an additional phase will be acquired. This phase is called Berry's phase or the geometric phase, because the phase has a geometric interpretation as seen from the following convenient rewriting: The time dependence of $\psi_n(t)$ can be viewed as a dependence of time varying parameters, $\bar{R}(t)$, controlling the Hamiltonian and we write $\psi_n(\bar{R}(t))$. The time derivative is now expressed as,

$$\frac{\partial \psi_n(\bar{R}(t))}{\partial t} = \nabla_{\bar{R}} \psi_n \frac{d\bar{R}}{dt}, \quad (2.7)$$

and the phase is found by integrating (2.6),

$$\gamma_n(t) = i \int_{t_i}^t \langle \psi_n | \nabla_{\bar{R}} \psi_n \rangle \frac{\partial \bar{R}}{\partial t'} dt' = i \int_{\bar{R}(t_i)}^{\bar{R}(t)} \langle \psi_n | \nabla_{\bar{R}} \psi_n \rangle d\bar{R}. \quad (2.8)$$

While the dynamic phase in (2.2) depends strongly on the elapsed time, the additional phase γ_n , on the contrary, is independent of the time and only relies on the path traversed in the parameter space spanned by $\bar{R}(t)$. This geometric nature of Berry's phase is particularly apparent for a cyclic evolution, where the system returns to the initial state after some time T and the geometric phase is a path integral around a closed loop,

$$\gamma_n(T) = i \oint \langle \psi_n | \nabla_{\bar{R}} \psi_n \rangle d\bar{R}. \quad (2.9)$$

The three dimensional cyclic geometric phase has a classical analogue, called the Hannay angle [20], acquired for instance by the Foucault pendulum.

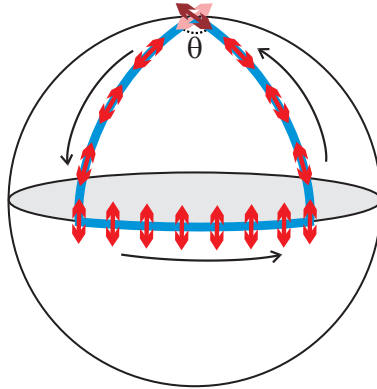


Figure 2.1: Parallel transport of a pendulum oscillating in the direction of the red arrows around the blue cyclic route on the earth. Initially, the pendulum swings in the direction of the light red arrow on the North Pole, but when it returns to the North Pole again it swings in the direction of the dark red arrow and the oscillation plane has been rotated an angle $\Theta = A/R^2$ defined by the enclosed area, A , and the radius of the earth, R .

If we first imagine a pendulum swinging in some direction at the North Pole indicated by the light red arrow in Fig. 2.1 and then move its support around the earth following for example the closed blue loop the oscillation plane will follow the red arrows. When the pendulum returns to the North Pole it no longer swing in its original plane - the oscillation plane is rotated an angle determined by the area enclosed by the loop, or more precisely the solid angle subtended. This is exactly an example of the Hannay angle [16]. The Foucault pendulum does not move, but instead the earth rotates making the pendulum acquire a Hannay angle, rotating the oscillation plane of the pendulum.

2.1.2 Degenerate eigenvalues

For degenerate eigenvalues transfer may occur between eigenstates with the same eigenvalue even when adiabaticity is maintained and the Berry phase is replaced by a unitary transformation between the degenerate eigenstates [21, 22]. A system initially in the eigenspace spanned by eigenstates ψ_k corresponding to the eigenvalue E will remain in the same eigenspace when the evolution is adiabatic and the wave function can be written,

$$\Psi = e^{i\theta} \sum_k c_k \psi_k, \quad (2.10)$$

where all eigenstates acquire the same dynamic phase, θ . Inserting (2.10) into the Schrödinger equation yields the evolution,

$$\begin{aligned} H\Psi &= i\hbar\dot{\Psi} \Rightarrow \\ e^{i\theta} E \sum_k c_k \psi_k &= \sum_k e^{i\theta} \left(i\hbar\dot{c}_k \psi_k - \hbar\dot{\theta} c_k \psi_k + i\hbar\dot{\psi}_k c_k \right) \Rightarrow \\ E \sum_k c_k \psi_k &= \sum_k \left(i\hbar\dot{c}_k \psi_k + E c_k \psi_k + i\hbar\dot{\psi}_k c_k \right) \Rightarrow \\ \sum_k \dot{c}_k \psi_k &= \sum_k -\dot{\psi}_k c_k. \end{aligned} \quad (2.11)$$

Taking the inner product with ψ_m gives the differential equations,

$$\dot{c}_m = - \sum_k c_k \langle \psi_m | \dot{\psi}_k \rangle. \quad (2.12)$$

The single phase acquired in the non-degenerate case derived in (2.6) is thus replaced by a matrix connecting the initial and final state.

2.1.3 Geometric quantum computation

Geometric phases only depend on the path traversed in the parameter space. They are therefore expected to be less sensitive to noise than the dynamic

phases, but to what extent this holds true is still an open question. As an illustration we consider the closed loop phase (2.9) in the three dimensional case, where it can be rewritten as a surface integral,

$$\gamma_n(T) = i \int \nabla_R \times \langle \psi_n | \nabla_{\bar{R}} \psi_n \rangle d\bar{a}. \quad (2.13)$$

The first thing to note is that the integral does not depend on the speed of the process. In addition, as long as the area enclosed is kept constant, the integral will be insensitive to small variations in the path traversed. This leads to the conclusion that geometric phases are typically robust with respect to fluctuations in the controlling parameters [23,24]. Robustness against environmental noise leading to decoherence is less obvious and proof has only been given for certain kinds of noises and systems [25,26].

The robust features of the geometric phases, anticipated by the theoretical investigations discussed above, may be used to improve the fidelities of quantum gates. So-called geometric or holonomic quantum computation [27] is build of gates relying on geometric phases. Proposals for holonomic quantum computation is available in trapped ion [28–30], neutral atom [31], linear optics [32], NMR [33] and solid state [34] systems. Experimentally, gates have been implemented in ion traps [35], NMR [33] and super conducting systems [36].

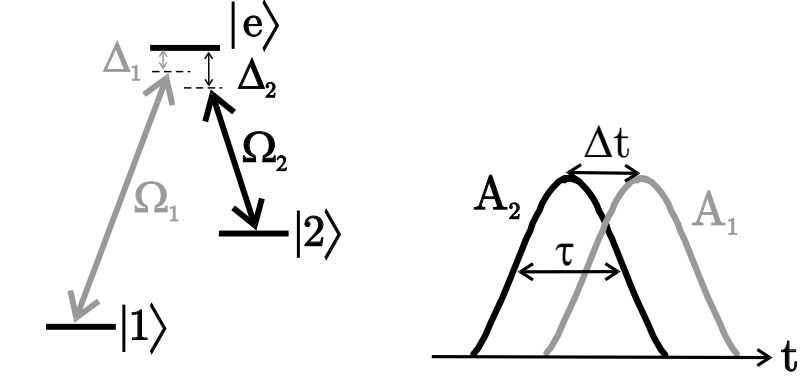
2.2 Stimulated Raman adiabatic passage

Stimulated Raman adiabatic passage (STIRAP) is a robust way of adiabatically transferring population from one quantum state to another and enables us to make the transfer state selective, coherent and efficient. The adiabaticity also ensures controllable geometric phases making STIRAP a promising tool for creation of robust geometric gates in quantum computation. We present the STIRAP theory that will be used throughout the thesis as a basis for the geometric gate suggestions as well as in a proposal for detection of the internal state of a trapped ion. A thorough review of STIRAP was presented in [37].

2.2.1 STIRAP theory

STIRAP is performed by application of two laser fields to a system with a lambda level structure as shown in Fig. 2.2(a). Two coherent laser pulses transfer the population from one quantum state, $|1\rangle$, via an intermediate state $|e\rangle$ to another state, $|2\rangle$. In the Rotating Wave Approximation (RWA) we can express the instantaneous Hamiltonian of the system in the $\{|1\rangle, |e\rangle, |2\rangle\}$ -basis [37, 38] as

$$H(t) = \frac{\hbar}{2} \begin{bmatrix} 0 & \Omega_1^*(t) & 0 \\ \Omega_1(t) & 2\Delta_1 & \Omega_2(t) \\ 0 & \Omega_2^*(t) & 2(\Delta_1 - \Delta_2) \end{bmatrix}. \quad (2.14)$$



(a) Three level lambda-system coupled with two laser fields with Rabi frequencies Ω_1 and Ω_2 detuned Δ_1 and Δ_2 with respect to resonance.

(b) Pulse sequence used for the STIRAP process consisting of two pulses applied in a counter-intuitive order with delay, Δt , and pulse width, τ .

Figure 2.2

The Rabi frequencies, Ω_1 and Ω_2 , describe the coupling strength between the states and are calculated from experimental parameters (see Appendix B). The detunings are the difference between the transition frequencies and the laser frequencies, $\Delta_i = \frac{E_i - E_e}{\hbar} - \omega_{i,\text{laser}}$. The Rabi frequencies are described by the real amplitudes of the fields, $A_1(t)$ and $A_2(t)$, and the relative phase between the fields, $\varphi_2(t)$,

$$\begin{aligned}\Omega_1(t) &= A_1(t), \\ \Omega_2(t) &= A_2(t)e^{-i\varphi_2(t)}.\end{aligned}\quad (2.15)$$

Diagonalising $H(t)$ analytically is not straight forward and requires division into many different parameter regimes, but the solutions can be found in [39]. Here, we will only consider two-photon resonance ($\Delta_1 = \Delta_2$). In this case we find eigenvalues [37],

$$\omega^\pm = \frac{1}{2} \left(\Delta_1 \pm \sqrt{\Delta_1^2 + A_1^2 + A_2^2} \right), \quad \omega^D = 0, \quad (2.16)$$

and instantaneous eigenstates,

$$\begin{aligned}|D\rangle &= \cos \theta |1\rangle - \sin \theta e^{i\varphi_2(t)} |2\rangle, \\ |+\rangle &= \sin \theta \sin \phi |1\rangle + \cos \phi |e\rangle + \cos \theta \sin \phi e^{i\varphi_2(t)} |2\rangle, \\ |-\rangle &= \sin \theta \cos \phi |1\rangle - \sin \phi |e\rangle + \cos \theta \cos \phi e^{i\varphi_2(t)} |2\rangle,\end{aligned}\quad (2.17)$$

with $\tan \theta(t) = \frac{A_1(t)}{A_2(t)}$ defining the mixing angle, θ , and $\tan \phi = \sqrt{\frac{\omega_-}{\omega_+}}$. $|D\rangle$ is called a dark state because it does not absorb or emit photons. In terms of Rabi frequencies the dark state reads,

$$|D(t)\rangle = \frac{A_2(t)}{\sqrt{A_1^2(t) + A_2^2(t)}}|1\rangle - \frac{A_1(t)}{\sqrt{A_1^2(t) + A_2^2(t)}}e^{i\varphi_2(t)}|2\rangle. \quad (2.18)$$

With all population initially in $|1\rangle$ and only field 2 applied we start out in $|D\rangle$. Changing the amplitudes of the fields $A_1(t)$ and $A_2(t)$ adiabatically ensures that all population remains in $|D\rangle$. Increasing $A_1(t)$ while decreasing $A_2(t)$ transfers the population from $|1\rangle$ to $|2\rangle$. A counter-intuitive pulse sequence, where the pulse of the second field arrives before the pulse of the first, is shown in Fig. 2.2(b) and does exactly as we request. If the evolution is not perfectly adiabatic, population will be lost to $|+\rangle$ and $|-\rangle$ and therefore to the excited state $|e\rangle$, from where it could be lost due to spontaneous emission. To avoid this diabatic transfer the adiabatic criterion (2.1) states that the coupling between $|D\rangle$ and $|+\rangle$ or $|-\rangle$ must be small compared to the energy-splitting of the states,

$$\left| \left\langle \pm \left| \frac{d}{dt} \right| D \right\rangle \right| \ll |\omega^\pm - \omega^D|. \quad (2.19)$$

The coupling, $|\langle \pm | \frac{d}{dt} | D \rangle|$, corresponds to $|\frac{d\theta}{dt}|$ [40], which can be averaged for smooth laser pulses to give [37],

$$\left| \frac{d\theta}{dt} \right|_{av} = \frac{\pi}{2\mathcal{T}} \quad (2.20)$$

where \mathcal{T} is the duration of the pulse sequence from $\theta = 0$ until $\theta = \pi/2$. Combining (2.20) and (2.19) yields the criterion,

$$|\omega^\pm| \mathcal{T} = \frac{1}{2} \left| \Delta \pm \frac{1}{2} \sqrt{\Delta_1^2 + A_1^2 + A_2^2} \right| \mathcal{T} \gg 1. \quad (2.21)$$

The criterion can be fulfilled by many different pulse shapes and in this work we use either Gaussian

$$\begin{aligned} A_1(t) &= A_{1,\max} e^{-\left(\frac{t}{\tau/2}\right)^2} \\ A_2(t) &= A_{2,\max} e^{-\left(\frac{t+\Delta t}{\tau/2}\right)^2} \end{aligned} \quad (2.22)$$

or \sin^2 pulses

$$\begin{aligned} A_1(t) &= \begin{cases} A_{1,\max} \sin^2\left(\frac{\pi t}{2\tau}\right) & \text{if } 0 < t < 2\tau \\ 0 & \text{otherwise} \end{cases} \\ A_2(t) &= \begin{cases} A_{2,\max} \sin^2\left(\frac{\pi(t+\Delta t)}{2\tau}\right) & \text{if } -\Delta t < t < 2\tau - \Delta t \\ 0 & \text{otherwise} \end{cases} \end{aligned} \quad (2.23)$$

In both cases Δt is the delay between the two pulses while the pulse width τ is defined as the full width at $1/e$ of maximum for the Gaussian pulses and the full width at half maximum (FWHM) for \sin^2 pulses.

2.2.2 Maintaining adiabaticity

Adiabatic processes are obtained by a large energy splitting and slowly varying pulses. Fig. 2.3 considers two pulse sequences. One, where the peak Rabi frequencies are $A_{1,\max} = A_{2,\max}/2\pi = 20$ MHz and the duration of the sequence is $\mathcal{T} \approx 12$ μs (left column) and another with weaker Rabi frequencies $A_{1,\max} = A_{2,\max}/2\pi = 10$ MHz, and shorter pulses with $\mathcal{T} \approx 6$ μs (right column). The laser fields are on resonance, the pulses are Gaussian and their time variation is shown in Fig. 2.3(a). The energy difference between the eigenvalues is calculated directly from (2.16) with $\Delta_1 = 0$ and depends only on the Rabi frequency amplitudes. The splitting is halved when the Rabi frequencies are halved as shown in Fig. 2.3(c). The shorter pulses influence the duration of the sequence and cause the slope of the mixing angle, θ , in Fig. 2.3(b) to become steeper. The splitting of the eigenvalues is smaller and the time variation is faster in the right column implying that this situation is less adiabatic. This is also what we see when we propagate the Schrödinger equation and plot the populations in the atomic states in Fig. 2.3(d). To the left no population of $|e\rangle$ is visible, while the situation in the right column populates $|e\rangle$ slightly and the transfer efficiency is reduced by a factor of 10^{-3} . The violation of adiabaticity is more apparent when we look at the population of the dark state in Fig. 2.3(e). We see that even though the diabatic transfer is present during the process, the population of the dark state is almost fully restored. If decay from $|e\rangle$ is introduced diabatic transfer to the bright states are more severe, because they decay and population of the dark state is no longer restored.

2.2.3 Adiabatic elimination

STIRAP can also be understood from adiabatic elimination of the excited state. The Schrödinger equation for the lambda system yields the differential equations for the population amplitudes on two-photon resonance with real Rabi frequencies,

$$\begin{aligned}\dot{c}_1 &= -\frac{1}{2}\Omega_1 c_e, \\ \dot{c}_e &= -\frac{1}{2}\Omega_1 c_1 - \frac{1}{2}\Omega_2 c_2 + \Delta_1 c_e, \\ \dot{c}_2 &= -\frac{1}{2}\Omega_2 c_e.\end{aligned}\tag{2.24}$$

Now assuming $\dot{c}_e = 0$ leads to

$$c_e = \frac{(\Omega_1 c_1 + \Omega_2 c_2)}{2\Delta_1},\tag{2.25}$$

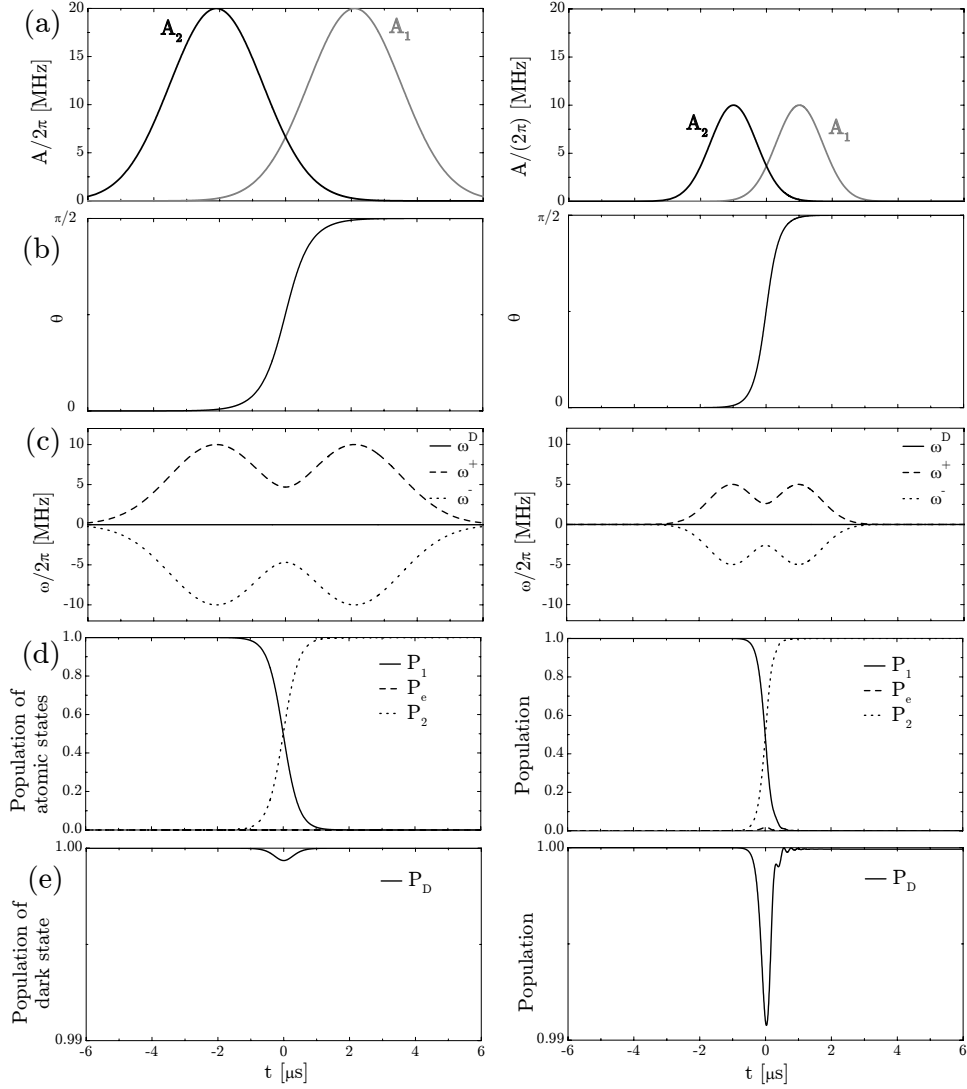


Figure 2.3: Time evolution of the field amplitudes (panel (a)), the mixing angle (panel (b)), the eigenenergies (panel (c)), population in the atomic states (panel (d)), and population in the dark state (panel(e)). The left column shows results for parameters, $A_{1,\text{max}} = A_{2,\text{max}}/2\pi = 20$ MHz, $\Delta t = 4.2$ and $\tau = 4$, while the right column shows results for parameters $A_{1,\text{max}} = A_{2,\text{max}}/2\pi = 10$ MHz, $\Delta t = 2$ and $\tau = 2$.

and substituting (2.25) into (2.24) yields,

$$\begin{pmatrix} \dot{c}_1 \\ \dot{c}_2 \end{pmatrix} = -\frac{1}{4\Delta_1} \begin{pmatrix} \Omega_1^2 & \Omega_1\Omega_2 \\ \Omega_1\Omega_2 & \Omega_2^2 \end{pmatrix} \begin{pmatrix} c_1 \\ c_2 \end{pmatrix}. \quad (2.26)$$

Diagonalising (2.26) gives eigenvalues

$$\omega^B = -\frac{1}{4\Delta_1}(\Omega_1^2 + \Omega_2^2), \quad \omega^D = 0, \quad (2.27)$$

and corresponding eigenstates,

$$\begin{aligned} |D\rangle &= \cos\theta|1\rangle - \sin\theta|2\rangle, \\ |B\rangle &= \sin\theta|1\rangle + \cos\theta|2\rangle, \end{aligned} \quad (2.28)$$

where θ is the mixing angle from the previous section. The dark state, $|D\rangle$, is exactly the dark state found from the full solution, while the bright state, $|B\rangle$, is the superposition of $|+\rangle$ and $|-\rangle$ of (2.17), where $|e\rangle$ is not populated, $|B\rangle = \sin\phi|+\rangle + \cos\phi|-\rangle$. As long as adiabaticity is maintained using adiabatic elimination is a good approach, but as soon as we have some diabatic transfer we need to turn to the full solution to analyse the effect of populating the bright states.

2.3 Optimising the STIRAP efficiency

Achieving a high transfer efficiency using the STIRAP process depends of course on the parameters used. Here, we discuss the influence of the fundamental variables, delay between pulses, one- and two-photon detunings and pulse widths. We will investigate this by propagating the density matrix (see Appendix A), while including decay from $|e\rangle$ as shown in Fig. 2.4. The decay

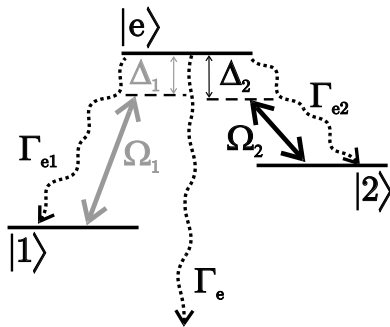


Figure 2.4: Three level lambda-system coupled by two laser fields with Rabi frequencies Ω_1 and Ω_2 detuned Δ_1 and Δ_2 with respect to resonance. Decay rates from the excited state and out of the system is indicated with Γ_e , decay to $|1\rangle$ with Γ_{e1} and decay to $|2\rangle$ with Γ_{e2} . $|1\rangle$ and $|2\rangle$ are assumed stable.

does not influence adiabaticity, but when $|e\rangle$ gets populated, decay increases the error. The parameters used in the following are chosen to match the experimental situation of chapter 6, $\Gamma_e/2\pi = 21.5$ MHz, $\Gamma_{e1}/2\pi = 0.2$ MHz and $\Gamma_{e2}/2\pi = 1.6$ MHz. The simulations solve the density matrix master equation numerically with the Gaussian pulses of (2.22).

2.3.1 Optimal pulse delay and width

The first parameter we investigate is the delay between the two pulses. We show the transfer efficiency as a function of Δt for various peak Rabi frequencies $A_{1,\max} = A_{2,\max}$ in Fig. 2.5. Both laser fields are on resonance. For negative delay corresponding to the intuitive pulse sequence, the pulse of field 1 arrives first and may excite some population but when the pulse of field 2 subsequently arrives the population is repumped from $|2\rangle$ and the transfer efficiency is zero. When the pulses begin to overlap the Raman resonance created induces Rabi oscillations and the transfer efficiency increases. For counter-intuitive pulse sequences the transfer efficiency approaches 1 and an optimal delay is reached at a value depending on the Rabi frequency. For large positive delays the pulses are separated but the Ω_1 pulse arrives last, and it can therefore excite some population to $|e\rangle$, from where some will decay to $|2\rangle$ explaining the plateau in Fig. 2.5. The efficiency at the plateau is determined

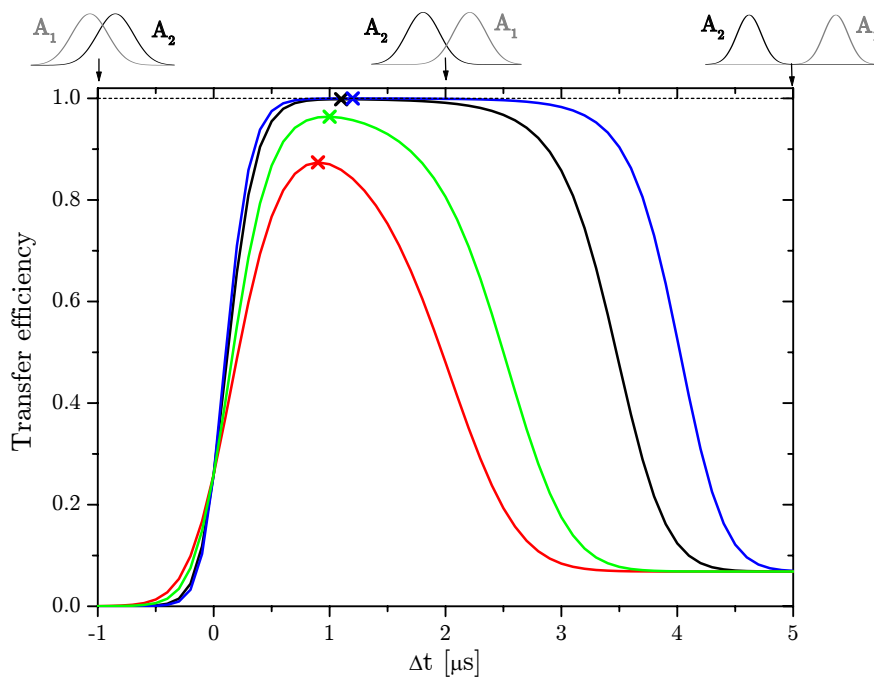


Figure 2.5: Transfer efficiency as a function of delay between pulses for different choices of peak Rabi frequencies, $A_{1,\max}/2\pi = A_{2,\max}/2\pi = 10$ MHz (—), $A_{1,\max}/2\pi = A_{2,\max}/2\pi = 20$ MHz (—), $A_{1,\max}/2\pi = A_{2,\max}/2\pi = 100$ MHz (—) and $A_{1,\max}/2\pi = A_{2,\max}/2\pi = 300$ MHz (—). Positive delay corresponds to the counter-intuitive pulse sequence, where the laser pulse of field 2 arrives before the laser pulse of field 1. The optimal delay is indicated by crosses. Parameters; $\tau_1 = \tau_2 = 2$ μ s and $\Delta_1 = \Delta_2 = 0$. The three pulse sequences on top illustrate the pulse positions at the delays indicated by the small arrows.

by the branching ratio between the different decay rates. The simulations show that for peak Rabi frequencies above $A_{1,\max}/2\pi = A_{2,\max}/2\pi = 100$ MHz the transfer efficiency is close to unity and insensitive to fluctuations in the delay. For smaller Rabi frequencies the transfer efficiency decreases and the sensitivity to fluctuations in delay increases.

The crosses in Fig. 2.5 indicate the optimal delay for each Rabi frequency and show that the optimal delay increases when the Rabi frequency increases. This is due to the tails of the Gaussian pulses and the finite simulation time. All population is transferred when $\theta = \pi/2$ and for Gaussian pulses

$$\tan \theta = \frac{A_1(t)}{A_2(t)} = \frac{A_{1,\max} e^{-\left(\frac{t}{\tau/2}\right)^2}}{A_{2,\max} e^{-\left(\frac{t+\Delta t}{\tau/2}\right)^2}} = \frac{A_{1,\max}}{A_{2,\max}} e^{\left(\frac{\Delta t^2 + 2t\Delta t}{(\tau/2)^2}\right)}. \quad (2.29)$$

For a simulation terminated at some fixed time $t = t_f$ a larger Δt implies θ closer to $\pi/2$ and therefore a higher transfer efficiency. On the other hand, a large delay will make it more difficult to obtain adiabaticity, but this can be compensated by large Rabi frequencies. The optimal pulse delay is therefore the largest possible not violating adiabaticity, favouring large delays for large Rabi frequencies. It should be noted, however, that inclusion of decoherence mechanisms as for example laser linewidth, tends to make the optimal delay smaller.

A longer pulse width, will of course strengthen the adiabaticity, but in experiments decoherence is also an issue imposing an upper limit on the time used and therefore on the pulse widths. Choosing the pulse width will thus be a trade-off between the effect of decoherence and diabatic transfer.

2.3.2 Laser detunings

In experiments one-photon excitations may reduce the efficiency and it is advantageous to introduce large one-photon detunings to diminish this effect. We have simulated the effect in Fig. 2.6. It shows that increasing the one-photon detuning does not limit the transfer efficiency as long as we are close to the two-photon resonance, $\Delta_2 - \Delta_1 = 0$, but also that this criterion gets stricter as we increase the one-photon detuning. If we require a transfer efficiency above 0.99 the demand on two-photon detuning is found from the green curve of Fig. 2.6 to be $|\Delta_2 - \Delta_1| \leq 2\pi \times 0.5$ MHz, when $\Delta_1 = 2\pi \times 1200$ MHz. For $\Delta_1 = 2\pi \times 600$ MHz, maintaining a two-photon resonance within $2\pi \times 1$ MHz is sufficient as found from the red curve. An efficient transfer can in this way be maintained in spite of a small drift from two-photon resonance.

A closer look at Fig. 2.6 reveals that the spectra are not exactly symmetric with respect to the sign of the two-photon detuning. With unbalanced Rabi frequencies, $A_{2,\max} = 2A_{1,\max}$, the asymmetry becomes more evident as seen in Fig. 2.7(a). For small negative two-photon detunings the transfer efficiency is much higher than for the corresponding positive two-photon detunings. This

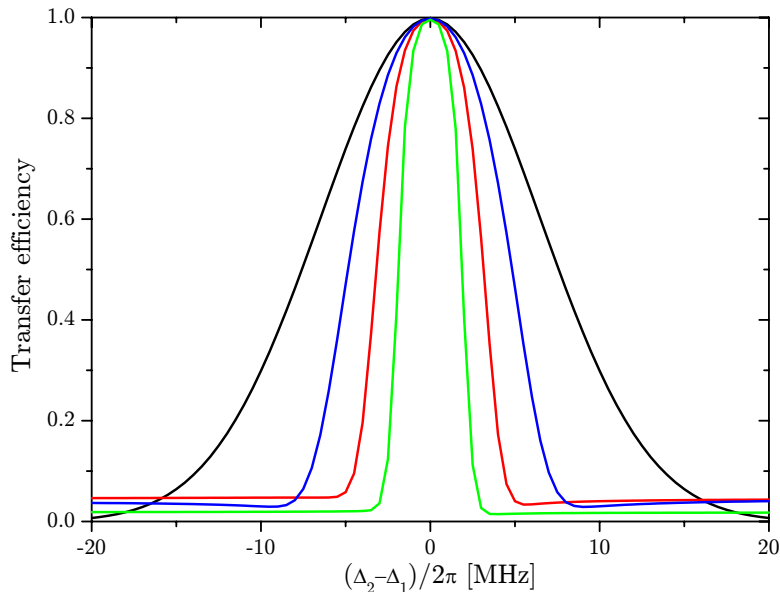


Figure 2.6: Transfer efficiency as a function of two-photon detuning ($\Delta_2 - \Delta_1$). The curves correspond to different one-photon detunings, $\Delta_1/2\pi = 0$ MHz (—), $\Delta_1/2\pi = 300$ MHz (—), $\Delta_1/2\pi = 600$ MHz (—) and $\Delta_1/2\pi = 1200$ MHz (—). Parameters, $A_{1,\max}/2\pi = A_{2,\max}/2\pi = 100$ MHz, $\tau_1 = \tau_2 = 2$ μ s and $\Delta t = 1.2$ μ s.

effect is due to diabatic transfer between $|D\rangle$ and the energetically closest bright state $|-\rangle$. As discussed previously, this is likely when $|D\rangle$ and $|-\rangle$ are nearly degenerate. The eigenvalues found in (2.16) are valid only on two-photon resonance. A more complicated general expression for the eigenvalues has as mentioned been derived in [39] and is plotted in Fig. 2.7(b-d), where we show the eigenvalues of $|D\rangle$ (solid curves) and $|-\rangle$ (dashed curves) as a function of time for three different choices of two-photon detuning. In the case where $\Delta_2 - \Delta_1 = 0$ MHz (Fig. 2.7(b)) the eigenvalues of course coincide when the Rabi frequencies are zero before and after the pulses, but in this case no diabatic transfer will occur as no coupling is present. For a positive two-photon detuning, $(\Delta_2 - \Delta_1)/2\pi = 5$ MHz (Fig. 2.7(d)), we see an avoided crossing leading to a probability for diabatic transfer to the $|-\rangle$ -state. Such a transfer leads to population of the $|e\rangle$ -state which decays rapidly. For a negative two-photon detuning, $(\Delta_2 - \Delta_1)/2\pi = -5$ MHz in Fig. 2.7(c), an energy splitting of $|D\rangle$ and $|-\rangle$ is present through the whole evolution and the probability for diabatic transfer is much smaller. It is this difference that gives rise to the asymmetry of the two-photon spectrum in Fig. 2.7(a).

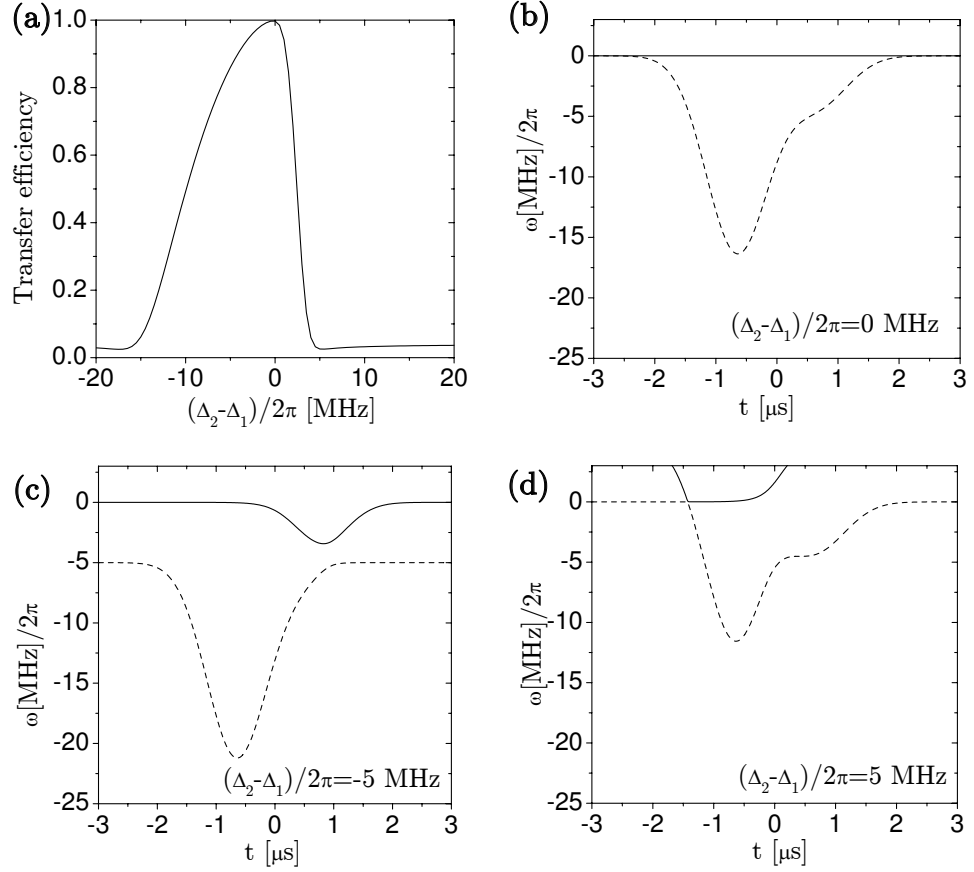


Figure 2.7: (a) Transfer efficiency as a function of two-photon detuning. Evolution of eigenvalues as a function of time for various two-photon detunings is shown in (b) $(\Delta_2 - \Delta_1)/2\pi = 0$ MHz, (c) $(\Delta_2 - \Delta_1)/2\pi = -5$ MHz and (d) $(\Delta_2 - \Delta_1)/2\pi = 5$ MHz. In (b), (c) and (d) we use the signatures, ω^D (—) and ω^- (- - -). Parameters used for all graphs, $A_{1,\max}/2\pi = 100$ MHz, $A_{2,\max}/2\pi = 200$ MHz, $\Delta_1/2\pi = 600$ MHz, $\tau_1 = \tau_2 = 2$ μ s and $\Delta t = 1.2$ μ s.

2.4 Summary

In quantum mechanics adiabaticity can be used to ensure that a system remain in some desired eigenstate. STIRAP is a well-documented method for population transfer between selected states in a robust manner. Small fluctuations in the controlling parameters do not influence the efficiency and the variables (detuning, pulse width and delay between pulses) discussed above can be chosen such that perfect transfer is achieved as shown in chapter 2.3. Unfortunately they are not the only variables to be considered in experiments. The atom will move, the phase of the laser will fluctuate, light might be present before and after the STIRAP process due to imperfect shutters, and external fields could influence the process. In chapter 7 and 8 we discuss these experimental limitations in relation to the work with trapped ions.

In this chapter we have only considered STIRAP for population transfer, but the adiabatic processes also have the nice feature that eigenstates acquire controllable geometric phases that are expected to be robust with respect to parameter fluctuations and certain kinds of noise as discussed in chapter 2.1.3. In chapter 3 and 5 we utilise the geometric phases acquired in a STIRAP process to create robust entanglement and quantum gates. In chapter 4 we take a closer look at one of the gates, when decoherence is present.

Chapter 3

Geometric phase gates

Quantum gates based on geometric phases can be employed to improve the robustness of quantum computation. In order to create a desired controllable geometric phase the system must undergo an adiabatic evolution, preferable in a dark state with eigenenergy zero such that no dynamic phase is acquired. One suitable candidate fulfilling these requirements is STIRAP where the system evolves adiabatically in the dark state found in (2.17). We show how this dark state acquires a geometric phase, which is used to create a one-qubit phase gate. We present a complete set of gates based on similar dark states acquiring geometric phases. The work described here was published in [II].

3.1 Geometric phase and STIRAP

As discussed in chapter 2.2, STIRAP can be described as a rotation of the adiabatic dark state in the $\{|1\rangle, |e\rangle, |2\rangle\}$ basis for the lambda system,

$$|D(t)\rangle = \cos\theta(t)|1\rangle - \sin\theta(t)e^{i\varphi_2(t)}|2\rangle, \quad (3.1)$$

where $\tan\theta = \frac{A_1}{A_2}$ is the fraction of the two Rabi frequency amplitudes and φ_2 the relative phase between the two laser fields as defined in (2.15). Initially ($\cos\theta = 1$ and $|\psi(t_i)\rangle = |1\rangle$), only $|D\rangle$ is populated and in the adiabatic limit all population remains in the $|D\rangle$ -state through the whole process. The dark state has zero energy eigenvalue and hence does not acquire any dynamic phase, but may acquire a geometric phase $\gamma_1(t)$, and we can write the wave function as

$$|\psi(t)\rangle = e^{i\gamma_1(t)}|D(t)\rangle. \quad (3.2)$$

In order to find the geometric phase we apply Berry's formula (2.8),

$$\gamma_1 = i \int_{R_i}^{R_f} \langle D | \nabla_{\vec{R}} | D \rangle \cdot d\vec{R}, \quad (3.3)$$

with \bar{R} -vector, $\bar{R} = \begin{pmatrix} \theta \\ \varphi_2 \end{pmatrix}$. We find the gradient of the dark state

$$\nabla_{\bar{R}}|D\rangle = \begin{pmatrix} -\sin\theta|1\rangle - \cos\theta e^{i\varphi_2}|2\rangle \\ -\sin\theta i e^{i\varphi_2}|2\rangle \end{pmatrix}, \quad (3.4)$$

calculate the inner product

$$\langle D|\nabla_{\bar{R}}|D\rangle = \begin{pmatrix} 0 \\ i \sin^2\theta \end{pmatrix} \Rightarrow \langle D|\nabla_{\bar{R}}|D\rangle \cdot d\bar{R} = i \sin^2\theta d\varphi_2, \quad (3.5)$$

and find the geometric phase

$$\gamma_1(t) = - \int_{\varphi_2(t_i)}^{\varphi_2(t)} \sin^2\theta d\varphi_2. \quad (3.6)$$

This yields the wave function

$$\psi(t) = e^{i\gamma_1(t)}|D(t)\rangle = e^{i\gamma_1(t)} \cos\theta(t)|1\rangle - e^{i(\gamma_1(t)+\varphi_2(t))} \sin\theta(t)|2\rangle,$$

which after the whole STIRAP pulse sequence ($\sin\theta = 1$) simply reads

$$\psi(t_f) = -e^{i(\gamma_1(t_f)+\varphi_2(t_f))}|2\rangle.$$

3.2 Geometric phase gates

Above we described how a geometric phase is acquired during a STIRAP process in a lambda system and we wish to use such geometric phases to construct quantum gates. In order to achieve this we add an extra ground state level and consider two atoms (ions or neutrals) with a tripod level structure as shown in Fig. 3.1. The $|0\rangle$ and the $|1\rangle$ states are the qubit states we wish to

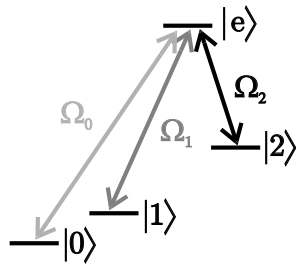


Figure 3.1: Four-level tripod system coupled by three laser fields with Rabi frequencies Ω_0 , Ω_1 and Ω_2 .

manipulate and we transfer population from $\{|0\rangle, |1\rangle\}$ to $|2\rangle$ via the $|e\rangle$ state using STIRAP processes such that geometric phases are acquired. The three lower states ($|0\rangle, |1\rangle$ and $|2\rangle$) are long-lived, and could in practice be ground Zeeman- or hyperfine-sublevels. The upper state $|e\rangle$ is an electronically excited state or excited state manifold. The lower states are coupled to the upper state by application of three resonant laser fields with Rabi frequencies Ω_0 , Ω_1 and

Ω_2 , respectively. We restrict the Rabi frequencies to the case where the relative phase between Ω_0 and Ω_1 , φ_{01} , is time independent, while the phase of Ω_2 , φ_2 , is time dependent,

$$\begin{aligned}\Omega_0 &= A_0(t), \\ \Omega_1 &= A_1(t)e^{-i\varphi_{01}}, \\ \Omega_2 &= A_2(t)e^{-i\varphi_2(t)}.\end{aligned}\quad (3.7)$$

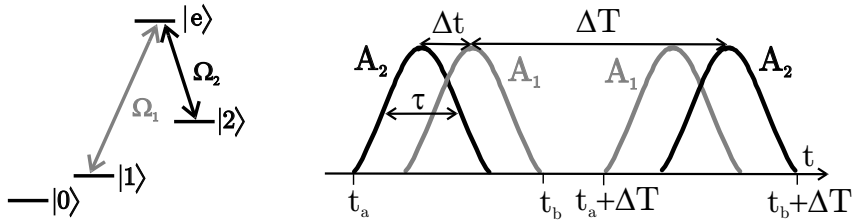
The real amplitudes of all fields (A_0, A_1, A_2) are time dependent and we use \sin^2 -pulses defined in (2.23) for the numerical simulations.

We now present a set of gates, which are universal for quantum computation, consisting of a one-qubit phase gate (S), a one-qubit Hadamard gate (Ha), and a two-qubit controlled phase gate (CS). Explicitly in the one- and two-qubit bases ($\{|0\rangle, |1\rangle\}$, $\{|00\rangle, |01\rangle, |10\rangle, |11\rangle\}$) the form of these gates are

$$S = \begin{bmatrix} 1 & 0 \\ 0 & e^{i\phi_1} \end{bmatrix}, \quad \text{Ha} = \frac{1}{\sqrt{2}} \begin{bmatrix} 1 & 1 \\ 1 & -1 \end{bmatrix}, \quad \text{CS} = \begin{bmatrix} 1 & 0 & 0 & 0 \\ 0 & 1 & 0 & 0 \\ 0 & 0 & 1 & 0 \\ 0 & 0 & 0 & e^{i\phi_2} \end{bmatrix}. \quad (3.8)$$

3.2.1 One-qubit phase gate

One STIRAP process is not sufficient to create a one-qubit phase gate. A phase is acquired but the population is also transferred from the qubit state, $|1\rangle$, to the $|2\rangle$ state, so we need to apply a second STIRAP sequence with pulses in reversed order transferring the population back to the qubit state. The whole pulse sequence is shown in Fig. 3.2(b), where τ is the FWHM, Δt the delay between pulses within one sequence and ΔT the delay between the two sequences. The initial condition is still $\psi(t_i) = |1\rangle$ and as in the case with



(a) Four-level tripod system coupled by two laser fields applied with Rabi frequencies Ω_1 and Ω_2 .

(b) Pulse sequence consisting of two STIRAP processes separated by ΔT in time. The FWHM of each pulse is τ and the delay between pulses within one process is Δt .

Figure 3.2

one sequence the wave function is as derived above

$$\psi(t) = e^{i\gamma_1(t)} |D(t)\rangle = e^{i\gamma_1(t)} \cos \theta(t) |1\rangle - e^{i(\gamma_1(t) + \varphi_2(t))} \sin \theta(t) |2\rangle, \quad (3.9)$$

but now the final state after the whole pulse sequence is

$$\psi(t_f) = e^{i\gamma_1} |1\rangle. \quad (3.10)$$

This corresponds to a one-qubit phase gate $|1\rangle \rightarrow e^{i\gamma_1} |1\rangle$ and the geometric phase is integrated over the whole pulse sequence from $t_i = t_a$ to $t_f = t_b + \Delta T$

$$\gamma_1 = - \int_{\varphi_2(t_a)}^{\varphi_2(t_b + \Delta T)} \sin^2 \theta(t) d\varphi_2(t), \quad (3.11)$$

where

$$\sin^2 \theta(t) = \frac{A_1^2(t)}{A_1^2(t) + A_2^2(t)}. \quad (3.12)$$

The integral in (3.11) can be solved analytically when we assume that all four pulses are described by the common function $A(t)$. The instants of time t_a and t_b in Fig. 3.2(b) are defined such that $\sin^2 \theta(t) \approx 0$ for $t < t_a$ and $t > t_b + \Delta T$ and $\sin^2 \theta(t) \approx 1$ for $t_b < t < t_a + \Delta T$. With these definitions we obtain from (3.11) and (3.12)

$$\begin{aligned} \gamma_1 = & - \int_{\varphi_2(t_a)}^{\varphi_2(t_b)} \frac{A^2(t)}{A^2(t) + A^2(t + \Delta t)} d\varphi_2 \quad (3.13) \\ & - \int_{\varphi_2(t_b)}^{\varphi_2(t_a + \Delta T)} 1 d\varphi_2 \\ & - \int_{\varphi_2(t_a + \Delta T)}^{\varphi_2(t_b + \Delta T)} \frac{A^2(t + \Delta t - \Delta T)}{A^2(t + \Delta t - \Delta T) + A^2(t - \Delta T)} d\varphi_2. \end{aligned}$$

Substituting $t' = t - \Delta T$ in the last integral and assuming that φ_2 is a monotonic function we obtain

$$\begin{aligned} \gamma_1 = & - \int_{t_a}^{t_b} \frac{A^2(t)}{A^2(t) + A^2(t + \Delta t)} \frac{d\varphi_2}{dt} dt \quad (3.14) \\ & - \int_{t_b}^{t_a + \Delta T} \frac{d\varphi_2}{dt} dt \\ & - \int_{t_a}^{t_b} \frac{A^2(t' + \Delta t)}{A^2(t' + \Delta t) + A^2(t')} \frac{d\varphi_2}{dt} dt' \\ = & - \int_{t_a}^{t_a + \Delta T} \frac{d\varphi_2}{dt} dt = \varphi_2(t_a) - \varphi_2(t_a + \Delta T). \end{aligned}$$

The geometric phase thus only depends on the laser field phases and requires control of ΔT and similarity of the four pulses. All these quantities are routinely controlled to high precision in present-day laboratories. The population

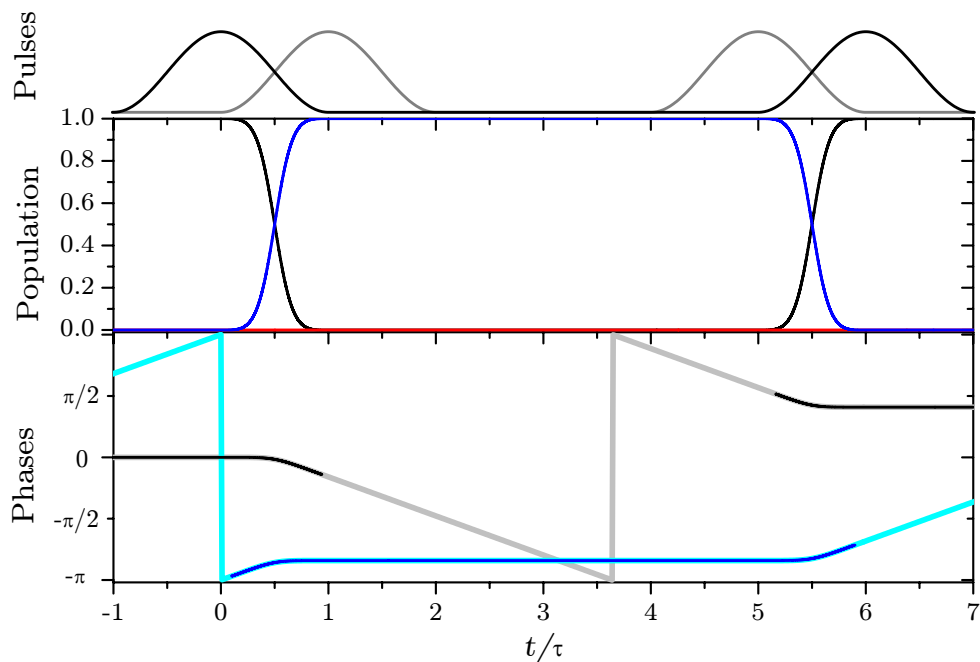


Figure 3.3: The centre panel shows the evolution of the population in states $|1\rangle$ (black), $|e\rangle$ (red), and $|2\rangle$ (blue). The lower panel shows the evolution of the phases, ϕ_1 of state $|1\rangle$ (grey, black) and ϕ_2 of state $|2\rangle$ (cyan, blue). Analytical results are shown with cyan or grey curves and numerical with blue or black curves. The numerically calculated phases are only shown when the corresponding population is non-zero. The calculations were made with \sin^2 -pulses, Eq. (2.23), and parameters in units of the pulse width τ , $\varphi_2 = t/\tau$, $A_{\max,1}\tau/2\pi = A_{\max,2}\tau/2\pi = 100$, $\Delta t/\tau = 1$, $\Delta T/\tau = 5$.

and the phases of the three states $|1\rangle$, $|e\rangle$ and $|2\rangle$ can be found numerically by solving the time-dependent Schrödinger equation (See details in appendix A). An example of this is shown in the centre panel of Fig. 3.3. All population is initially in the $|1\rangle$ -state (black curve). During the first STIRAP-process the population is transferred from $|1\rangle$ to $|2\rangle$ (blue curve) while the second STIRAP-process transfers the population back to $|1\rangle$. The $|e\rangle$ -state (red curve) is never populated and hence no loss of population occurs due to spontaneous emission from $|e\rangle$. The evolution of the phases can be found numerically as well as analytically, as shown with the cyan/grey and the blue/black curves in the lower panel of Fig. 3.3. In the time-spans where the states in question are populated, the direct numerical solution of the time-dependent Schrödinger equation gives results for the phases in agreement with the above analytical results. The grey curve shows the phase of $|1\rangle$, ϕ_1 . This phase is the geometric phase ($\phi_1 = \gamma_1$) and it remains zero until the first set of STIRAP pulses arrive (t_a in Fig. 3.2(b)). It then accumulates a phase until the second pair

of pulses has passed ($t_b + \Delta T$ in Fig. 3.2(b)). The total acquired phase is as shown in (3.14), $\gamma_1 = \varphi_2(t_a) - \varphi_2(t_a + \Delta T)$. The phase of the $|2\rangle$ -state (ϕ_2) (cyan curve) contains not only the geometric phase γ_1 but also the additional $\varphi_2 - \pi$ [see Eq. (3.1)] yielding a total phase $\phi_2 = \gamma_1 + \varphi_2 - \pi$. The $|2\rangle$ -state therefore accumulates a phase before the first and after the second STIRAP process -but none in between where γ_1 and φ_2 cancel each other.

3.2.2 Hadamard gate

Creating a Hadamard gate takes a little more effort than the one-qubit phase gate but relies on the same principles now involving two dark states. It is implemented using all three laser fields with Rabi frequencies Ω_0 , Ω_1 and Ω_2 as defined in (3.7) and shown in Fig. 3.4(a). In the rotating wave approximation

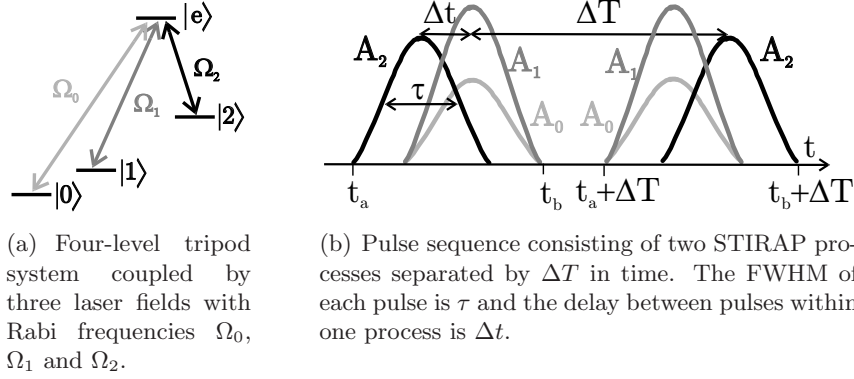


Figure 3.4

we derive the Hamiltonian

$$H(t) = \frac{\hbar}{2} \begin{bmatrix} 0 & 0 & A_0(t) & 0 \\ 0 & 0 & A_1(t)e^{i\varphi_{01}} & 0 \\ A_0(t) & A_1(t)e^{-i\varphi_{01}} & 0 & A_2(t)e^{-i\varphi_2(t)} \\ 0 & 0 & A_2(t)e^{i\varphi_2(t)} & 0 \end{bmatrix} \quad (3.15)$$

expressed in the $\{|0\rangle, |1\rangle, |e\rangle, |2\rangle\}$ basis. We parameterise the complex Rabi frequencies

$$\Omega_0(t) = \sin \theta_{01} \sqrt{A_0(t)^2 + A_1(t)^2}, \quad (3.16)$$

$$\Omega_1(t) = \cos \theta_{01} \sqrt{A_0(t)^2 + A_1(t)^2} e^{-i\varphi_{01}}, \quad (3.17)$$

$$\Omega_2(t) = \cos \theta_H(t) \sqrt{A_0(t)^2 + A_1(t)^2 + A_2(t)^2} e^{-i\varphi_2(t)}, \quad (3.18)$$

where the two angles are defined as $\tan \theta_{01} = A_0(t)/A_1(t)$ and $\tan \theta_H(t) = \sqrt{A_0^2(t) + A_1^2(t)}/A_2(t)$. A diagonalisation of (3.15) gives the four energy eigenvalues

$$\omega^\pm = \pm \frac{1}{2} \sqrt{A_0^2 + A_1^2 + A_2^2}, \quad \omega^{D_i} = 0 \quad (i = 1, 2), \quad (3.19)$$

and eigenvectors

$$\begin{aligned}
|+\rangle &= \frac{1}{\sqrt{2}} \left[\sin \theta_H(t)(\sin \theta_{01}|0\rangle + \cos \theta_{01}e^{i\varphi_{01}}|1\rangle) - |e\rangle + \cos \theta_H(t)e^{i\varphi_2(t)}|2\rangle \right], \\
|-\rangle &= \frac{1}{\sqrt{2}} \left[\sin \theta_H(t)(\sin \theta_{01}|0\rangle + \cos \theta_{01}e^{i\varphi_{01}}|1\rangle) + |e\rangle + \cos \theta_H(t)e^{i\varphi_2(t)}|2\rangle \right], \\
|D_1\rangle &= -\cos \theta_H(t)(\sin \theta_{01}|0\rangle + \cos \theta_{01}e^{i\varphi_{01}}|1\rangle) + \sin \theta_H(t)e^{i\varphi_2(t)}|2\rangle, \\
|D_2\rangle &= \cos \theta_{01}|0\rangle - \sin \theta_{01}e^{i\varphi_{01}}|1\rangle.
\end{aligned} \tag{3.20}$$

We assume that the system is initially ($t = t_i$) in a superposition of the dark states and that the evolution is adiabatic. Then the population stays within the space spanned by the two dark states and the wave function at later times is given by

$$|D(t)\rangle = C_{D_1}(t)|D_1(t)\rangle + C_{D_2}(t)|D_2(t)\rangle. \tag{3.21}$$

In order to determine the time evolution of the coefficients $\{C_{D_1}(t), C_{D_2}(t)\}$ we use the method for degenerate eigenvalues described in chapter 2.1.2. The time evolution is given by the Schrödinger equation $i\hbar|\dot{D}(t)\rangle = H(t)|D(t)\rangle = 0$ and yields two coupled differential equations

$$\begin{aligned}
\dot{C}_{D_1} &= -C_{D_1}\langle D_1|\dot{D}_1\rangle - C_{D_2}\langle D_1|\dot{D}_2\rangle, \\
\dot{C}_{D_2} &= -C_{D_1}\langle D_2|\dot{D}_1\rangle - C_{D_2}\langle D_2|\dot{D}_2\rangle.
\end{aligned} \tag{3.22}$$

Only one coefficient is non-zero, $\langle D_1|\dot{D}_1\rangle = i\dot{\varphi}_2 \sin^2 \theta_H$ and hence the differential equations just read

$$\begin{aligned}
\dot{C}_{D_1} &= -i\dot{\varphi}_2 \sin^2 \theta_H C_{D_1} \\
\dot{C}_{D_2} &= 0,
\end{aligned} \tag{3.23}$$

yielding the simple evolution

$$\begin{aligned}
C_{D_1}(t) &= e^{i\gamma_H} C_{D_1}(t_i), \\
C_{D_2}(t) &= C_{D_2}(t_i).
\end{aligned} \tag{3.24}$$

The phase

$$\gamma_H = - \int_{t_i}^t \dot{\varphi}_2 \sin^2 \theta_H dt', \tag{3.25}$$

acquired by $|D_1\rangle$ is purely geometric because the dark states do not acquire any dynamic phases, $\omega^{D_i} = 0$. Since no population is transferred between the two dark states the geometric phase acquired by $|D_1\rangle$ could also be calculated using Berry's original formula (2.8). This approach was used in Refs. [22] and [II].

The geometric phase is only acquired by one of the dark states and it can therefore be used to control the superposition

$$|D(t)\rangle = e^{i\gamma_H} C_{D_1}(t_i) |D_1(t)\rangle + C_{D_2}(t_i) |D_2(t)\rangle. \quad (3.26)$$

For the Hadamard gate, like for the one-qubit gate, the pulse sequence consists of two STIRAP processes, but this time with both Ω_0 and Ω_1 applied simultaneously with different amplitudes as shown in Fig. 3.4(b). This creates a constant θ_{01} , while θ_H is varied according to

$$\cos \theta_H(t) = \frac{A_2(t)}{\sqrt{A_0(t)^2 + A_1(t)^2 + A_2(t)^2}}. \quad (3.27)$$

Initially, with all population in $|0\rangle$ or $|1\rangle$ and $\cos \theta_H = 1$ only the dark states are populated [See Eq. (3.20)]. The first set of pulses transfers population partially from $|0\rangle$ and $|1\rangle$ to $|2\rangle$ while the second transfers all population back to $|0\rangle$ and $|1\rangle$. Only population in $|D_1\rangle$ will be transferred, while $|D_2\rangle$ is unaffected. After the whole pulse sequence ($\sin \theta_H = 1$) the system ends up in the final state

$$\begin{aligned} |D(t_f)\rangle &= C_{D_1}(t_i) e^{i\gamma_H(t_f)} |D_1(t_f)\rangle + C_{D_2}(t_i) |D_2(t_f)\rangle \\ &= [-\sin \theta_{01} C_{D_1}(t_i) e^{i\gamma_H(t_f)} + \cos \theta_{01} C_{D_2}(t_i)] |0\rangle \\ &\quad + [-\cos \theta_{01} C_{D_1}(t_i) e^{i\gamma_H(t_f)} + \sin \theta_{01} C_{D_2}(t_i)] |1\rangle, \end{aligned} \quad (3.28)$$

where we have used (3.20) in the second line. In the $\{|0\rangle, |1\rangle\}$ -basis, an initial state $|\psi_i\rangle = a_i|0\rangle + b_i|1\rangle$ is transferred to a final state $|\psi_f\rangle = a_f|0\rangle + b_f|1\rangle = U|\psi_i\rangle$, with the unitary transformation

$$U = \begin{bmatrix} \cos^2 \theta_{01} + e^{i\gamma_H} \sin^2 \theta_{01} & \cos \theta_{01} \sin \theta_{01} e^{-i\varphi_{01}} (e^{i\gamma_H} - 1) \\ \cos \theta_{01} \sin \theta_{01} e^{i\varphi_{01}} (e^{i\gamma_H} - 1) & \sin^2 \theta_{01} + e^{i\gamma_H} \cos^2 \theta_{01} \end{bmatrix}. \quad (3.29)$$

By carefully adjusting the amplitudes and phases of the laser fields, the values of θ_{01} , φ_{01} and γ_H can be controlled and thus generate rotations in the $\{|0\rangle, |1\rangle\}$ -basis. We note that U is the identity when no geometric phase is acquired, $\gamma_H = 0$. As a special case $\theta_{01} = \frac{\pi}{8}$, $\varphi_{01} = \pi$ and $\gamma_H = -\pi$ implement a Hadamard gate

$$U = \frac{1}{\sqrt{2}} \begin{bmatrix} 1 & 1 \\ 1 & -1 \end{bmatrix}. \quad (3.30)$$

More specifically, $\theta_{01} = \frac{\pi}{8}$ can be obtained by choosing the relative laser field strengths such that $A_{\max,0} = A_{\max,1}(\sqrt{2} - 1)$. Furthermore, $A_{\max,2} = \sqrt{A_{\max,0}^2 + A_{\max,1}^2}$, $\varphi_2 = t/\tau$ and $\Delta T/\tau = \pi$ assure $\gamma_H = -\pi$.

3.2.3 Two-qubit phase gate

STIRAP processes are well suited for creating arbitrary one-qubit rotations, but quantum computation requires gates acting on two or more qubits and these are typically more difficult to implement because they necessitate a controllable coupling between the qubits. We consider a coupling $E|22\rangle\langle 22|$ between two atoms with the tripod level structure shown in Fig. 3.5. We apply

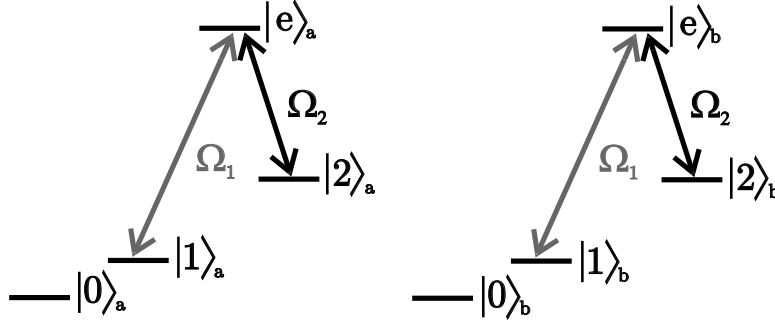


Figure 3.5: Two atoms with a four-level tripod structure with two laser fields applied with Rabi frequencies Ω_1 and Ω_2 .

only two laser fields Ω_1 and Ω_2 , assume no relative phase between the two Rabi frequencies and without loss of generality write them as real, $\Omega_1 = A_1$ and $\Omega_2 = A_2$. The Hamiltonian in the two atomic basis $\{|ji\rangle = |j\rangle_a|i\rangle_b\}_{j,i=0,1,e,2}$ reads

$$\begin{aligned}
 H = & -\frac{\hbar}{2}\Omega_1 [(|1\rangle_a\langle e| + |e\rangle_a\langle 1|) \otimes \mathbb{I}_b + \mathbb{I}_a \otimes (|1\rangle_b\langle e| + |e\rangle_b\langle 1|)] \\
 & -\frac{\hbar}{2}\Omega_2 [(|2\rangle_a\langle e| + |e\rangle_a\langle 2|) \otimes \mathbb{I}_b + \mathbb{I}_a \otimes (|2\rangle_b\langle e| + |e\rangle_b\langle 2|)] \\
 & + E|2\rangle_a\langle 2|_b\langle 2|_a\langle 2|.
 \end{aligned} \tag{3.31}$$

In order to solve (3.31) it is advantageous to go into the interaction picture with respect to the coupling term in the Hamiltonian, $H_0 = E|22\rangle\langle 22|$. Here the Hamiltonian is solved analytically yielding eigenvalues

$$\omega = \begin{cases} 0 & \text{multiplicity 6} \\ 2\sqrt{\Omega_1^2 + \Omega_2^2} & \text{multiplicity 4} \\ -2\sqrt{\Omega_1^2 + \Omega_2^2} & \text{multiplicity 4} \\ \sqrt{\Omega_1^2 + \Omega_2^2} & \text{multiplicity 1} \\ -\sqrt{\Omega_1^2 + \Omega_2^2} & \text{multiplicity 1} \end{cases}, \tag{3.32}$$

and an orthonormal basis for the 6-dimensional null space,

$$\begin{aligned}
|D_1\rangle &= |00\rangle, \\
|D_2\rangle &= -\cos\theta|10\rangle + \sin\theta|20\rangle, \\
|D_3\rangle &= -\cos\theta|01\rangle + \sin\theta|02\rangle, \\
|D_4\rangle &= 1/\sqrt{2}(\sin\theta(|1e\rangle - |e1\rangle) + \cos\theta(|2e\rangle - |e2\rangle)), \\
|D_5\rangle &= \cos^2\theta|11\rangle - \sin\theta\cos\theta(|12\rangle + |21\rangle) + \sin^2\theta e^{iEt}|22\rangle, \\
|D_6\rangle &= 1/\sqrt{2}(-\sin^2\theta|11\rangle - \sin\theta\cos\theta(|12\rangle + |21\rangle) + |ee\rangle - \cos^2\theta e^{iEt}|22\rangle),
\end{aligned} \tag{3.33}$$

where $\tan\theta = \frac{A_1}{A_2}$. We note that $|D_2\rangle$ and $|D_3\rangle$ are exactly the single atom dark states used for the one-qubit phase gate. With six degenerate states we once more use the method of chapter 2.1.2. We assume that we start with all population in $|11\rangle$, only Ω_2 applied ($\cos\theta = 1$) and write $\psi(t_i) = |D_5(t_i)\rangle$. Initially, the Schrödinger and the interaction picture coincides and hence $\psi_I(t_i) = \psi(t_i)$, where I indicates the interaction picture. We assume an adiabatic evolution and hence no population transfer between the six dark states and the bright states will occur. The interaction picture wave function at later times is

$$|D_I(t)\rangle = \sum_b B_b(t)|D_b(t)\rangle. \tag{3.34}$$

The time evolution of the coefficients is given by the Schrödinger equation

$$\begin{aligned}
|\dot{D}_I(t)\rangle &= \frac{-i}{\hbar}(H(t) - H_0(t))|D_I(t)\rangle \Rightarrow \\
\sum_b \dot{B}_b(t)|D_b(t)\rangle + B_b(t)|\dot{D}_b(t)\rangle &= \frac{-i}{\hbar} \sum_b B_b(t)(H(t) - H_0(t))|D_b(t)\rangle = 0 \Rightarrow \\
\sum_b \dot{B}_b(t)|D_b(t)\rangle &= - \sum_b B_b(t)|\dot{D}_b(t)\rangle,
\end{aligned} \tag{3.35}$$

where we have used that $[H(t) - H_0(t)]|D_b(t)\rangle = 0$ for all dark states. Taking the inner product with $\langle D_c(t)|$ gives the coupled differential equations,

$$\dot{B}_c(t) = - \sum_b B_b(t)\langle D_c(t)|\dot{D}_b(t)\rangle. \tag{3.36}$$

The only non-zero $\langle D_c | \dot{D}_b \rangle$ -elements are,

$$\begin{aligned}\langle D_5 | \dot{D}_5 \rangle &= iE \sin^4 \theta, \\ \langle D_5 | \dot{D}_6 \rangle &= \frac{i}{\sqrt{2}} E \cos^2 \theta \sin^2 \theta, \\ \langle D_6 | \dot{D}_5 \rangle &= \frac{i}{\sqrt{2}} E \cos^2 \theta \sin^2 \theta, \\ \langle D_6 | \dot{D}_6 \rangle &= \frac{i}{2} E \cos^4 \theta,\end{aligned}\tag{3.37}$$

and the differential equations for the B -coefficient reduce to,

$$\begin{aligned}\dot{B}_1 &= 0, \quad \dot{B}_2 = 0, \quad \dot{B}_3 = 0, \quad \dot{B}_4 = 0, \\ \dot{B}_5 &= -iE \sin^4 \theta B_5 - \frac{i}{\sqrt{2}} E \cos^2 \theta \sin^2 \theta B_6, \\ \dot{B}_6 &= -\frac{i}{\sqrt{2}} E \cos^2 \theta \sin^2 \theta B_5 - i\frac{1}{2} E \cos^4 \theta B_6.\end{aligned}\tag{3.38}$$

All population is initially in $|D_5\rangle$ and (3.38) shows that only when $\cos^2 \theta \sin^2 \theta$ is non-vanishing, population can be transferred from $|D_5\rangle$ to $|D_6\rangle$. Keeping the time when $\cos^2 \theta \sin^2 \theta \neq 0$ short ensures that effectively all population stays in $|D_5\rangle$ while accumulating a phase. In this regime where $B_6(t) \approx 0$ we may readily solve (3.38) and obtain the wave function

$$\begin{aligned}|\dot{D}_I(t)\rangle &= e^{-iE \int_{t_i}^t \sin^4 \theta dt} |D_5\rangle \\ &= \cos^2 \theta e^{-iE \int_{t_i}^t \sin^4 \theta dt} |11\rangle \\ &\quad - \sin \theta \cos \theta e^{-iE \int_{t_i}^t \sin^4 \theta dt} (|12\rangle + |21\rangle) \\ &\quad + \sin^2 \theta e^{-iE \int_{t_i}^t \sin^4 \theta dt + iEt} |22\rangle.\end{aligned}\tag{3.39}$$

Going back to the Schrödinger picture an extra phase is added to the $|22\rangle$ state,

$$\begin{aligned}|D\rangle &= e^{-iE|22\rangle\langle 22|t} |D_I\rangle \\ &= e^{-iE \int_{t_i}^t \sin^4 \theta dt} [\cos^2 \theta |11\rangle - \sin \theta \cos \theta (|12\rangle + |21\rangle) + \sin^2 \theta |22\rangle].\end{aligned}\tag{3.40}$$

We stay in $|D_5\rangle$ during the whole sequence acquiring the geometric phase

$$\gamma_2 = -E \int_{-\infty}^t \sin^4 \theta dt,\tag{3.41}$$

and the two STIRAP sequences thus transfers $|11\rangle \rightarrow e^{i\gamma_2}|11\rangle$. When only one atom is in the $|1\rangle$ -state the evolution is exactly as described for the one-qubit phase gate, but here no geometric phase is accumulated because the phases of the laser fields are kept fixed ($\dot{\varphi}_2 = 0$), i.e.,

$$\begin{aligned} |00\rangle &\rightarrow |00\rangle \\ |01\rangle &\rightarrow |01\rangle \\ |10\rangle &\rightarrow |10\rangle \\ |11\rangle &\rightarrow e^{i\gamma_2}|11\rangle. \end{aligned} \tag{3.42}$$

Maintaining adiabaticity limits our choice of parameters and now we additionally need to ensure a small population transfer to $|D_6\rangle$. In order to achieve this we need to keep $\int E \cos^2 \theta \sin^2 \theta dt$ small. On the other hand we wish to acquire a geometric phase $\gamma_2 = -E \int_{-\infty}^t \sin^4 \theta dt$. Fortunately, these requirements are not contradictory because γ_2 is mainly acquired between the two set of pulses, where $\sin^4 \theta = 1$, while $\cos^2 \theta \sin^2 \theta$ is only non-zero during the overlap of pulses. Therefore the smallest pulse width not violating adiabaticity should be used. For this pulse width the optimal delay, Δt , will be a trade off. A large delay will decrease the time where $\cos^2 \theta \sin^2 \theta$ is non-zero, but make it more difficult to maintain adiabaticity. With an optimal pulse delay, E and ΔT must be chosen such that $\int E \cos^2 \theta \sin^2 \theta dt$ is small while $\gamma_2 \approx E\Delta T$ is equal to, e.g., π . This will be a trade off between fidelity and gate time. As an example the parameters $A_{\max,i}\tau/2\pi = 100$, $\Delta t/\tau = 1.35$, $\Delta T/\tau = 2.7$, $E\tau/2\pi = 0.1$ lead to a phase $\gamma_2 = \pi$ and a fidelity $|\langle D(t_f)|\psi(t_f)\rangle|^2 = 0.99$, where $|\psi(t_f)\rangle$ was found propagating the Schrödinger equation with initial state $|11\rangle$ and projected onto the idealised final state $|D(t_f)\rangle = e^{i\gamma_2}|11\rangle$. The simulations are made with decay rate $\Gamma_e\tau/2\pi = 1$ in order to enhance the effect of population transfer to $|D_6\rangle$ populating $|e\rangle$.

The two-qubit gate exploits the small energy shift, when two particles occupy the same state, to create a conditional geometric phase. Alternatively, a large energy shift could have been employed to block certain states from being populated and hence alter the dark states followed by the system steering it through different dark states depending on the number of particles present. The different dark states acquire different geometric phases and thus a phase gate is achieved. This method is explored in chapter 5.

3.2.4 Experimental realisation

The one-qubit gates are implemented choosing an atom with three stable states and one excited state. The demands for laser and pulse sequence parameters are basically the same as for a single STIRAP process described in chapter 2.3. In addition the relative phase of the two laser fields needs to be controlled. This could be achieved implementing the gates in systems where

the three laser frequencies lie so close that all fields can be generated from the same source and hence the relative phases of the fields are easily controllable. Encoding $\{|0\rangle, |1\rangle, |2\rangle\}$ in atomic Zeeman- or hyperfine-substates would fulfil this. These requirements can be achieved in various atomic systems such as optically trapped neutral atoms, trapped ions and rare-earth ions doped into crystals.

To provide the coupling $E|22\rangle\langle 22|$ for the two-qubit gate we need to be a little more specific, and we suggest in the case of trapped atoms or ions to exploit the long-range dipole-dipole interaction between Rydberg excited atoms [41] (described in chapter 5) and in the case of doped crystals to use the interaction between excited states with permanent dipole moments [42]. How to use this interaction to create $E|22\rangle\langle 22|$ is an open question. One suggestion could be to apply an off-resonant laser field between $|2\rangle$ and an excited state with large dipole moment. As shown in [43], this off-resonant excitation causes energy shifts (AC Stark shifts) of the $|2\rangle$ states, and due to the dipole-dipole interaction, this shift will have a non-separable component of precisely the desired form for suitable choices of the laser detunings and strengths. The problem with this approach is that in order to create a sufficiently large energy shift without populating the excited state the interaction time must be very long because the interaction is off-resonant.

Decoherence due to spontaneous emission from the upper state $|e\rangle$ is negligible, because all population transfers are done without populating this state, with the possible exception of the undesirable population of $|D_6\rangle$ for the two-qubit gate. Other decoherence mechanisms could influence the gates and to avoid this fast processes are preferable. The exact values depend on the system. With trapped ions, Rabi frequencies of some hundred MHz are easily achievable and the adiabatic gates can be performed in a few microseconds. On this timescale decoherence will not limit the STIRAP efficiency as shown experimentally as well as theoretically [I, III]. In neutral atoms interacting via Rydberg excited state dipole moments, Rabi frequencies may exceed MHz. A dephasing time of $870 \mu\text{s}$ between two hyperfine states in Rubidium atoms in an optical dipole trap was measured using Ramsey spectroscopy [44] and also here decoherence is not expected to be a limiting factor for the proposed gates. This is supported by an experiment where population was transferred efficiently in Rydberg atoms using adiabatic passage [45]. Rare-earth-ions have coherence lifetimes exceeding ms and also here adiabatic transfer was demonstrated with pulses well below ms [46, 47]. In chapter 4 we show how a dephasing will affect the geometric phases and the fidelity of the Hadamard gate.

3.3 Conclusion

We have shown that in the adiabatic limit population transfer in tripod systems introduces purely geometric phases. These phases can be used to form a set of robust geometric gates. The performance of the three gates depends on the robustness of the geometric phases. The population transfers are done without ever populating the upper state $|e\rangle$ in the tripod system, which ensures that the gates are insensitive to spontaneous emission and STIRAP allows for some fluctuations in the controlling parameters. Pulse shapes, delay between sequences and ratio between Rabi frequencies are routinely controlled experimentally without drift in the laboratory and using systems where the three laser fields are generated from the same source, the relative laser phases are also controllable.

In the two-qubit gate the product of the coupling strength, E , and the time when the pulses overlap must be kept small, while the product of E and the time spent between pulse pairs should yield the desired phase. This implies that the latter time interval must be an order of magnitude longer than the duration of the STIRAP pulses. In the mentioned examples the coherence times of the systems are indeed sufficiently long to fulfil this constraint. In conclusion, the one-qubit gates are governed by parameters that are achievable in present-day laboratories and can be performed on timescales where decoherence is not a limiting factor. The two-qubit gate is only feasible if a realistic implementation of the coupling is found. In chapter 5 we present an alternative geometric two-qubit gate in Rydberg atoms.

Chapter 4

Geometric phases of an open system

Chapter 3 presented an universal set of gates based on dark states that acquire geometric phases. The geometric phases are expected to be robust against some sources of decoherence as discussed in chapter 2.1.3. To study decoherence we need to generalise the concept of geometric phase to open quantum systems. Various proposals have been made [48–50] and they all point to the problem that phase information tends to be lost when the system is open and decoheres for instance due to spontaneous emission. The full system including decoherence can still be described, for example, by the density matrix approach, which predicts the relative phases between the involved basis states. The information about the phases acquired by each eigenstate, however, is not available nor is the information about the geometric or dynamic nature of the phase. We will here use the Monte Carlo wave function (MCWF) approach [51, 52] and we consider as an example the Hadamard gate of chapter 3.2.2. For the open system we calculate geometric phases and show how the gate fidelity is affected. This work was published in [IV].

4.1 Evolution of an open system

4.1.1 Lindblad master equation

The evolution of an open system can be found by solving the Lindblad master equation [53],

$$\dot{\rho} = -\frac{i}{\hbar}[H, \rho] - \frac{1}{2} \sum_m (C_m^\dagger C_m \rho + \rho C_m^\dagger C_m) + \sum_m C_m \rho C_m^\dagger, \quad (4.1)$$

where H is the Hamiltonian for the closed system and the decoherence is described by the Lindblad operators, C_m . The Lindblad master equation describes the evolution of a system coupled to some environment. It is derived

as the reduced trace over the environment variables assuming the Markov approximation, that is $\dot{\rho}(t)$ only depends on $\rho(t)$ at the same time. The C_m operators are not uniquely defined and have not necessarily any physical interpretation.

4.1.2 Quantum Monte Carlo approach

The Lindblad master equation results in an ensemble average of the evolution, but does not reveal a clear distinction between the geometric and dynamic phases. Instead we use the quantum jump approach, where the wave function is evolved stochastically [51, 52]. Here we can follow the evolution of the wave functions as well as the acquired geometric and dynamic phases. We see how the population in the atomic states and the relative phases between them are affected by the decoherence.

For a small time step, δt , the evolution of the wave function is described as either a jump, that is a projection by one of the Lindblad operators,

$$|\psi_{nn}(t + \delta t)\rangle = C_m |\psi(t)\rangle \quad (4.2)$$

or by a no-jump evolution with the non-Hermitian Hamiltonian

$$\begin{aligned} \tilde{H} &= H + H', \\ H' &= \frac{-i\hbar}{2} \sum_m C_m^\dagger C_m, \end{aligned} \quad (4.3)$$

which for a sufficiently small δt yields

$$|\psi_{nn}(t + \delta t)\rangle = \left(1 - \frac{i\tilde{H}\delta t}{\hbar}\right) |\psi(t)\rangle. \quad (4.4)$$

The propagated wave function is not normalised as denoted by $\{.\}_{nn}$. The probability for the system to follow the no-jump evolution is given by the squared norm of the wave function.

$$\begin{aligned} \langle \psi_{nn}(t + \delta t) | \psi_{nn}(t + \delta t) \rangle &= \langle \psi(t) | \left(1 + \frac{i\tilde{H}^\dagger \delta t}{\hbar}\right) \left(1 - \frac{i\tilde{H} \delta t}{\hbar}\right) | \psi(t) \rangle \quad (4.5) \\ &= 1 - \frac{i}{\hbar} \langle \psi(t) | C_m^\dagger C_m | \psi(t) \rangle \\ &\equiv 1 - \delta p \equiv 1 - \sum_m \delta p_m \end{aligned}$$

where $\delta p_m = \delta t \langle \psi(t) | C_m^\dagger C_m | \psi(t) \rangle$ is the probability for the m^{th} jump to occur within the time step δt . For the method to be valid, δt has to be so small that

$\delta p \ll 1$ and the evolution is therefore to a good approximation given by the non-Hermitian Hamiltonian.

Numerically, different methods can be employed to determine when a jump occurs. One method is for each time step to choose a random number between 0 and 1, propagate the wave function one time step with the non-Hermitian Hamiltonian, calculate the square of the wave function norm and if it is less than the random number a jump occurs. Finally, the wave function is normalised after each time step and a new random number chosen. A more efficient method is to choose one random number and then propagate the wave function until its norm squared is less than the number - at this instant a jump occurs. When we average over many different traces we reproduce the density matrix calculation. For further details see for example [51, 52].

4.1.3 Decoherence model

We consider the Hadamard gate described in chapter 3.2.2. Decoherence due to spontaneous emission has little effect because $|e\rangle$ is never populated, but dephasing of the state $|0\rangle$ due to, e.g., collisions or phase fluctuation of the field Ω_0 will influence the evolution. We consider for simplicity only dephasing of one state and describe this by including relaxation terms in the master equation

$$\dot{\rho} = -\frac{i}{\hbar}[H, \rho] - \begin{bmatrix} 0 & \Gamma_0\rho_{01} & \Gamma_0\rho_{0e} & \Gamma_0\rho_{02} \\ \Gamma_0\rho_{10} & 0 & 0 & 0 \\ \Gamma_0\rho_{e0} & 0 & 0 & 0 \\ \Gamma_0\rho_{20} & 0 & 0 & 0 \end{bmatrix}. \quad (4.6)$$

One can verify that (4.6) is on the Lindblad form [Eq. (4.1)] with a single Lindblad operator, $C_0 = \sqrt{2\Gamma_0}|0\rangle\langle 0|$. The operator is not unique and it is possible to choose other operators yielding (4.6), but working with just one operator simplifies the analysis. Given C_0 we find $H' = -i\hbar\Gamma_0|0\rangle\langle 0|$ and with the closed system Hamiltonian in (3.15) we write the non-Hermitian Hamiltonian

$$\tilde{H}(t) = \frac{\hbar}{2} \begin{bmatrix} -2i\Gamma_0 & 0 & A_0(t) & 0 \\ 0 & 0 & A_1(t)e^{i\varphi_{01}} & 0 \\ A_0(t) & A_1(t)e^{-i\varphi_{01}} & 0 & A_2(t)e^{-i\varphi_2(t)} \\ 0 & 0 & A_2(t)e^{i\varphi_2(t)} & 0 \end{bmatrix}. \quad (4.7)$$

Propagating (4.7) yields the no-jump evolution, which we describe in chapter 4.2. Jump traces, where the system is projected onto the state $C_0|\psi(t_j)\rangle \propto |0\rangle$ at the instant of time t_j , are considered in chapter 4.3.

4.2 Non-Hermitian no-jump evolution

We first aim to solve the no-jump evolution and to this end it is advantageous to rewrite (4.7) in the interaction picture with respect to $H' = -i\hbar\Gamma_0|0\rangle\langle 0|$,

$$\tilde{H}_I(t) = \frac{\hbar}{2} \begin{bmatrix} 0 & 0 & A_0(t)e^{\Gamma_0(t-t_i)} & 0 \\ 0 & 0 & A_1(t)e^{i\varphi_{01}} & 0 \\ A_0(t)e^{-\Gamma_0(t-t_i)} & A_1(t)e^{-i\varphi_{01}} & 0 & A_2(t)e^{-i\varphi_2(t)} \\ 0 & 0 & A_2(t)e^{i\varphi_2(t)} & 0 \end{bmatrix}. \quad (4.8)$$

The subscript I indicates that the evolution is described in the interaction picture. The Hamiltonian is non-Hermitian due to the Γ_0 -exponents and in order to determine the geometric phases we follow the procedure of [54]. We diagonalise H_I and find the eigenvalues

$$\omega_I^\pm = \pm \frac{1}{2} \sqrt{A_0^2 + A_1^2 + A_2^2}, \quad \omega_I^{D_i} = 0 \quad (i = 1, 2), \quad (4.9)$$

and the right (subscript r) and left (subscript l) eigenvectors

$$\begin{aligned} |\pm_r\rangle_I &= \frac{1}{\sqrt{2}} \left[\sin \theta_H(t) (\sin \theta_{01} e^{\Gamma_0(t-t_i)} |0\rangle + \cos \theta_{01} e^{i\varphi_{01}} |1\rangle) \right. \\ &\quad \left. \mp |e\rangle + \cos \theta_H(t) e^{i\varphi_2(t)} |2\rangle \right], \\ |D_{1r}\rangle_I &= -\cos \theta_H(t) (\sin \theta_{01} e^{\Gamma_0(t-t_i)} |0\rangle + \cos \theta_{01} e^{i\varphi_{01}} |1\rangle) + \sin \theta_H(t) e^{i\varphi_2(t)} |2\rangle, \\ |D_{2r}\rangle_I &= \cos \theta_{01} e^{\Gamma_0(t-t_i)} |0\rangle - \sin \theta_{01} e^{i\varphi_{01}} |1\rangle, \\ {}_I\langle \pm_l| &= \frac{1}{\sqrt{2}} \left[\sin \theta_H(t) (\sin \theta_{01} e^{-\Gamma_0(t-t_i)} \langle 0| + \cos \theta_{01} e^{-i\varphi_{01}} \langle 1|) \right. \\ &\quad \left. \mp \langle e| + \cos \theta_H(t) e^{-i\varphi_2(t)} \langle 2| \right], \\ {}_I\langle D_{1l}| &= -\cos \theta_H(t) (\sin \theta_{01} e^{-\Gamma_0(t-t_i)} \langle 0| + \cos \theta_{01} e^{-i\varphi_{01}} \langle 1|) + \sin \theta_H(t) e^{-i\varphi_2(t)} \langle 2|, \\ {}_I\langle D_{2l}| &= \cos \theta_{01} e^{-\Gamma_0(t-t_i)} \langle 0| - \sin \theta_{01} e^{-i\varphi_{01}} \langle 1|, \end{aligned} \quad (4.10)$$

where θ_{01} , θ_H , φ_{01} and φ_2 are as in the closed system case, see (3.16)-(3.18). The left and right eigenvectors fulfil the biorthonormal condition $\langle i_l | j_r \rangle_I = \delta_{i,j}$ [55].

Initially ($t = t_i$) the eigenvectors of the open system (4.10) coincide with the eigenvectors of the closed system (3.20), and the initial state of the open system is simply the initial state of the closed system,

$$\begin{aligned} |\psi(t_i)\rangle_I &= C_{D_1}^o(t_i) |D_{1r}(t_i)\rangle_I + C_{D_2}^o(t_i) |D_{2r}(t_i)\rangle_I \\ &= C_{D_1}(t_i) |D_1(t_i)\rangle + C_{D_2}(t_i) |D_2(t_i)\rangle, \end{aligned} \quad (4.11)$$

where $\{\cdot\}^o$ denotes the open system coefficients. The adiabatic STIRAP evolution ensures that the system remains within the subspace spanned by $\{|D_{1r}(t)\rangle_I, |D_{2r}(t)\rangle_I\}$. Inserting (4.11) into the time-dependent Schrödinger equation gives a set of differential equations for the coefficients

$$\begin{aligned}\dot{C}_{D_1}^o &= -(\Gamma_0 \cos^2 \theta_H \sin^2 \theta_{01} + i\dot{\varphi}_2 \sin^2 \theta_H)C_{D_1}^o + \Gamma_0 \cos \theta_H \sin \theta_{01} \cos \theta_{01} C_{D_2}^o \\ \dot{C}_{D_2}^o &= \Gamma_0 \cos \theta_H \sin \theta_{01} \cos \theta_{01} C_{D_1}^o - \Gamma_0 \cos^2 \theta_{01} C_{D_2}^o\end{aligned}\quad (4.12)$$

These can be solved numerically for $C_{D_1}^o$ and $C_{D_2}^o$ and without loss of generality we write the solutions as

$$\begin{aligned}C_{D_1}^o(t) &= e^{-\Gamma_0 \alpha(t)} e^{i\gamma_{1,nj}(t)} C_{D_1}^o(t_i), \\ C_{D_2}^o(t) &= e^{-\Gamma_0 \beta(t)} e^{i\gamma_{2,nj}(t)} C_{D_2}^o(t_i),\end{aligned}\quad (4.13)$$

and expand the wave function as

$$|\psi_{nm}(t)\rangle_I = e^{-\Gamma_0 \alpha(t)} e^{i\gamma_{1,nj}(t)} C_{D_1}^o(t_i) |D_{1r}(t)\rangle_I + e^{-\Gamma_0 \beta(t)} e^{i\gamma_{2,nj}(t)} C_{D_2}^o(t_i) |D_{2r}(t)\rangle_I. \quad (4.14)$$

The two dark states each acquire a complex geometric phase composed by real parts ($\gamma_{1,nj}$ and $\gamma_{2,nj}$) and imaginary parts ($\Gamma_0 \alpha(t)$ and $\Gamma_0 \beta(t)$) parameterised by the dephasing rate, Γ_0 . When $\Gamma_0 \rightarrow 0$ the differential equation in (4.12) reduces to the closed system equations in (3.22).

As an example we choose an initial state $|\psi_i\rangle = |0\rangle$ and apply the pulse sequence in Fig. 3.1(b) with parameters leading to $\theta_{01} = \frac{\pi}{8}$, $\phi_{01} = \pi$ and $\gamma_H = -\pi$ (see details in caption of Fig. 4.1). As discussed in chapter 3.2.2 this evolution corresponds to the Hadamard gate (3.30) for the closed system. In Fig. 4.1 we show the evolution of the phases as a function of time for different values of the dephasing rate, Γ_0 . The real geometric phases $\gamma_{1,nj}$ (black) and $\gamma_{2,nj}$ (blue) are unaffected by the dephasing and their values are, on the scale of the figure, identical to the analytical result for the closed system ($\gamma_{1,nj} = \gamma_H$, $\gamma_{2,nj} = 0$), which are marked with crosses in Fig. 4.1. The exponents α (green) and β (red) are also almost unaffected by the dephasing rate. The results for $\Gamma_0 \tau = 10^{-5}$ and $\Gamma_0 \tau = 10^{-3}$ (solid) are identical while increasing the dephasing to $\Gamma_0 \tau = 10^{-1}$ (dashed) gives only a small deviation. Experimentally, dephasing rates can be kept below $\Gamma_0 \tau = 10^{-3}$ and for these values of Γ_0 , α and β are unaffected by the dephasing rate and hence the imaginary parts of the phases $\Gamma_0 \alpha$ and $\Gamma_0 \beta$ scale linearly with the dephasing rate. It should be noted that the values of α and β depend on the initial state while $\gamma_{1,nj}$ and $\gamma_{2,nj}$ are independent. Going back to the Schrödinger picture yields

$$\begin{aligned}|\psi_{nm}(t)\rangle &= e^{-\Gamma_0(t-t_i)} |0\rangle \langle 0| [e^{-\Gamma_0 \alpha} e^{i\gamma_{1,nj}} C_{D_1}^o(t_i) |D_{1r}\rangle_I \\ &\quad + e^{-\Gamma_0 \beta} e^{i\gamma_{2,nj}} C_{D_2}^o(t_i) |D_{2r}\rangle_I].\end{aligned}\quad (4.15)$$

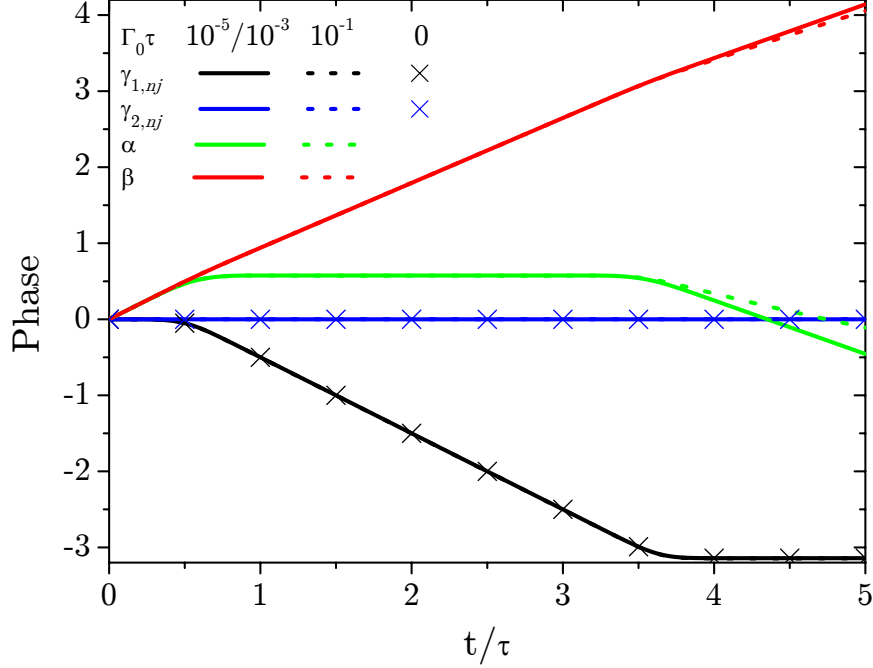


Figure 4.1: Time evolution of $\gamma_{1,nj}$, $\gamma_{2,nj}$, α and β for different dephasing rates, Γ_0 . The calculations were made with \sin^2 pulses (2.23) and all parameters are given in units of the pulse width, τ : $\varphi_2 = t/\tau$, $A_{\max,0}\tau/2\pi = 300$, $A_{\max,1} = A_{\max,0}/(\sqrt{2} - 1)$, $A_{\max,2}^2 = A_{\max,0}^2 + A_{\max,1}^2$, $\Delta t/\tau = 1$, and $\Delta T/\tau = \pi$. These parameters lead to $\theta_{01} = \frac{\pi}{8}$, $\phi_{01} = \pi$ and $\gamma_H = -\pi$. Dephasing rates of $\Gamma_0\tau = 10^{-5}$ and $\Gamma_0\tau = 10^{-3}$ (solid) yield identical results, while $\Gamma_0\tau = 10^{-1}$ (dashed) shows a small deviation at $t/\tau \gtrsim 3.5$.

In the $\{|0\rangle, |1\rangle\}$ -basis an initial state in the Schrödinger picture $|\psi(t_i)\rangle = a_i|0\rangle + b_i|1\rangle$ is transferred to a final non-normalised state $|\psi_{nn}(t_f)\rangle = L_i|\psi(t_i)\rangle = a_f|0\rangle + b_f|1\rangle$ with

$$L_i = \begin{bmatrix} L_{i,00} & L_{i,01} \\ L_{i,01}^* & L_{i,11} \end{bmatrix}, \quad (4.16)$$

where

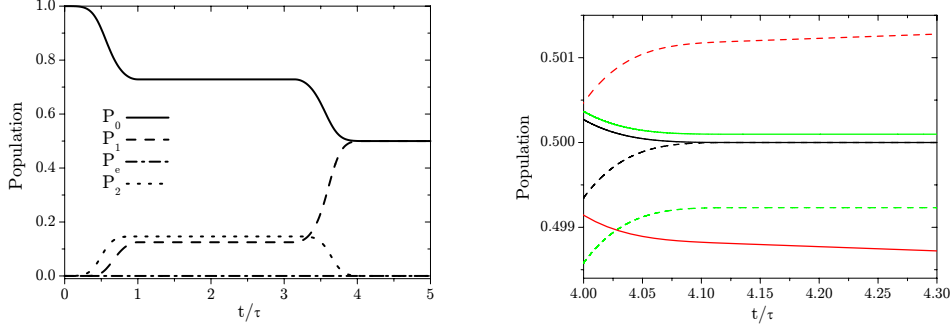
$$\begin{aligned} L_{i,00} &= \cos^2 \theta_{01} e^{-\Gamma_0\beta} e^{i\gamma_{2,nj}} + \sin^2 \theta_{01} e^{-\Gamma_0\alpha} e^{i\gamma_{1,nj}}, \\ L_{i,01} &= \cos \theta_{01} \sin \theta_{01} e^{-i\varphi_{01}} (e^{i\gamma_{1,nj}} e^{-\Gamma_0\alpha} - e^{i\gamma_{2,nj}} e^{-\Gamma_0\beta}), \end{aligned} \quad (4.17)$$

$$L_{i,11} = \sin^2 \theta_{01} e^{-\Gamma_0\beta} e^{i\gamma_{2,nj}} + \cos^2 \theta_{01} e^{-\Gamma_0\alpha} e^{i\gamma_{1,nj}}. \quad (4.18)$$

We note that the phases α and β and therefore also L_i depends on the initial state of the system. The normalisation constant

$$N_i = |C_{D_1}(t_i)|^2 e^{-2\Gamma_0\alpha} + |C_{D_2}(t_i)|^2 e^{-2\Gamma_0\beta}, \quad (4.19)$$

also depends on the initial state, and the final state reads $|\psi(t_f)\rangle = \frac{1}{\sqrt{N_i}} L_i |\psi(t_i)\rangle$. While the phases $\gamma_{1,nj}$ and $\gamma_{2,nj}$ are robust with respect to dephasing, the appearance of the imaginary phases α and β affects the populations. Figure 4.2



(a) Closed system evolution. The populations evolve to $P_0 = 1/2$ and $P_1 = 1/2$ when no dephasing is present.

(b) Final part of the populations when no dephasing is present (black) and with dephasing ($\Gamma_0\tau = 10^{-3}$) calculated from the master equation (green) as well as the no-jump evolution (red).

Figure 4.2 Evolution of the population in the $|0\rangle$ -state (P_0 , solid), the $|1\rangle$ -state (P_1 , dashed), the $|e\rangle$ -state (P_e , dashed-dotted) and the $|2\rangle$ -state (P_2 , dotted) with all population initially in the $|0\rangle$ -state. The calculations were made with \sin^2 pulses [Eq. (2.23)] and all parameters are given in units of the pulse width, τ : $\varphi_2 = t/\tau$, $A_{\max,0}\tau/2\pi = 300$, $A_{\max,1} = A_{\max,0}/(\sqrt{2}-1)$, $A_{\max,2}^2 = A_{\max,0}^2 + A_{\max,1}^2$, $\Delta t/\tau = 1$, and $\Delta T/\tau = \pi$. These parameters lead to $\theta_{01} = \frac{\pi}{8}$, $\phi_{01} = \pi$ and $\gamma_H = -\pi$.

shows the evolution of the population in the four atomic states ($|0\rangle$, $|1\rangle$, $|e\rangle$, $|2\rangle$) with initial state $|\psi_i\rangle = |0\rangle$ and application of the pulse sequence in Fig. 3.1(b) with parameters $\theta_{01} = \pi/8$, $\varphi_{01} = \pi$ and $\gamma_H = -\pi$. In the closed system these parameters lead to an implementation of the Hadamard gate and hence final populations

$$P_0 = (\cos^2 \theta_{01} - \sin^2 \theta_{01})^2 = \frac{1}{2}, \quad (4.20)$$

$$P_1 = 4 \sin^2 \theta_{01} \cos^2 \theta_{01} = \frac{1}{2},$$

as shown in Fig. 4.2(a). When we introduce dephasing, $|\psi_i\rangle = |0\rangle$ leads to final populations found from the no-jump evolution in (4.16) with the approximations $\gamma_{1,nj} = -\pi$ and $\gamma_{2,nj} = 0$,

$$P_0 = \frac{(\cos^2 \theta_{01} e^{-\Gamma_0\beta} - \sin^2 \theta_{01} e^{-\Gamma_0\alpha})^2}{\sin^2 \theta_{01} e^{-2\Gamma_0\alpha} + \cos^2 \theta_{01} e^{-2\Gamma_0\beta}}, \quad (4.21)$$

$$P_1 = \frac{(\sin \theta_{01} \cos \theta_{01} (e^{-\Gamma_0\beta} + e^{-\Gamma_0\alpha}))^2}{\sin^2 \theta_{01} e^{-2\Gamma_0\alpha} + \cos^2 \theta_{01} e^{-2\Gamma_0\beta}}.$$

The deviation from the closed system case is thus determined by the two imaginary geometric phases, $\Gamma_0\alpha$ and $\Gamma_0\beta$. Figure 4.2(b) shows how the evolution is modified. The no-jump traces (red) predict too little population in the $|0\rangle$ state compared to the full solution calculated by the Lindblad master equation (green), because the jump traces, where the population at some instant of time is projected onto the $|0\rangle$ state, is neglected. In order to find the whole solution we therefore need to calculate the jump traces, but for realistic dephasing rates the no-jump calculation predicts the evolution to a good approximation.

4.3 Jump evolution

For the present choice of parameters the system jumps in a small fraction of the Monte Carlo traces to the $|0\rangle$ -state due to $C_0 = \sqrt{2\Gamma_0}|0\rangle\langle 0|$. If a jump occurs at t_j we expand the wave function ($|0\rangle$) in the adiabatic basis of the instantaneous eigenstates

$$\begin{aligned} |\psi(t_j)\rangle_I &= |0\rangle \\ &= -\cos\theta_H(t_j)\sin\theta_{01}|D_{1r}(t_j)\rangle_I + \cos\theta_{01}|D_{2r}(t_j)\rangle_I \\ &\quad + \frac{1}{\sqrt{2}}\sin\theta_H(t_j)\sin\theta_{01}(|+_r(t_j)\rangle_I + |-_r(t_j)\rangle_I). \end{aligned} \quad (4.22)$$

After the jump the evolution is described by the no-jump non-Hermitian Hamiltonian in (4.8). In the adiabatic basis we can describe this evolution by calculating the geometric and dynamic phases acquired by the four states. Adiabaticity ensures that population is only transferred between adiabatic eigenstates with same eigenvalue. The bright eigenstates ($|+_r\rangle, |-_r\rangle$) are separated in energy from each other and from the dark states, such that there is only population transfer between the two dark states. Each bright state is therefore uncoupled to other states and they each acquire a dynamic phase as well as a complex geometric phase that can be calculated directly from (2.8). The complex geometric phase is the same for the two bright states

$$\begin{aligned} \gamma_B &= i \int_{\bar{R}(t_j)}^{\bar{R}(t_f)} \langle \pm_l | \nabla_{\bar{R}} | \pm_r \rangle \cdot d\bar{R} \\ &= \frac{1}{2} i \Gamma_0 \sin^2\theta_{01} \int_{t_j}^t \sin^2\theta_H dt' - \frac{1}{2} \int_{t_j}^t \dot{\varphi}_2 \cos^2\theta_H dt' \\ &\equiv i\Gamma_0\delta + \gamma_b, \end{aligned} \quad (4.23)$$

while the dynamic phase is different for the $|+_r\rangle_I$ and $|-_r\rangle_I$ states,

$$\vartheta_{\pm} = \mp \frac{1}{2} \int_{t_j}^t \sqrt{A_0^2 + A_1^2 + A_2^2} dt'.$$

The two dark states $\{|D_{1r}\rangle, |D_{2r}\rangle\}$ are coupled and the phases they acquire are found from (4.12) with the initial conditions,

$$\begin{aligned} C_{D_1}^o(t_i) &= C_{D_1}^o(t_j) = -\cos\theta_H(t_j)\sin\theta_{01}, \\ C_{D_2}^o(t_i) &= C_{D_2}^o(t_j) = \cos\theta_{01}. \end{aligned} \quad (4.24)$$

The phases are denoted $-\Gamma_0\alpha_a + i\gamma_{1a}$ and $-\Gamma_0\beta_a + i\gamma_{2a}$, where $\{\cdot\}_a$ indicates phases acquired by the dark states after the jump. The wave function at later times in the interaction picture is then written

$$\begin{aligned} |\psi(t)\rangle_I &= -\cos\theta_H(t_j)\sin\theta_{01}e^{-\Gamma_0\alpha_a}e^{i\gamma_{1a}}|D_{1r}\rangle_I \\ &\quad + \cos\theta_{01}e^{-\Gamma_0\beta_a}e^{i\gamma_{2a}}|D_{2r}\rangle_I \\ &\quad + \frac{1}{\sqrt{2}}\sin\theta_H(t_j)\sin\theta_{01}e^{-\Gamma_0\delta}e^{i\gamma_b}e^{i\vartheta_+}|+_r\rangle_I \\ &\quad + \frac{1}{\sqrt{2}}\sin\theta_H(t_j)\sin\theta_{01}e^{-\Gamma_0\delta}e^{i\gamma_b}e^{i\vartheta_-}|_-_r\rangle_I, \end{aligned} \quad (4.25)$$

Going back to the Schrödinger picture and calculating the final populations in the atomic states yields

$$\begin{aligned} P_0 &= \frac{1}{N}|\cos^2\theta_{01}e^{-\Gamma_0\beta_a}e^{i\gamma_{2a}} + \sin^2\theta_{01}\cos\theta_H(t_j)e^{-\Gamma_0\alpha_a}e^{i\gamma_{1a}}|^2, \\ P_1 &= \frac{1}{N}\sin^2\theta_{01}\cos^2\theta_{01}|e^{-\Gamma_0\beta_a}e^{i\gamma_{2a}} - \cos\theta_H(t_j)e^{-\Gamma_0\alpha_a}e^{i\gamma_{1a}}|^2, \\ P_e &= \frac{1}{N}\sin^2\theta_{01}\sin^2\theta_H(t_j)e^{-2\Gamma_0\delta}\sin^2\vartheta_-, \\ P_2 &= \frac{1}{N}\sin^2\theta_{01}\sin^2\theta_H(t_j)e^{-2\Gamma_0\delta}\cos^2\vartheta_-, \end{aligned} \quad (4.26)$$

where the normalisation constant is given as

$$N = \sin^2\theta_{01}\cos^2\theta_H(t_j)e^{-2\Gamma_0\alpha} + \cos^2\theta_{01}e^{-2\Gamma_0\beta} + \sin^2\theta_{01}\sin^2\theta_H(t_j)e^{-2\Gamma_0\delta}, \quad (4.27)$$

and phases are only acquired from the latest jump time, t_j . The final populations can in this way be calculated after each Monte Carlo trace and the deviations from the closed system case can be explained by the complex geometric phases acquired by the adiabatic states.

When all complex geometric phases are carefully taken into account an average over many traces reproduces the numerical solution of the master equation in (4.6). Figure 4.2(b) showed how the final populations calculated using only the no-jump evolution deviated from the full density matrix solution. In Fig. 4.3 we show how this can be corrected taking into account also jump traces. The calculations are made with parameters which implement

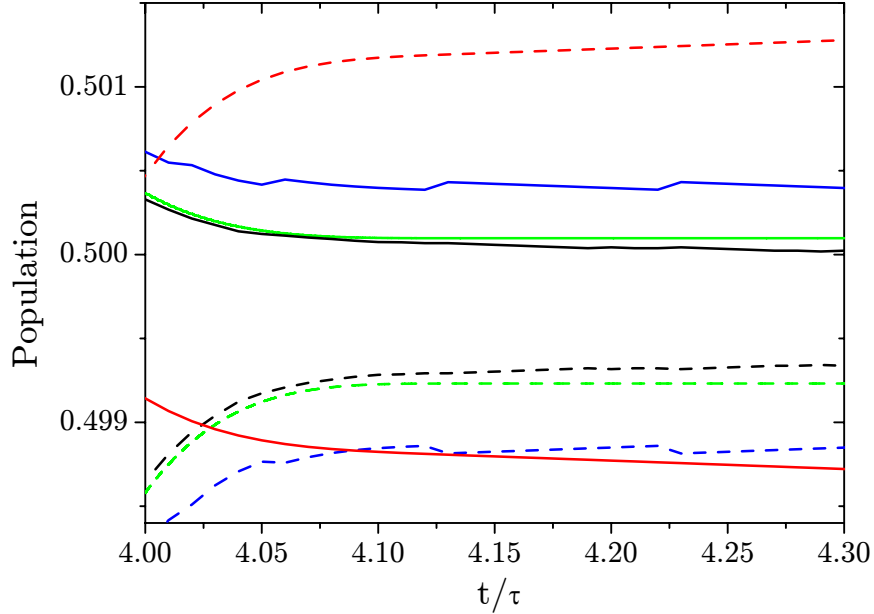


Figure 4.3: Population in the $|0\rangle$ -state (solid) and the $|1\rangle$ -state (dashed), when the system is subject to dephasing, $\Gamma_0\tau = 10^{-3}$. The graph shows only the final part of the time evolution, where the differences can be distinguished. The green curve shows the solution of the master equation [Eq. (4.6)], the red curve the no-jump trace, while the last two curves are averages over 10000 (blue) and 200000 (black) jump and no-jump traces. The calculations were made with \sin^2 pulses [Eq. (2.23)] and all parameters are given in units of the pulse width, τ : $\varphi_2 = t/\tau$, $A_{max,0}\tau/2\pi = 300$, $A_{max,1} = A_{max,0}/(\sqrt{2} - 1)$, $A_{max,2}^2 = A_{max,0}^2 + A_{max,1}^2$, $\Delta t/\tau = 1$, and $\Delta T/\tau = \pi$.

the Hadamard gate in the closed system and a dephasing rate $\Gamma_0\tau = 10^{-3}$ (see details in the caption of Fig. 4.3). The no-jump trace (red) deviates from the density matrix calculation (green) on the order of 10^{-3} . An average over 10000 jump and no-jump Monte Carlo traces (blue) reduces the deviation to an order of 10^{-4} , while averaging over 200000 traces (black) reduces it further to an order of 10^{-5} .

4.4 Fidelity of Hadamard gate

The calculated Monte Carlo traces can be used to find the fidelity of the Hadamard gate. For a given initial state $|\psi_i\rangle$ we can determine the fidelity as the overlap between the target (closed-system) wave function $|\psi_0\rangle$ and the final Monte Carlo wave functions (no-jump $|\psi_{nj}\rangle$ or one jump at t_j $|\psi_j(t_j)\rangle$) weighed by the probability for each trace to occur (no-jump P_{nj} or one jump $P_j(t_j)$). The contribution to the fidelity from traces with more than one jump

is negligible for realistic dephasing rates. The fidelity, accordingly reads

$$F_i = P_{nj} |\langle \psi_0 | \psi_{nj} \rangle|^2 + \int P_j(t_j) |\langle \psi_0 | \psi_j(t_j) \rangle|^2 dt_j. \quad (4.28)$$

As a first approximation the fidelity can be calculated neglecting the jump traces

$$F_{i,nj} = P_{nj} |\langle \psi_0 | \psi_{nj} \rangle|^2. \quad (4.29)$$

The no-jump probability is just the norm of the non-normalised no-jump wave function [see Eq. (4.5)] and the fidelity reduces to

$$F_{i,nj} = |\langle \psi_0 | \psi_{nj,nn} \rangle|^2. \quad (4.30)$$

The wave functions are found from (3.29), $|\psi_0\rangle = U|\psi_i\rangle$ and (4.16) combined with a transformation to the Schrödinger picture, $|\psi_{nj,nn}\rangle = e^{-\Gamma_0(t-t_i)|0\rangle\langle 0|} L|\psi_i\rangle$. The overlap between these leads to

$$\begin{aligned} F_{i,nj} &= |\langle \psi_i U_0^\dagger | e^{-\Gamma_0(t-t_i)|0\rangle\langle 0|} L \psi_i \rangle|^2 \\ &= e^{-2\Gamma_0\alpha_{nj}} |C_{D_1}^i|^4 + e^{-2\Gamma_0\beta_{nj}} |C_{D_2}^i|^4 \\ &\quad + 2e^{-\Gamma_0(\alpha_{nj}+\beta_{nj})} |C_{D_1}^i|^2 |C_{D_2}^i|^2 \cos(\gamma_{1,nj} - \gamma_{2,nj} - \gamma_H), \end{aligned} \quad (4.31)$$

where we write the initial coefficients, $C_{D_1}^o(t_i) = C_{D_1}^i$ and $C_{D_2}^o(t_i) = C_{D_2}^i$.

The second part of the fidelity comes from traces with one jump at the instant t_j . Also here the fidelity can be calculated directly from the non-normalised wave function,

$$F_{i,j} = |\langle \psi_0 | \psi_{j,nn} \rangle|^2. \quad (4.32)$$

$|\psi_{j,nn}\rangle$ is calculated as described in (4.25) with the modification that the wave function is not normalised after a jump, and both the norm-loss before the jump as well as the $\sqrt{2\Gamma_0}$ factor obtained in the jump are kept in order to get the true probability distribution. The overlap is calculated in the Schrödinger picture and is determined by the geometric phases acquired by $|D_{1r}\rangle_I$ ($-\Gamma_0\alpha_b + i\gamma_{1b}$, $-\Gamma_0\alpha_a + i\gamma_{1a}$) and $|D_{2r}\rangle_I$ ($-\Gamma_0\beta_b + i\gamma_{2b}$, $-\Gamma_0\beta_a + i\gamma_{2a}$) before the jump denoted by $\{.\}_b$ and after denoted by $\{.\}_a$. The fidelity from the jump traces is proportional to $\sqrt{2\Gamma_0}^2$ because this factor is obtained by the wave function during a jump,

$$F_{i,j} = 2\Gamma_0 \int \xi_{i,j}(\alpha_b, \gamma_{1b}, \alpha_a, \gamma_{1a}, \beta_b, \gamma_{2b}, \beta_a, \gamma_{2a}) dt_j, \quad (4.33)$$

where $\xi_{i,j}(\alpha_b, \gamma_{1b}, \alpha_a, \gamma_{1a}, \beta_b, \gamma_{2b}, \beta_a, \gamma_{2a})$ depends on the geometric phases in the jump traces with a jump at t_j . Traces with more than one jump will contribute with terms proportional to higher orders of Γ_0 and are therefore neglected. Also $F_{i,j}$ will contain terms proportional to higher orders of Γ_0 and

keeping only terms to first order in Γ_0 we approximate $e^{-\Gamma_0\alpha_i} \approx 1$, $e^{-\Gamma_0\beta_i} \approx 1$. The fidelity thus only depends on the real phases,

$$F_{i,j} = 2\Gamma_0 \int \xi_{i,j}(\gamma_{1b}, \gamma_{1a}, \gamma_{2b}, \gamma_{2a}) dt_j, \quad (4.34)$$

and to first order in Γ_0 only zeroth order terms in γ_{1b} , γ_{1a} , γ_{2b} and γ_{2a} contribute. These can be found analytically by solving the imaginary part of (4.12),

$$\begin{aligned} \gamma_{1b}^{(0)} &= - \int_{t_i}^{t_j} \sin \theta_H(t_j) \dot{\varphi}_2 dt, \\ \gamma_{1a}^{(0)} &= - \int_{t_j}^{t_f} \sin \theta_H(t_j) \dot{\varphi}_2 dt, \\ \gamma_{2b}^{(0)} &= \gamma_{2a}^{(0)} = 0, \end{aligned} \quad (4.35)$$

and we write the the jump fidelity,

$$F_{i,j} = 2\Gamma_0 \int \xi_{i,j}(\gamma_{1b}^0, \gamma_{1a}^0) dt_j. \quad (4.36)$$

The no-jump fidelity in (4.31) is also simplified keeping only first order terms. This corresponds to, $e^{-\Gamma_0\alpha_{nj}} \approx 1 - \Gamma_0\alpha_{nj}$, $e^{-\Gamma_0\beta_{nj}} \approx 1 - \Gamma_0\beta_{nj}$ and $\cos(\gamma_{1,nj} - \gamma_{2,nj} - \gamma_H) \approx \cos(\gamma_{1,nj}^0 - \gamma_{2,nj}^0 - \gamma_H) = 1$, because the same calculation that gave (4.35) yields $\gamma_{1,nj}^0 = \gamma_H$ and $\gamma_{2,nj}^0 = 0$. With these approximations (4.31) reduces to,

$$F_{i,nj} = 1 - 2\Gamma_0(\alpha_{nj}|C_{D_1}^i|^2 + \beta_{nj}|C_{D_2}^i|^2), \quad (4.37)$$

and we write the total fidelity for a given initial state

$$\begin{aligned} F_i &= F_{i,nj} + F_{i,j} \\ &= 1 - 2\Gamma_0(\alpha_{nj}|C_{D_1}^i|^2 + \beta_{nj}|C_{D_2}^i|^2) + 2\Gamma_0 \int \xi_{i,j}(\gamma_{1b}^0, \gamma_{1a}^0) dt_j. \end{aligned} \quad (4.38)$$

The fidelity determined from the Monte Carlo traces can be compared to the Uhlmann state fidelity calculated from the final closed system density matrix ρ_0 and the final open system density matrix $\rho_{(\Gamma_0)}$ [56],

$$F_{\rho,i} = \left(\text{Tr} \sqrt{\rho_0^{1/2} \rho_{(\Gamma_0)} \rho_0^{1/2}} \right)^2. \quad (4.39)$$

Both F_i and $F_{\rho,i}$ give the fidelity for a given initial state and the average fidelity can be found by integrating over the surface of the Bloch sphere

$$F = \frac{1}{4\pi} \int F_i d\Omega. \quad (4.40)$$

This averaging procedure can be simplified to only averaging over the six axial pure initial states on the Bloch sphere, $\Lambda = \{|0\rangle, |1\rangle, \frac{1}{\sqrt{2}}(|0\rangle + |1\rangle), \frac{1}{\sqrt{2}}(|0\rangle - |1\rangle), \frac{1}{\sqrt{2}}(|0\rangle + i|1\rangle), \frac{1}{\sqrt{2}}(|0\rangle - i|1\rangle)\}$ [57],

$$F = \frac{1}{6} \sum_{|\psi_i\rangle \in \Lambda} F_i. \quad (4.41)$$

Averaging over the jump part of (4.38) is straightforward because the real phases ($\gamma_{1b}^0, \gamma_{1a}^0$) do not depend on the initial state, while the imaginary phases (α_{nj}, β_{nj}) differ and we write the final average fidelity to first order in Γ_0 ,

$$F_i = 1 - \frac{2}{6}\Gamma_0 \sum_{|\psi_i\rangle \in \Lambda} (\alpha_{nj}|C_{D_1}^i|^2 + \beta_{nj}|C_{D_2}^i|^2) \quad (4.42)$$

$$+ \frac{4}{6}\Gamma_0 \int_{t_i}^{t_f} (\sin^2 \theta_{01} \cos^2 \theta_H(t_j) + \cos^2 \theta_{01})^2 dt_j.$$

In Fig. 4.4 we show the average fidelity of (4.42) as a function of the dephasing rate, when only the no-jump evolution is taken into account (dashed), and the full solution to first order in Γ_0 (solid). These are compared to the full mas-

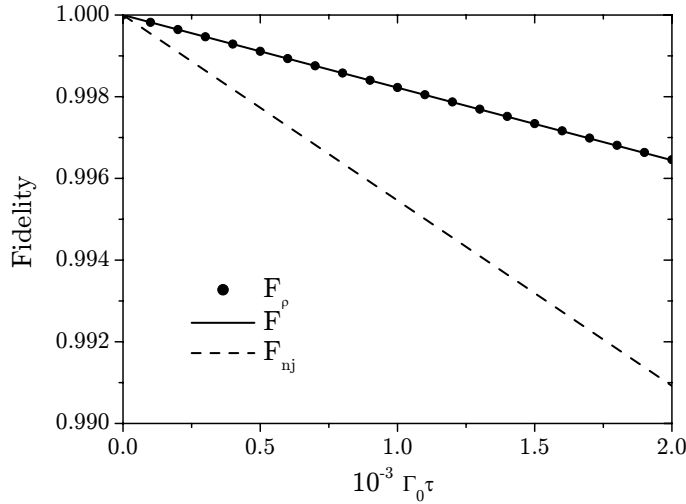


Figure 4.4: Fidelity as a function of the dephasing rate, Γ_0 . The full solution calculated from the density matrix (circles), F_{ρ} [Eq. (4.39)] is compared to the Monte Carlo calculations to first order in Γ_0 (4.42). The dashed curve includes only the no-jump contribution, while the solid curve also take jump traces into account. The calculations were made with \sin^2 pulses [Eq. (2.23)] and all parameters are given in units of the pulse width, τ : $\varphi_2 = t/\tau$, $A_{max,0}\tau/2\pi = 300$, $A_{max,1} = A_{max,0}/(\sqrt{2}-1)$, $A_{max,2}^2 = A_{max,0}^2 + A_{max,1}^2$, $\Delta t/\tau = 1$, and $\Delta T/\tau = \pi$.

ter equation solution (circles). All fidelities are calculated for the Hadamard gate implemented by the parameters $\theta_{01} = \pi/8$, $\varphi_{01} = \pi$ and $\gamma_H = -\pi$ as in all previous numerical results. The fidelity decreases as expected when the dephasing rate increases, but is still acceptable when the system is subject to realistic dephasing rates. The no-jump results set a lower bound on the fidelity but it is necessary to include traces with one jump in order to get a satisfactory accuracy for realistic dephasing rates. Equation (4.42) shows explicitly how the average fidelity depends on the geometric phases acquired during the no-jump evolution.

4.5 Conclusion

We have shown how the evolution of a system acquiring geometric phases can be described also when dephasing is present. Modifying the closed system analysis to a jump and a no-jump evolution under which the wave function acquires complex geometric phases. This method has the advantage that we retain the analytical insight given by the adiabatic following of eigenstates and the phases they acquire. The no-jump trace gives a first approximation to the evolution, but jump traces has to be included in order to achieve a sufficient accurate result consistent with a density matrix calculation.

Chapter 5

Entangling Rydberg atoms

Rydberg atoms are neutrals with a highly excited electron in so-called Rydberg states. The Rydberg atoms have played an important role in atomic physics, because they possess a range of interesting properties. The electron can be in states that resemble classical orbits, the Rydberg states have large transition dipole moments and the Rydberg atoms are easily manipulated by external magnetic or electric fields [58]. From a quantum information point of view the Rydberg states are interesting since they have relatively long lifetimes and because the large dipole moments induce a dipole-dipole interaction inhibiting excitation of more than one atom to the Rydberg state. This Rydberg excitation blockade can be used as the coupling between qubits required to implement two-qubit gates.

In this chapter we will combine the Rydberg blockade and the rapid adiabatic laser pulse sequence known from STIRAP. We show how the adiabatic passage in the presence of the Rydberg blockade can be used to steer two atoms into a maximally entangled state and implement two-bit quantum gates. For many atoms, the excitation blockade leads to an effective implementation of collective-spin and Jaynes-Cummings-like Hamiltonians, and we show that the adiabatic passage can be used to generate collective $J_x = 0$ states and Greenberger-Horne-Zeilinger states of tens of atoms. The work presented in this chapter was published in [V].

5.1 Rydberg atoms

Progress in trapping and manipulating neutral atoms in dipole traps has made it possible to work towards a quantum computer using the hyperfine sublevel of the ground state in alkali atoms (typically Caesium or Rubidium) to encode qubits. The atoms are confined in optical dipole traps and can be prepared in arrays with access to individual addressing of each atom [44, 59]. The optical traps can be moved and by overlapping two traps the atoms can be transferred

from one trap to another without loss of coherence [60]. Single qubit rotations are performed driving two-photon Raman transitions [61,62].

The single valence electron in a trapped alkali atom is excited to a Rydberg state with large principal quantum number, n . Two or more atoms will experience the Rydberg excitation blockade, which we discuss in further detail below. Experimentally, the challenge at this point is demonstrating a two-qubit gate relying on the Rydberg blockade and most recent an important progress was made, when the excitation of one atom to a Rydberg state with $n = 79$ was seen to block excitation of another [63]. The next step is now to use the blockade to implement a two-qubit gate. The first proposals for this type of gate [41,64] were dynamic, while the work presented here relies on adiabatic evolution and geometric phases. Before describing our scheme to create two-qubit gates as well as many-atom entanglement we will briefly discuss the level structure of the Rydberg atoms considered, the application of the STIRAP pulse sequence, and the Rydberg excitation blockade.

5.1.1 STIRAP applied to ladder-systems in Rydberg atoms

We consider atoms with two lower levels and a Rydberg state in a ladder structure coupled by two resonant laser fields with Rabi frequencies Ω_1 and Ω_r as shown in Fig. 5.1(a). The STIRAP process applies the counter-intuitive pulse sequence of Fig. 5.1(b) and the mathematics is exactly as described for the lambda system in chapter 2.2.1 [38]. For a single atom the process therefore transfers the population from the ground state $|1\rangle$ to the Rydberg

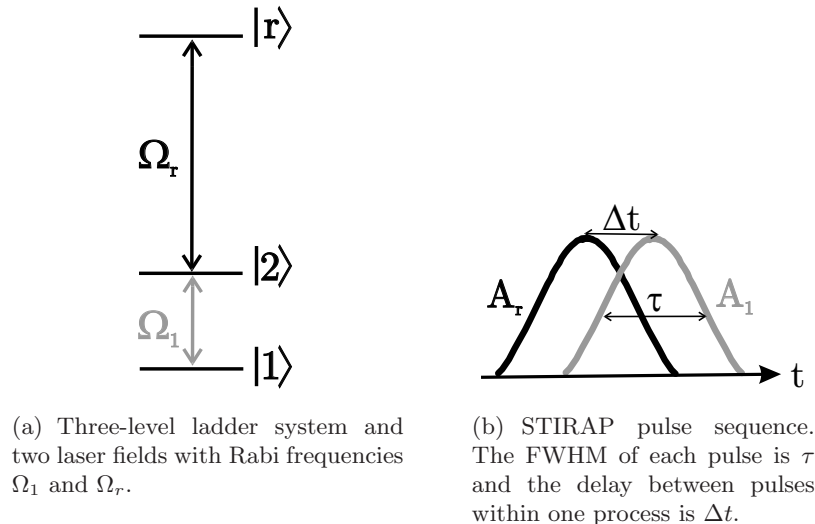


Figure 5.1

state $|r\rangle$ by adiabatically following the usual dark state

$$|D_1\rangle = \cos\theta|1\rangle - \sin\theta e^{i\phi_r}|r\rangle, \quad (5.1)$$

where $\tan\theta = A_1/A_r$ expresses the relative strength and ϕ_r the relative phase of the two laser fields. We assume that $|1\rangle$ and $|2\rangle$ are long lived states, but $|r\rangle$ has a finite lifetime, which may affect the gate fidelity. This could for example be achieved by implementing $|1\rangle$ and $|2\rangle$ as hyperfine states in Rubidium or Caesium. The lifetime of the Rydberg state, τ_r , increases with n as shown in Fig. 5.2 for Rubidium¹. Here $n > 70$ ensures $\tau_r \gtrsim 100 \mu\text{s}$ implying that gates should last only a few microseconds.

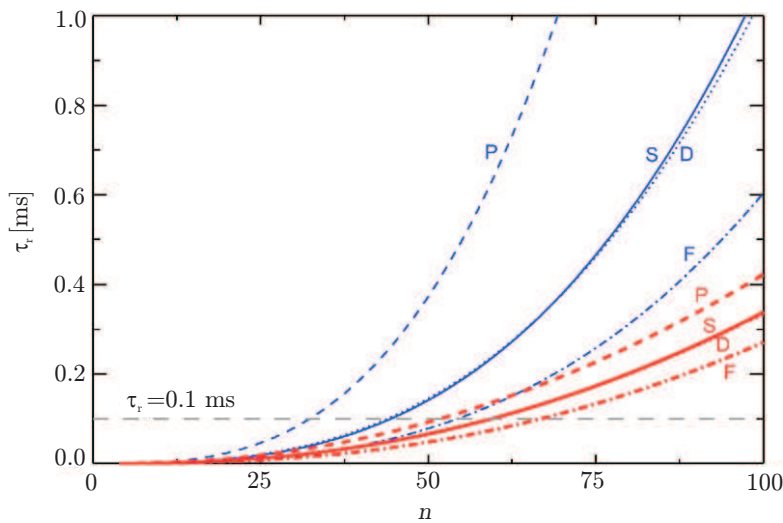


Figure 5.2: Lifetime of the excited S,P,D and F states of Rubidium as a function of principal quantum number, n . The red curves show results for atoms in a cryogenic environment ($T=0$ K) while the blue curves show results at room temperature ($T=300$ K). The figure is reproduced from [65] by courtesy of Mark Saffman.

5.1.2 Rydberg excitation blockade

The large transition dipole moments of the highly excited Rydberg states lead to strong interactions between atoms a few micrometres apart. When the interaction is present, double excited states are shifted in energy, and a laser field resonant with a single atom transition can not excite two atoms because it will be off-resonant. A single excitation will therefore suppress excitation of other atoms within reach of the dipole-dipole interaction. Calculating the exact value of the energy shift is not an easy task because it involves many states. Experimentally, it is important to choose proper states

¹The lifetimes of Rydberg states in Caesium are similar.

where the blockade is large and it can even be important to choose the right Zeeman substates [66]. One example of suitable states are the two-atomic states $|ns\rangle|ns\rangle$ and $|np\rangle|(n-1)p\rangle$. They are nearly degenerate and the dipole-dipole interaction therefore mixes the product states leading to new two-atom states that are shifted in energy [67] as indicated in Fig. 5.3. This leads to the second excitation being off-resonant and therefore strongly suppressed. When the dipole-dipole interaction is large the energy shift, E , is just given

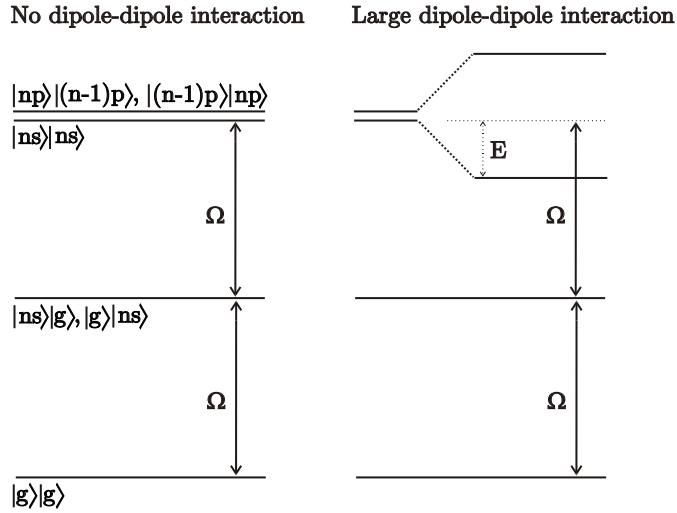


Figure 5.3: Effect of the dipole-dipole interaction. If there is no dipole-dipole interaction between the two atoms, a laser (Ω) which resonantly excites one atom from a ground state $|g\rangle$ to an excited s-state $|ns\rangle$ will also be resonant on the second transition between states with one excitation ($|ns\rangle|g\rangle$, $|g\rangle|ns\rangle$) and two excitations ($|ns\rangle|ns\rangle$). The large dipole-dipole interaction mixes the two-atomic $|ns\rangle|ns\rangle$ -state with the near resonant $|np\rangle|(n-1)p\rangle$, $|(n-1)p\rangle|np\rangle$ -states and the new two atom states are shifted in energy causing the the second excitation to become off-resonant.

by the strength of the interaction. The dipole-dipole interaction strength for the states in Fig. 5.3 was calculated in [68] for Caesium and shown in Fig. 5.4 as a function of the separation of the atoms². An interaction strength above $2\pi \cdot 100$ MHz is achieved when atoms are separated less than $5 \mu\text{m}$. The accompanying suppression of excitation for n up to 80 [69, 70] and the influence of the excitation blockade on coherent collective dynamics [71] was observed in cold gases. Most recent the blockade was also observed for single atoms in dipole traps for Rydberg states with $n = 79$ [63].

²The dipole-dipole interaction strength is similar in Rubidium.

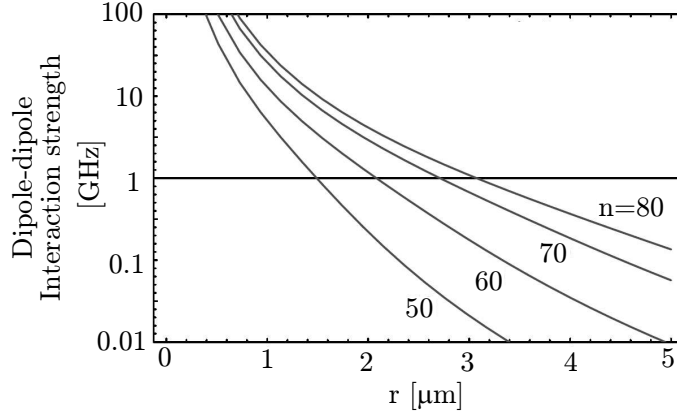


Figure 5.4: Dipole-dipole interaction as a function of the atom separation, r , for Rydberg states in Caesium with principal quantum number, $n = 50 - 80$. The figure is reproduced from [68] by courtesy of Klaus Mølmer.

5.2 Entangling two atoms

We now turn to describing an adiabatic scheme for creation of entanglement and quantum gates between neutral atoms utilising the long range dipole-dipole interaction combined with STIRAP processes. We first consider two atoms, initially in the product state $|11\rangle$ and subject to the same interaction with the two resonant laser fields Ω_1 and Ω_r . The evolution preserves the symmetry under interchange of atoms, and it is therefore sufficient to consider the Hamiltonian in the symmetric two-atomic basis,

$\{|11\rangle, \frac{1}{\sqrt{2}}(|1r\rangle + |r1\rangle), \frac{1}{\sqrt{2}}(|12\rangle + |21\rangle), |rr\rangle, \frac{1}{\sqrt{2}}(|2r\rangle + |r2\rangle), |22\rangle\}$. Here the Hamiltonian reads,

$$H(t) = \frac{\hbar}{2} \begin{bmatrix} 0 & 0 & \sqrt{2}\Omega_1^* & 0 & 0 & 0 \\ 0 & 0 & \Omega_r^* & 0 & \Omega_1^* & 0 \\ \sqrt{2}\Omega_1 & \Omega_r & 0 & 0 & 0 & \sqrt{2}\Omega_1^* \\ 0 & 0 & 0 & 2E/\hbar & \sqrt{2}\Omega_r^* & 0 \\ 0 & \Omega_1 & 0 & \sqrt{2}\Omega_r & 0 & \sqrt{2}\Omega_r^* \\ 0 & 0 & \sqrt{2}\Omega_1 & 0 & \sqrt{2}\Omega_r & 0 \end{bmatrix}, \quad (5.2)$$

where E denotes the energy shift of the state $|rr\rangle$ due to the dipole-dipole interaction. This Hamiltonian has one dark state for the two-atom system,

$$|D_2\rangle = \frac{1}{\sqrt{\cos^4\theta + 2\sin^4\theta}} [(\cos^2\theta - \sin^2\theta)|11\rangle - \cos\theta \sin\theta e^{i\phi_r} (|1r\rangle + |r1\rangle) + \sin^2\theta|22\rangle]. \quad (5.3)$$

We first assume $e^{i\phi_r} = 1$ and apply the counter-intuitive pulse sequence of Fig. 5.1(b). Initially, $\cos\theta = 1$ and the system is in $|D_2\rangle = |11\rangle$. Adiabaticity

ensures that we remain in $|D_2\rangle$ and after the pulses $\sin\theta = 1$ and the system is in

$$|D_2\rangle = \frac{1}{\sqrt{2}}(-|11\rangle + |22\rangle). \quad (5.4)$$

Equation (5.3) shows, that while the STIRAP process in the single atom case ensures that $|2\rangle$ is never populated, due to the Rydberg blockade the pair of atoms are adiabatically steered into a state populating $|22\rangle$. Moreover, (5.4) is a maximally entangled state of the two atoms, generated robustly irrespective of the precise pulse shapes, field strengths and the precise value of the Rydberg interaction energy. Figure 5.5 shows the evolution of populations for

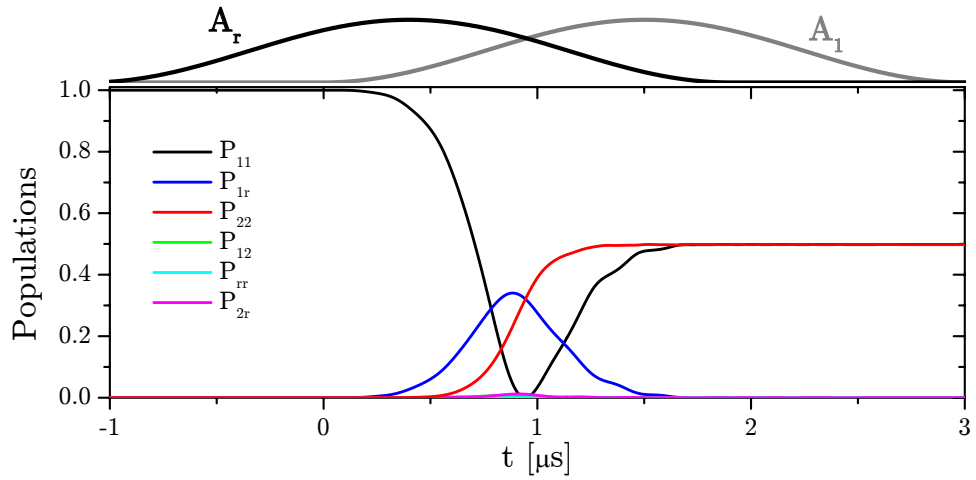


Figure 5.5: Time evolution of the population in the symmetric basis states, $|11\rangle$, $\frac{1}{\sqrt{2}}(|1r\rangle + |r1\rangle)$, $\frac{1}{\sqrt{2}}(|12\rangle + |21\rangle)$, $|rr\rangle$, $\frac{1}{\sqrt{2}}(|2r\rangle + |r2\rangle)$, $|22\rangle$. We propagate the Schrödinger equation with the \sin^2 -pulses defined in (2.23) and parameters $A_{\max,1}/2\pi = A_{\max,r}/2\pi = 10$ MHz, $\Delta t = 1.1$ μs , $\tau = 1.5$ μs , lifetime of the $|r\rangle$ state, $\tau_r = 100$ μs and $E/\hbar = 100 \cdot 2\pi$ MHz

realistic experimental parameters, obtained from a numerical propagation of the Schrödinger equation. The decay due to the finite lifetime of the $|r\rangle$ states, populated during the process, is incorporated as a decay out of the system, whereas the $|1\rangle$ and $|2\rangle$ states are treated as long lived hyperfine sublevels. This implies that if the levels are coupled by single photon transitions, the field coupling $|1\rangle$ and $|2\rangle$ will have a frequency in the radiofrequency range, while the laser field coupling $|2\rangle$ and $|r\rangle$ has a wavelength of approximately 300 nm for Caesium and Rubidium. Experimentally, access to infrared or optical lasers are easier, than the 300 nm required here, and a modification of our scheme allows for the use of such laser systems.

The modified scheme is obtained with two-photon transitions involving four optical fields as sketched in Fig. 5.6. Assuming large detunings (Δ_1 , Δ_{2A} , Δ_{2B} , Δ_r) we can adiabatically eliminate $|e_A\rangle$ and $|e_B\rangle$ as described in

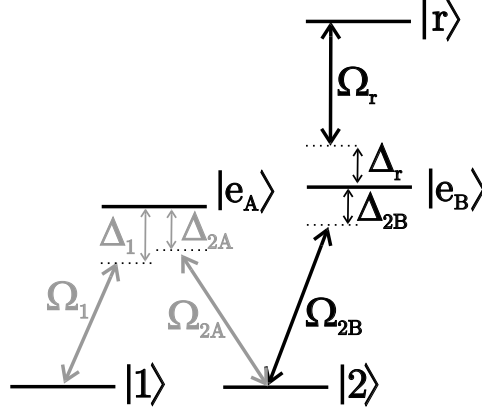


Figure 5.6: Five-level system coupled by four infrared or optical laser fields.

chapter 2.2.3 and find the Hamiltonian for the reduced three level system,

$$H(t) = \frac{\hbar}{2} \begin{bmatrix} \frac{|\Omega_1|^2}{2\Delta_{2A}} - 2(\Delta_{2A} - \Delta_1) & \frac{\Omega_1\Omega_{2A}^*}{2\Delta_{2A}} & 0 \\ \frac{\Omega_1^*\Omega_{2A}}{2\Delta_{2A}} & \frac{|\Omega_{2A}|^2}{2\Delta_{2A}} + \frac{|\Omega_{2B}|^2}{2\Delta_{2B}} & \frac{\Omega_r\Omega_{2B}^*}{2\Delta_{2B}} \\ 0 & \frac{\Omega_r^*\Omega_{2B}}{2\Delta_{2B}} & \frac{|\Omega_r|^2}{2\Delta_{2B}} - 2(\Delta_{2B} - \Delta_r) \end{bmatrix}. \quad (5.5)$$

If the two-photon detunings are now varied such that,

$$2(\Delta_{2A} - \Delta_1) = \frac{|\Omega_1|^2}{2\Delta_{2A}} \quad \text{and} \quad 2(\Delta_{2B} - \Delta_r) = \frac{|\Omega_r|^2}{2\Delta_{2B}}, \quad (5.6)$$

the Hamiltonian reduces to the familiar three level Hamilton (see (2.14) for comparison)

$$H(t) = \frac{\hbar}{2} \begin{bmatrix} 0 & \Omega_{12} & 0 \\ \Omega_{12}^* & \frac{|\Omega_{2A}|^2}{2\Delta_{2A}} + \frac{|\Omega_{2B}|^2}{2\Delta_{2B}} & \Omega_{r2}^* \\ 0 & \Omega_{r2} & 0 \end{bmatrix}, \quad (5.7)$$

with the dark state

$$|D_{ad}\rangle = \frac{A_{r2}(t)}{\sqrt{A_{12}^2(t) + A_{r2}^2(t)}}|1\rangle - \frac{A_{12}(t)}{\sqrt{A_{12}^2(t) + A_{r2}^2(t)}}e^{i\varphi_{ad}(t)}|r\rangle, \quad (5.8)$$

where A_{12} and A_{r2} are the field strengths and φ_{ad} the relative phase of the Raman Rabi frequencies,

$$\Omega_{12} = \frac{\Omega_1\Omega_{2A}^*}{2\Delta_{2A}} \quad \text{and} \quad \Omega_{r2} = \frac{\Omega_r\Omega_{2B}^*}{2\Delta_{2B}}. \quad (5.9)$$

The five level scheme of course has the disadvantage that it involves four laser fields and in addition the two-photon detuning must be controlled time

dependent, but it should be straight forward to implement using for example acousto optical modulators. The advantage is the easier access to the necessary laser wavelengths. Both implementations require that the laser phases are stable.

To investigate the criterion of adiabaticity and the role of the Rydberg interaction energy E , in Fig. 5.7, we show the fidelity of the creation of the entangled state, $F = |\langle D_2 | \psi_f \rangle|^2$, where $|\psi_f\rangle$ is the final state calculated by propagation of the state vector with the time-dependent Hamiltonian (5.2). The simulations show that, as long as E is large enough to prevent population of states with more than one Rydberg excitation, the exact value of E is not important. With peak Rabi frequencies $A_{\max,1}/2\pi = A_{\max,r}/2\pi = 10$ MHz, a Rydberg energy shift of $E/\hbar = 50 \cdot 2\pi$ MHz is sufficient. The time span where $|r\rangle$ is populated is determined by the pulse width and it is desirable to use the smallest possible width that does not violate adiabaticity, yielding a total time of entanglement generation of 3-4 μs , which is short compared with the radiative lifetime of the highly excited Rydberg state $\gtrsim 100 \mu\text{s}$.

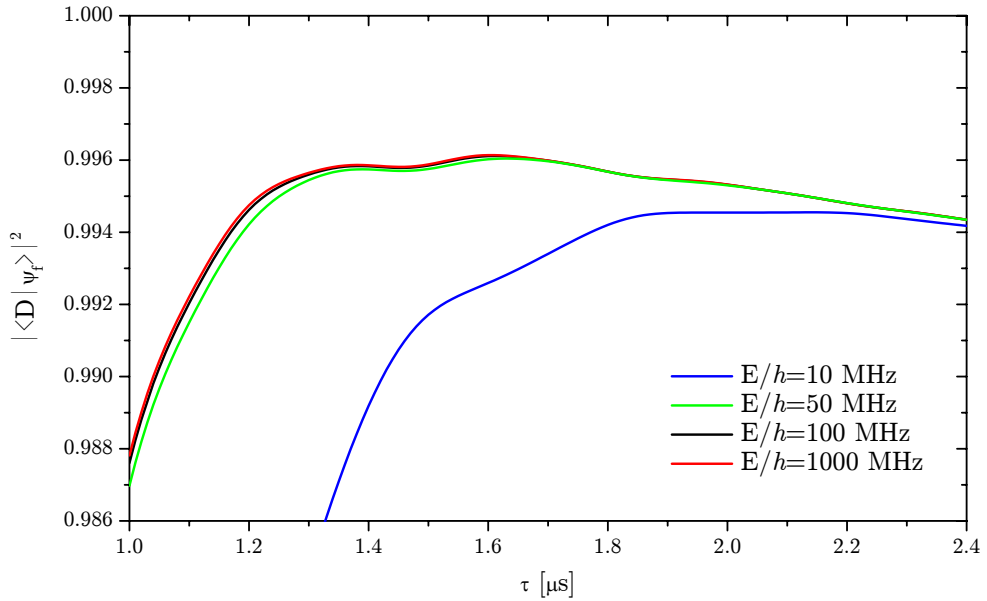


Figure 5.7: Fidelity of the entanglement creation as a function of pulse width for different values of dipole-dipole interaction, E . $|\psi_f\rangle$ was found by propagating (5.2) with initial state $|11\rangle$. We show the norm square of the overlap with the target state $|D_2\rangle$. The laser pulses are modelled by the \sin^2 -pulses in (2.23) and with parameters $A_{\max,1}/2\pi = A_{\max,r}/2\pi = 10$ MHz, $\Delta t = 1.1$ MHz and $\tau_r = 100$ MHz.

5.2.1 Two-qubit phase gate

The two-atom entanglement scheme can be modified to create a two-qubit phase gate. To this end we apply a second STIRAP sequence with pulses in reversed order as shown in Fig. 5.8. The second pulse pair transfers population back to $|11\rangle$. The Rabi frequencies now have a non-vanishing relative phase $\phi_r(t)$ between Ω_1 and Ω_r and the dark state (5.3) acquires the geometric phase [19]

$$\gamma_2 = - \int \frac{\cos^2 \theta \sin^2 \theta}{\cos^4 \theta + 2 \sin^4 \theta} \dot{\phi}_r dt. \quad (5.10)$$

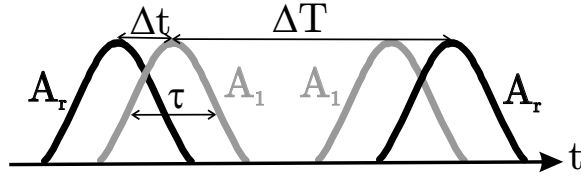


Figure 5.8: Two STIRAP processes separated by ΔT in time.

When we supplement the atomic level scheme with another qubit state $|0\rangle$, which is decoupled from the STIRAP pulses, only the two-qubit register state $|11\rangle$ will acquire the geometric phase, γ_2 . The $|00\rangle$ state will be unaffected while for the $|01\rangle$ and $|10\rangle$ states the atom in $|1\rangle$ will follow the single atom dark state (5.1) and acquire the geometric phase found in chapter 3.1,

$$\gamma_1 = - \int \sin^2 \theta \dot{\phi}_r dt. \quad (5.11)$$

This implies the evolution,

$$\begin{aligned} |00\rangle &\rightarrow |00\rangle \\ |01\rangle &\rightarrow e^{i\gamma_1} |01\rangle \\ |10\rangle &\rightarrow e^{i\gamma_1} |10\rangle \\ |11\rangle &\rightarrow e^{i\gamma_2} |11\rangle \end{aligned} \quad (5.12)$$

corresponding to a controlled two-qubit phase gate with phase $\Delta\varphi = \gamma_2 - 2\gamma_1$. γ_2 is only acquired when the pulses overlap ($\sin \theta \cos \theta \neq 0$), while γ_1 is acquired primarily between the two pulse sequences ($\sin \theta \neq 0$), and $\Delta\varphi$ can, e.g., be controlled by adjusting ΔT . This is seen in Fig. 5.9 where the entangling phase, $\Delta\varphi$ is shown as a function of the delay between the two pulse sequences when the relative phase is $\phi_r(t) = t \cdot 2$ MHz. To achieve $\Delta\varphi = \pi$ in this case it is sufficient to set $\Delta T \approx 2.1 \mu\text{s}$ corresponding to a gate time below $10 \mu\text{s}$.

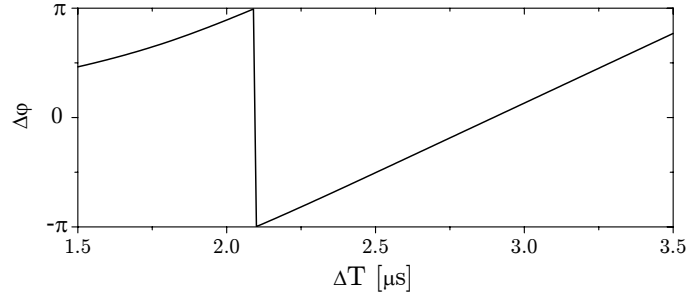


Figure 5.9: Entangling phase as a function of the delay between the two pulse sequences. The laser pulses are modeled by \sin^2 -pulses and parameters $A_{\max,1}/2\pi = A_{\max,r}/2\pi = 10$ MHz, $\Delta t = 1.1$ μs , $\tau = 1.5$ μs , $\phi_r(t) = t \cdot 2$ MHz, $\tau_r = 100$ μs and $E/\hbar = 100 \cdot 2\pi$ MHz

5.3 Many-particle entanglement

We now show that when more than two atoms in $|1\rangle$ are subject to the STIRAP pulse sequence they also become entangled. Provided all atoms are localised within a region of a few μm , the transition towards the Rydberg states is restricted to the coupling of collective states with either zero or one Rydberg atom and we implement this by truncating the basis so it only includes states with zero or one atom in the $|r\rangle$ state. We write the symmetric basis states of the system as

$$\begin{aligned} |n_1, n_2 = N - n_1, 0\rangle, \\ |n_1, n_2 = N - n_1 - 1, 1\rangle, \end{aligned} \quad (5.13)$$

where N is the total number of atoms, n_1 and n_2 the number of atoms in $|1\rangle$ and $|2\rangle$ and 0 or 1 indicates whether $|r\rangle$ is populated with zero or a single atom. The basis consists of $N + 1$ states with no Rydberg excitation and N with a single excitation. The interaction with the radiation fields Ω_1 and Ω_r , $\sum_{j=1}^N -\frac{1}{2}(\Omega_1(t)|2\rangle_j\langle 1| + \Omega_r(t)|r\rangle_j\langle 2| + \text{h.c.})$, can now be rewritten

$$H(t) = H_{J_x}(t) + H_{J_C}(t), \quad (5.14)$$

with variable strengths, representing the coupling by the fields driving the lower and the upper transition, respectively. The dynamics of the lower levels can be rewritten in a collective spin description and in the accompanying Schwinger oscillator description,

$$H_{J_x}(t) = -\hbar\Omega_1(t)J_x(t) = -\frac{1}{2}\hbar\Omega_1(t)(a_1^\dagger a_2 + a_1 a_2^\dagger), \quad (5.15)$$

where $a_i^{(\dagger)}$ are annihilation (creation) operators for the number of atoms in $|i\rangle$. The upper transition is described by

$$H_{JC}(t) = -\frac{1}{2}\hbar\Omega_r(t)(a_2\sigma^+ + a_2^\dagger\sigma^-) \quad (5.16)$$

where we use Pauli matrices σ^+ and σ^- to describe the transfer of population between states with zero and one Rydberg excitation in the atomic ensemble. The Rydberg blockade is assumed in both the truncation of the basis and in the use of the two-level Pauli matrix description of the population in $|r\rangle$. The H_{JC} is the quantum optical Jaynes-Cummings (JC) Hamiltonian, introduced originally to describe the resonant interaction between a two-level atom and quantised light [72]. JC dynamics has been implemented in strong coupling cavity QED experiments, where non-classical states of light, such as Fock states and quantum superposition states, are produced efficiently [73]. H_{JC} also describes the motion of laser driven trapped ions, where it has been used to generate various non-classical states [74, 75]. Following these proposals, JC dynamics is sufficient to produce a variety of interesting states of an atomic ensemble by the Rydberg blockade. In this work we will use the advantages of the robust STIRAP process to produce entangled states.

The Hamiltonian in (5.14) has a dark state with zero valued eigenenergy throughout the STIRAP process. This follows because the operator $\Theta = (-1)^{\hat{n}_2}$, which inverts the sign of the operators a_2 and a_2^\dagger , anti-commutes with H , $H\Theta = -\Theta H$. Any eigenstate $|\psi\rangle$ of H with energy eigenvalue \mathcal{E} , then has a partner, $\Theta|\psi\rangle$ with eigenvalue $-\mathcal{E}$ and the energy eigenvalue spectrum is symmetric around zero. The number of eigenstates is odd because N atoms induce $N+1$ different states with no atoms in $|r\rangle$ and N states with one atom in $|r\rangle$, and hence there must always be a state with eigenvalue zero. The full curves in Fig. 5.10 show the 13 energy eigenvalues for 6 atoms found from a numerical diagonalisation of (5.14), and they clearly confirm the existence of the dark state throughout the pulse sequence.

The STIRAP process starts with $\Omega_1 = 0$ and hence initially $H(t) = H_{JC}(t) = -\frac{1}{2}\hbar\Omega_r(t)(a_2\sigma^+ + a_2^\dagger\sigma^-)$. The Jaynes-Cummings Hamiltonian has eigenvalues $\{0, \pm\frac{1}{2}\hbar\Omega_r(t)\sqrt{n_2+1}\}$ and these are shown as blue curves in Fig. 5.10, where they match the full solution as long as $\Omega_1 = 0$. In this regime the dark state is $|n_1 = N, n_2 = 0, n_r = 0\rangle$ corresponding to our initial state with all atoms in $|1\rangle$. Adiabaticity ensures that we remain in the dark state of the full Hamiltonian and when Ω_1 is increased and Ω_r reduced, the system ends up in the dark state of $H(t) = H_{J_x}(t) = -\hbar\Omega_1(t)J_x$. The final state with $J_x = 0$ have either no or a single Rydberg excitation leaving $K = N$ or $K = N - 1$ atoms in the $|1\rangle$ and $|2\rangle$ states. The eigenvalues of $-\Omega_1(t)J_x$ are $-\Omega_1(t)\{-K/2, -K/2+1, \dots, K/2-1, K/2\}$ and $\mathcal{E} = 0$ occurs for K even. For N even, the dark state does not populate $|r\rangle$, while for N odd, the final dark state is the state with one Rydberg excitation and $N - 1$ atoms in the $J_x = 0$

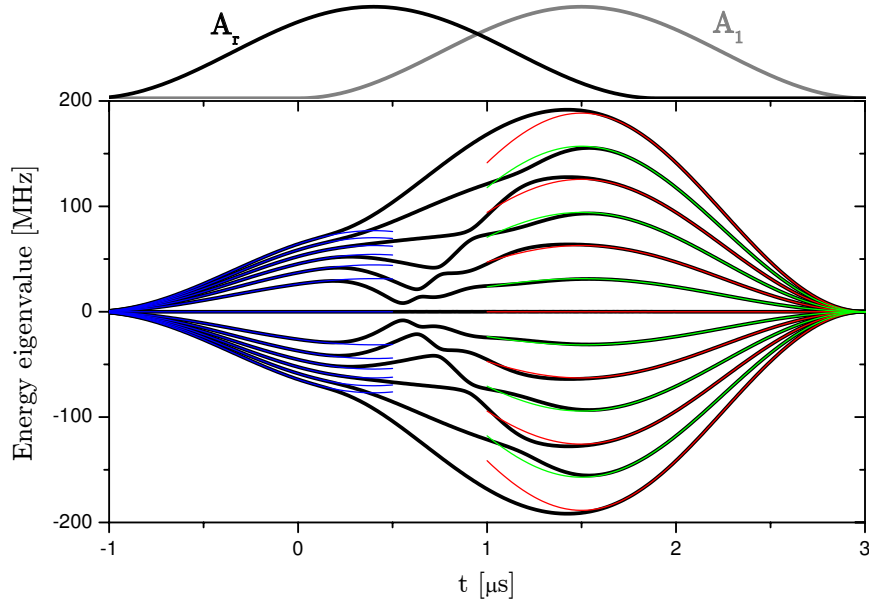


Figure 5.10: Eigenvalues of $H(t)/\hbar$ of (5.14) for $N = 6$. Black solid curves show the results of a numerical diagonalisation of the full Hamiltonian. The blue curves on the left show the analytical eigenvalues of $H_{JC}(t)/\hbar$ and the red and green curves on the right show the analytical eigenvalues of $H_{J_x}(t)/\hbar$ for zero and one Rydberg excitation, respectively. Parameters used are $A_{\max,1}/2\pi = A_{\max,r}/2\pi = 10$ MHz, $\Delta t = 1.1 \mu\text{s}$, $\tau = 1.5 \mu\text{s}$ and $\phi_r = 0$.

eigenstate. In general we write the final dark state

$$|D_N\rangle = \begin{cases} |J_x = 0\rangle & \text{if } N \text{ is even} \\ (|J_x = 0\rangle \otimes |r\rangle)_{sym} & \text{if } N \text{ is odd} \end{cases}, \quad (5.17)$$

where $(\cdot)_{sym}$ indicates that the state is symmetrised with respect to $|r\rangle$, such that any atom is Rydberg excited with equal weight. Figure 5.10 shows the eigenvalues of $-\Omega_1(t)J_x$ when $|r\rangle$ is not populated (red curves) and when one atom is excited to $|r\rangle$ (green curves) for $N = 6$. They overlap perfectly with the full solution when $\Omega_r = 0$.

The STIRAP protocol produces a $|J_x = 0\rangle$ multi-particle entangled state, and precisely this state reaches the Heisenberg limit of phase sensitivity in entanglement enabled precision metrology [76, 77]. If the two lower states are, e.g., the hyperfine states of the Cs clock transition, the presented entanglement scheme thus constitutes an ideal preparation of the system for an atomic clock. Note that $|J_x = 0\rangle$ is produced even when no knowledge of the exact atom number is available implying that a mixed initial state is transferred to a mixed final state with $J_x = 0$ exactly fulfilled. To avoid decay into the states $|1\rangle$ and $|2\rangle$, which would slightly perturb the $J_x = 0$ property, one may field ionise the Rydberg excited component after the STIRAP process.

5.3.1 Greenberger-Horne-Zeilinger states

The state (5.17) has none or a single Rydberg excited atom, depending on the number of atoms initially in the $|1\rangle$ state, n_1 , being even or odd. Following [78], this can be used to prepare a Greenberger-Horne-Zeilinger (GHZ) state [79] of the system. We first prepare all our atoms in a spin coherent state that is a product of superpositions of two ground states $|0\rangle$ and $|1\rangle$,

$$\left(\frac{|0\rangle + |1\rangle}{\sqrt{2}}\right)^{\otimes N} = \sum_{n_1=0}^N \sqrt{\binom{N}{n_1}} \left(\frac{1}{\sqrt{2}}\right)^N |n_0, n_1\rangle, \quad (5.18)$$

where n_1 is the number of atoms in $|1\rangle$ and $n_0 = N - n_1$. This can for instance be done by subjecting all atoms to a $\pi/2$ Raman pulse. Applying the pair of STIRAP processes in Fig. 5.8 to the entire system transfers each component $|n_0, n_1\rangle$ to a state with none or a single Rydberg excitation and back. An energy shift of the Rydberg state or a phase shift of the laser coupling the Rydberg state can now be used to provide components populating the Rydberg state with a phase, $e^{i\eta} = i = e^{i\pi/2}$, while states with no Rydberg excitation acquire the trivial phase, $e^{i\eta} = 1$. These phases can be expressed as a function of n_1 ,

$$e^{i\eta(n_1)} = \frac{e^{i\pi/4} + (-1)^{n_1} e^{-i\pi/4}}{\sqrt{2}}. \quad (5.19)$$

Each $|n_0, n_1\rangle$ component acquires $e^{i\eta(n_1)}$ leading after the second STIRAP process to the final GHZ state,

$$\begin{aligned} |\psi_f\rangle &= \sum_{n_1=0}^N \sqrt{\binom{N}{n_1}} \left(\frac{1}{\sqrt{2}}\right)^N e^{i\eta(n_1)} |n_0, n_1\rangle \\ &= \frac{e^{i\pi/4}}{\sqrt{2}} \left(\frac{|0\rangle + |1\rangle}{\sqrt{2}}\right)^{\otimes N} + \frac{e^{-i\pi/4}}{\sqrt{2}} \left(\frac{|0\rangle - |1\rangle}{\sqrt{2}}\right)^{\otimes N}. \end{aligned} \quad (5.20)$$

5.3.2 Maintaining adiabaticity

We have investigated the preparation of the $|J_x = 0\rangle$ (5.17) and GHZ (5.20) states using the \sin^2 -pulses and taking into account the coupling to states with two Rydberg excited atoms and the accompanying energy shift. For $N = 10$ we find a population of the $|J_x = 0\rangle$ or GHZ state above 0.995 for peak Rabi frequencies of $10 \cdot 2\pi$ MHz, a Rydberg interaction, $E/2\pi = 400$ MHz and pulse widths of $50 \mu\text{s}$. These numbers require the use of Rydberg levels with $n \geq 100$ where a lifetime above 1 ms can be achieved for atoms in a cryogenic environment (see Fig. 5.2). The black curve in Fig. 5.11 show the decrease in fidelity as N increases for the parameters mentioned above. Increasing N beyond 10 will require a stronger Rydberg interaction to prevent multiple Rydberg excitations as well as longer pulses and higher Rabi frequencies to

ensure adiabaticity. This is shown with the grey curve in Fig. 5.11 where the peak Rabi frequencies, the pulse widths and Rydberg interaction strength are doubled and the fidelity is increased from 0.43 to 0.98 for $N = 20$. Full insight into the parameter requirements for large N will necessitate further numerical studies. As indicated by the energy spectra in Fig. 5.10, there is a critical crossing region at $t \simeq 0.5 \mu\text{s}$, where special care should be taken, and we anticipate that control theory may be used to find optimal pulse shapes that may improve the fidelities and make it possible to reach higher atom number.

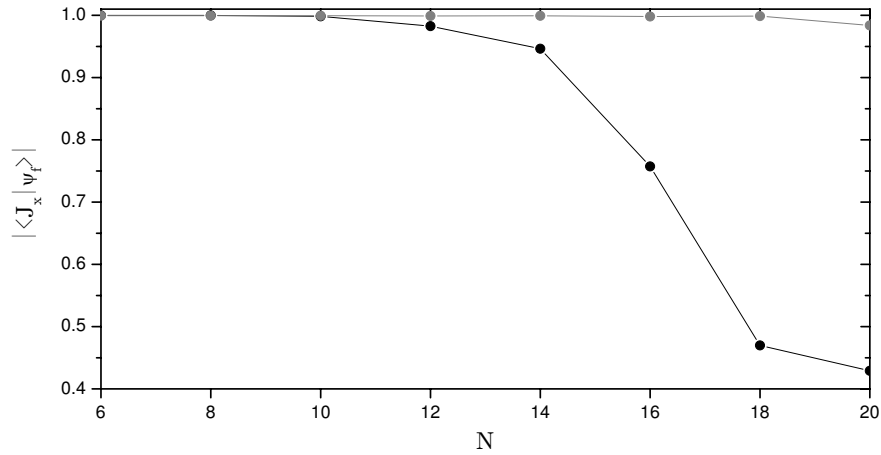


Figure 5.11: Fidelity of the $|J_x = 0\rangle$ creation as a function of the number of atoms for two different sets of parameters. The laser pulses are modelled by the \sin^2 -pulses in (2.23) and the black curve is the result for parameters $A_{\max,1}/2\pi = A_{\max,r}/2\pi = 10$ MHz, $\Delta t = 30 \mu\text{s}$, $\tau = 50 \mu\text{s}$ and $E/2\pi = 400$ MHz, while the grey corresponds to $A_{\max,1}/2\pi = A_{\max,r}/2\pi = 20$ MHz, $\Delta t = 70 \mu\text{s}$, $\tau = 100 \mu\text{s}$ and $E/2\pi = 800$ MHz.

5.4 Conclusion

In conclusion, we have demonstrated that the Rydberg excitation blockade mechanism in conjunction with rapid adiabatic passages provide rich opportunities to prepare two- and multi-atom entangled states with confined samples of atoms in for example optical dipole traps or small lattice arrays. Our calculations indicate the possibility of high fidelity generation of entangled states and quantum superposition states with tens of atoms. To achieve implementations in larger systems, higher Rabi frequencies and Rydberg states with longer coherence times must be available for experimentalist. In addition control theory may be used to optimise pulse shapes.

Chapter 6

Quantum computation with $^{40}\text{Ca}^+$

Trapped laser cooled ions are one of the most promising candidates for implementing quantum computation. They represent well isolated systems with long coherence times and by applying available laser sources population of the internal states can be controlled to high precision. In the first part of this chapter we briefly discuss the progress in implementing the ion trap quantum computer going through the DiVincenzo criteria presented in chapter 1.1.3. We focus on the ion specie ($^{40}\text{Ca}^+$) and the qubit encoding (Zeeman sub-levels) considered experimentally here in Århus, but also point out the key results of whole ion trap community. In the second part, we propose a scheme for internal state detection that we will use to detect our qubit. This detection scheme is also the subject of the experimental investigations in chapter 7 and 8.

6.1 Requirements

6.1.1 A scalable qubit system

We intend to use the two Zeeman-sublevels of the $|S_{1/2}\rangle$ ground state of $^{40}\text{Ca}^+$ as our qubit states and denote them by $|\uparrow\rangle(m = 1/2)$ and $|\downarrow\rangle(m = -1/2)$. The five relevant energy states $|S_{1/2}\rangle$, $|P_{1/2}\rangle$, $|D_{3/2}\rangle$, $|P_{3/2}\rangle$ and $|D_{5/2}\rangle$ are shown in Fig. 6.1 and we indicate their Zeeman structure. We will couple the states by four laser fields with wavelengths 397 nm, 866 nm, 850 nm and 854 nm. The $|D_{3/2}\rangle$ and $|D_{5/2}\rangle$ states are metastable with lifetimes ≈ 1 s [80] and their decay can thus be neglected. The $|P_{1/2}\rangle$ and $|P_{3/2}\rangle$ states decay as indicated in Fig. 6.1(b). The physical properties of the $^{40}\text{Ca}^+$ ion is described in appendix B.

Other advanced qubit encodings are based on either a combination of the $|S_{1/2}\rangle$ and the $|D_{5/2}\rangle$ states in $^{40}\text{Ca}^+$ [81] or encodings in hyperfine states of

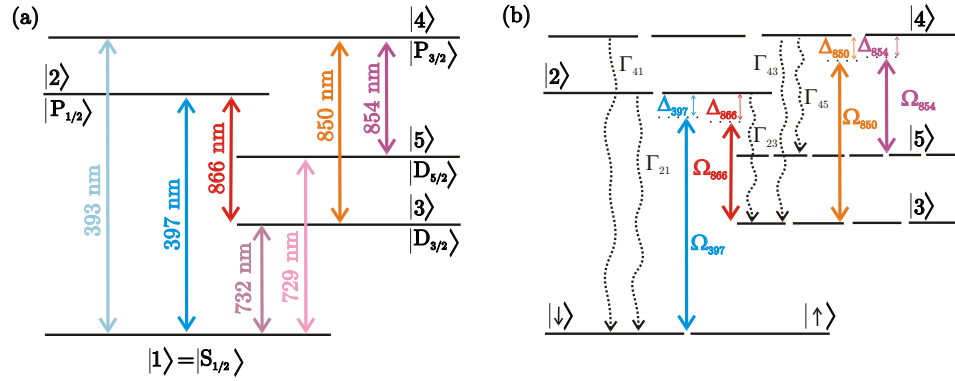


Figure 6.1: Relevant energy levels of $^{40}\text{Ca}^+$. In (a) we indicate their terms (LJ), $|1\rangle = |S_{1/2}\rangle$, $|2\rangle = |P_{1/2}\rangle$, $|3\rangle = |D_{3/2}\rangle$, $|4\rangle = |P_{3/2}\rangle$ and $|5\rangle = |D_{5/2}\rangle$ and show the wavelengths of the transitions. In (b) only the four couplings used in this work is shown with Rabi frequencies Ω_i and detunings Δ_i . Here, we also indicate the Zeeman sublevels and the qubit encoding in the electronic ground state, ($|\uparrow\rangle(m = 1/2)$ and $|\downarrow\rangle(m = -1/2)$). The non-negligible decay rates from $|i\rangle$ to $|j\rangle$ (Γ_{ij}) are shown as well.

$^9\text{Be}^+$ or $^{111}\text{Cd}^+$ [82, 83]. The advantage of the implementations in Ca is that laser sources of the right wavelengths are readily available, while the hyperfine qubits of $^9\text{Be}^+$ or $^{111}\text{Cd}^+$ are less sensitive to magnetic field fluctuations. The experimental advances are similar for the two approaches and research is also devoted to combining the strengths of the two using the isotope $^{43}\text{Ca}^+$, which have non-zero nuclear spin and encode the qubit in the hyperfine sublevels of the $|S_{1/2}\rangle$ ground state [84, 85].

For all the ion trap proposals scaling the system is a challenging task. Scaling by just adding more ions to a string has a natural limit [86] and experiments entangling 6-8 ions [87, 88] are reaching this limit. Further scaling must rely on more clever designs. One promising design for a large-scale ion trap quantum computer [89] consists of several connected ion traps with the ability to transfer ions from one trap area to another. One area is used for interaction between ions using laser manipulation while other areas are used as memory units, where the ions are stored when they are not involved in gate operations in the interaction area. This requires control of the transport of ions in complex structures [90] and especially shuttling around corners is challenging [91].

6.1.2 Initialisation

The ion can be initialised in either the $|\downarrow\rangle$ or $|\uparrow\rangle$ state by optical pumping and the vibrational ground state of the quantised ion motion, $|0\rangle$ can be reached, e.g. by applying sideband cooling as discussed in chapter 7.2.

6.1.3 Universal gates

Performing a one-qubit gate corresponds to an arbitrary rotation on the Bloch sphere (Fig. 1.1), which for ions can be done by applying a laser pulse and controlling the phase of the light field and the pulse area. This requires individual addressing of the ions which has been demonstrated experimentally [92]. In our system Raman transitions between the two Zeeman sublevels of $|S_{1/2}\rangle$ via the $|P_{1/2}\rangle$ -state will be used for these quantum logic operations as demonstrated for the hyperfine qubits [82]. It will then be the pulse area of the effective Raman Rabi frequency we need to control. Alternatively, the geometric gates presented in chapter 3 could be implemented.

There are many different proposals for the implementation of a universal two-qubit gate. The first proposal was given by Cirac and Zoller when they suggested the ion trap quantum computer [11]. The gate is realised by coupling the qubits through their common vibrational motion and requires cooling to the vibrational ground state. Mølmer and Sørensen [93] made another proposal using the same coupling. The advantage of their gate is that it works for ions, which are not cooled to the exact vibrational ground state. Additionally, different implementations of geometric two-qubit phase gates was proposed [29,30]. The Cirac-Zoller gate [11], the Mølmer-Sørensen gate [93] and a geometric phase gate [30] have all been demonstrated experimentally [94–96]. The highest fidelity with hyperfine qubits was demonstrated implementing the phase gate in $^9\text{Be}^+$ -ions yielding a fidelity of approximately 97% [96]. Recently, this result was exceeded with the optical qubit in $^{40}\text{Ca}^+$ implementing the Mølmer-Sørensen gate with a 99.3% fidelity [97]. This fidelity approaches the error thresholds required for fault tolerant quantum computation¹. Small algorithms using trapped ions have been implemented experimentally; Grover's search algorithm [100], the Deutsch-Jozsa algorithm [101] and the semiclassical quantum fourier transform [102], which is an important ingredient in Shor's factoring algorithm.

6.1.4 Coherence time

In the experimental realisation of the Cirac and Zoller gate [11] the operation time was $\approx 500 \mu\text{s}$, while the the Mølmer-Sørensen gate and the controlled phase gate is as fast as $\approx 20 \mu\text{s}$ [94, 96]. This sets the requirements for the coherence time of our qubit. Coherence times of tens of seconds of two Zeeman substates of $^{40}\text{Ca}^+$ encoded in a decoherence free subspace [103] has been observed [104]. Using the field insensitive hyperfine qubits [105] a similar coherence time is reached without going into a decoherence free subspace and an order of magnitude longer is expected for a decoherence free subspace of hy-

¹Different error correction codes estimate allowed error rates between 10^{-5} and 10^{-2} [98, 99]. However, high error rates require a large overhead of qubits to encode the error correction.

perfine qubits [103]. The coherence time of the ion trap quantum computer is therefore at present three orders of magnitude longer than the gate operation time. Since we are using the Zeeman-sublevels as our qubit the decoherence will mainly be due to external magnetic fields and to achieve a sufficient coherence time we will need a good control of magnetic fields combined with encoding in a decoherence free subspace.

6.2 Internal state detection

We determine whether the ion is in the $|\uparrow\rangle$ or $|\downarrow\rangle$ -state by performing a projection measurement in three steps as shown in Fig. 6.2.

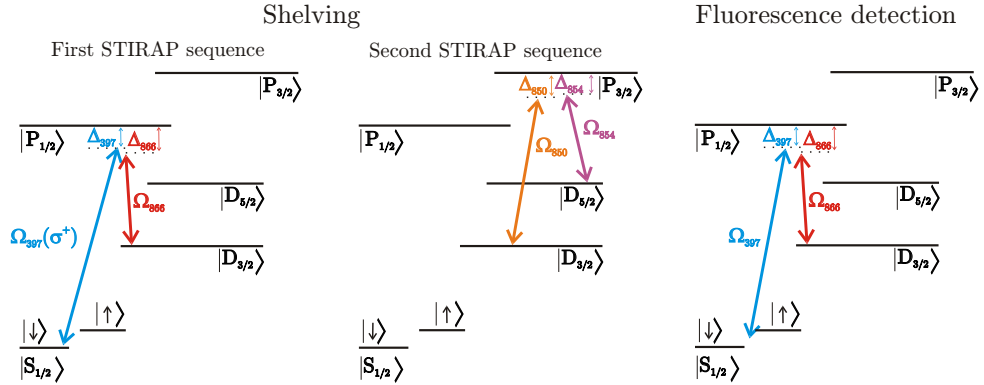


Figure 6.2: Laser fields applied in the three steps of the qubit detection scheme, first STIRAP process, second STIRAP process and fluorescence detection.

1. The first STIRAP process applies Ω_{397} and Ω_{866} transferring population from $|S_{1/2}\rangle$ to $|D_{3/2}\rangle$. The polarisation of the 397 nm pulse is chosen so that only the population in $|\downarrow\rangle$ is transferred, while $|\uparrow\rangle$ remains unaffected.
2. The second STIRAP process with Ω_{850} and Ω_{854} applied transfers all population in $|D_{3/2}\rangle$ to $|D_{5/2}\rangle$.
3. After shelving, the population remaining in $|\uparrow\rangle$ can be observed applying Ω_{397} and Ω_{866} and monitoring the fluorescence at 397 nm.

A weak externally applied magnetic field defines the quantisation axis and creates a Zeeman splitting of $|\downarrow\rangle$ and $|\uparrow\rangle$. Another detection scheme was presented in [106] with a 86% efficiency and relies on angular momentum selection rules combined with coherent population trapping. The STIRAP process used is described in chapter 2.2 and we use the Gaussian pulses defined in (2.22).

6.3 Summary

The ion trap quantum computer is no longer a theoretical idea since all DiVincenzo criteria except scalability are met. Scaling the computer requires new trap designs with, e.g., segmented traps as well as a reduction of all error rates. This means that all gates as well as the state detections have to be performed with very high fidelities and requires long coherence time. In the following two chapters we will focus on the experimental implementation of the internal state detection, as outlined above.

Chapter 7

Experimental setup

In this chapter we introduce the experimental equipment and setup used in the STIRAP experiments.

7.1 Overview

The experimental setup consists of a segmented linear Paul trap placed in the centre of a vacuum chamber accessible by laser beams from several directions. A sketch of the setup is shown in Fig. 7.1 and a picture of the vacuum chamber and its components in Fig. 7.2. Ultra high vacuum is obtained by baking out

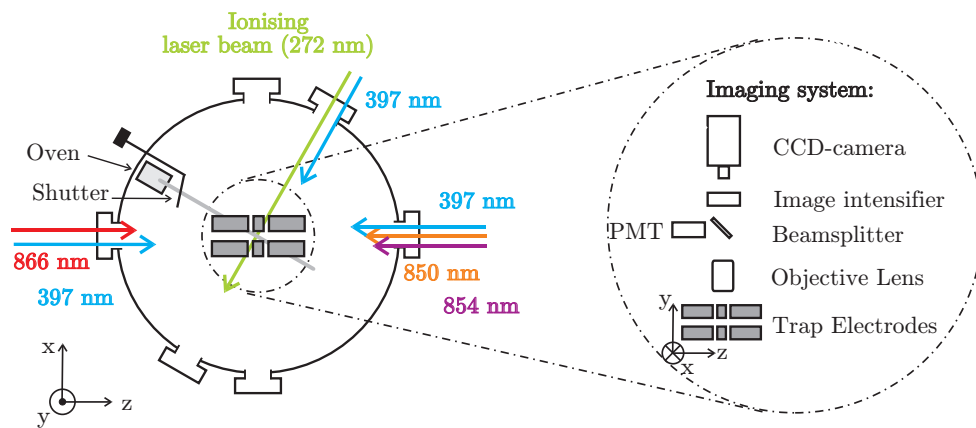


Figure 7.1: Sketch of the experimental setup including the imaging system. The applied laser fields are indicated.

the chamber at 150 °C during a few days while applying a turbo molecular pump¹. After bakeout a pressure around $4 \cdot 10^{-11}$ Torr is maintained by an

¹Leybold Trivac

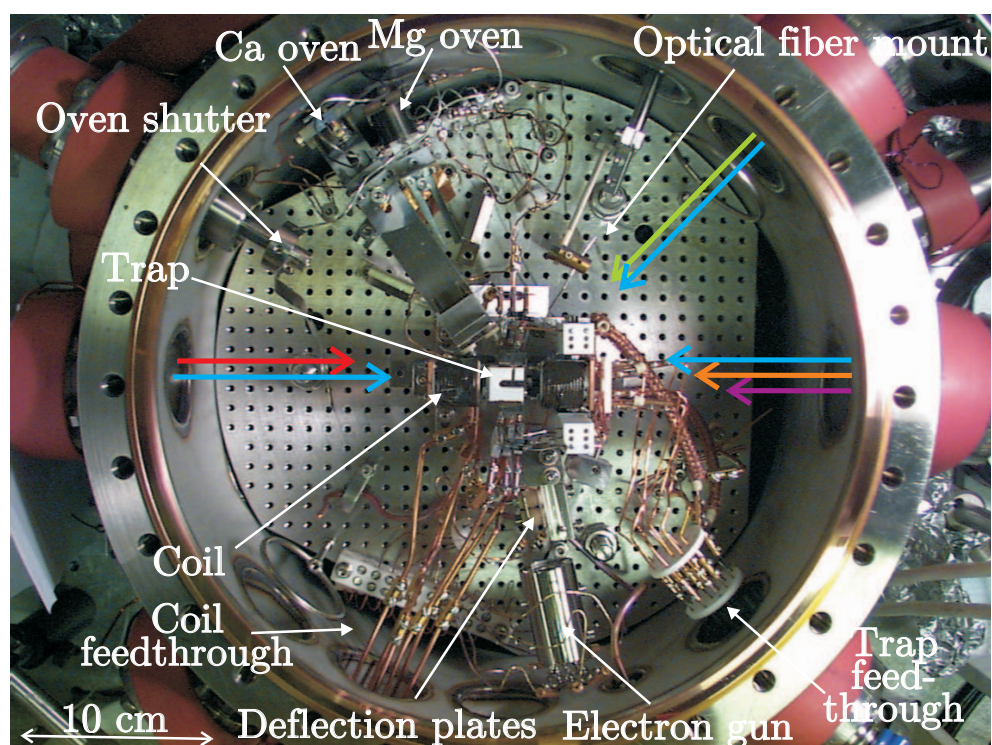


Figure 7.2: Picture of the vacuum chamber and its constituents. The applied laser fields are indicated.

ion pump² and a sublimation pump³. A beam of calcium atoms is released from an oven (heated to ≈ 500 °C) and ionised by a 272 nm uv-laser beam as described in chapter 7.3. The beam of calcium atoms intersects the ionising laser beam in the centre of the linear Paul trap. Alternatively, the calcium can be ionised using an Electron gun which can be steered through the trap centre using deflection plates. This method has not been used in this work since it is not isotope selective and more dirty than photoionisation. RF- and DC-voltages are applied to the trap electrodes, confining the ions in the centre of the trap.

In addition to the ionisation beam the ions are addressed by four laser beams (with wavelengths 397 nm, 866 nm, 850 nm and 854 nm) passing through viewports of the vacuum chamber as shown in Fig. 7.1 and 7.2. All laser fields intersect at the trap centre. As a guidance an optical fibre (125 μm diameter) mounted inside the chamber can be placed in the trap centre and detection of scattered light using the imaging system will ensure that the lasers pass through the centre. Above the trap an imaging system collects the 397 nm photons and we detect the fluorescence with a CCD camera and a photo mul-

²Varian VacIon Plus 300 Starcell pump (240L/s) with a Midivac 929-5002 controller

³Constructed at the Department

tiplier tube (PMT). Before entering the chamber the laser beams pass several lenses, waveplates, EOMs and AOMs, that control their waist, polarisation, frequency and shape.

Two coils are placed in a Helmholtz configuration on each side of the trap and used for creating a magnetic field along the trap axis. The vacuum chamber and all parts mounted inside it have been described in detail in [29]. In the following the laser systems (chapter 7.4), the imaging system (chapter 7.5), the ion trap (chapter 7.6), and external magnetic fields (chapter 7.7) will be described in further detail. The laser systems are used for STIRAP, Doppler cooling and photoionisation. STIRAP was discussed in detail in chapter 2.2 and we will, before giving the details on the setup of the laser systems, describe Doppler cooling (chapter 7.2) and photoionisation (chapter 7.3) of $^{40}\text{Ca}^+$.

7.2 Laser cooling of $^{40}\text{Ca}^+$

Laser cooling is a method used to reduce the velocity of for example a trapped ion. In Doppler laser cooling the ion interacts with a near resonant laser of frequency, ω_L . An ion with a velocity v with respect to the laser light experiences a shifted frequency: $\omega(v) = \omega_L(1 - \frac{v}{c})$. Ions moving towards the laser field will therefore experience a higher frequency, while ions moving away from the light experiences a lower.

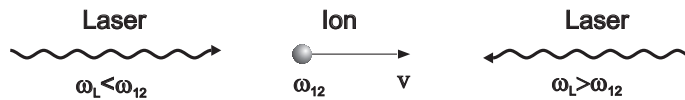


Figure 7.3: The Doppler cooling principle.

Doppler cooling takes place in what is effectively a two-level system (with resonance frequency, ω_{12}), where the laser field ω_L is red-detuned from the atomic resonance frequency, so ions moving towards the laser field with a velocity that match the Doppler shift ($kv = \Delta_{12} = \omega_{12} - \omega_L$) is exactly on resonance and have the largest possible absorption cross section. Absorption of a photon gives the ion an additional momentum $\hbar k$ in the direction of light propagation and subsequent decay gives another momentum kick. If the emission is stimulated it will effectively cancel the absorption. Spontaneous emission gives on average no contribution to the ion momentum, because the radiation pattern is spatially symmetric. This leaves an effective momentum kick in the direction of light propagation from absorption, which slows down the ion. The frequency of the absorbed photon is slightly lower than the frequency of the emitted and therefore energy is taken out of the system. Doppler cooling is described in further mathematical detail in [107].

In $^{40}\text{Ca}^+$, Doppler cooling is performed with a 397 nm laser on the $|S_{1/2}\rangle$ - $|P_{1/2}\rangle$ transition, and since some of the population in $|P_{1/2}\rangle$ decays to $|D_{3/2}\rangle$

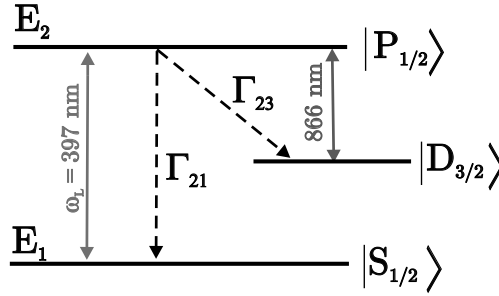


Figure 7.4: Doppler cooling using a two-level system with resonance frequency ω_{12} coupled with a laser at frequency ω_L . An additional laser at 866 nm is necessary in $^{40}\text{Ca}^+$ to repump from the $|D_{3/2}\rangle$ -state.

an additional laser at 866 nm is applied to repump the population in $|D_{3/2}\rangle$ into the cooling-cycle again (see Fig. 7.4). Laser cooling of free ions in three dimensions can be achieved using six pairwise counter-propagating laser beams⁴. For trapped ions this is not necessary because the velocity reverses in a confined system and one laser beam is sufficient if applied in a direction that cools both radial and axial motion. In the experiment we use two counter-propagating beams parallel to the ion string and one beam in a 45° angle with respect to the string as shown in Fig. 7.1. The continuous process where an ion absorbs and emits a photon sets a lower boundary for the velocity of the ion. With optimal detuning an average kinetic energy, $\langle E_k \rangle = \frac{\hbar\Gamma}{4}$ can be obtained, where for simplicity only one dimension was considered [108]. From the kinetic energy a temperature can be defined from $\frac{1}{2}k_B T = \langle E_k \rangle$, which for optimal Doppler cooling gives the so-called Doppler temperature,

$$T_D = \frac{\hbar\Gamma}{2k_B}. \quad (7.1)$$

For the $|S_{1/2}\rangle$ - $|P_{1/2}\rangle$ cooling transition $\Gamma_{21}/2\pi = 20.7$ MHz. This corresponds to a Doppler temperature $T_D = 0.5$ mK, when we neglect the $|P_{1/2}\rangle$ - $|D_{3/2}\rangle$ transition. This approximation is allowed because only 8% of the population in $|P_{1/2}\rangle$ decay through this channel. Doppler cooling gives the additional advantage that emitted 397 nm photons allow for detection of the ions using a CCD-camera or a photo-multiplier tube (PMT).

Recently, Doppler cooling on the dipole forbidden $|S_{1/2}\rangle$ - $|D_{5/2}\rangle$ transition was demonstrated [109]. The 854 nm and 866 nm lasers were applied to repump population from $|D_{3/2}\rangle$ and $|D_{5/2}\rangle$ to $|P_{3/2}\rangle$ and $|P_{1/2}\rangle$, from where it decays back to $|S_{1/2}\rangle$ and emits the 393 nm and 397 nm photons used for detection. This has the advantage that photons are detected on a transition, where no lasers are applied and therefore improves the signal to noise ratio.

⁴Actually only 4 laser beams are required when applied in a clever configuration.

Additionally, it allows for quantum logic experiments in $^{40}\text{Ca}^+$ using only infrared laser sources.

The ion is confined in the linear Paul trap and it experiences as we will discuss in chapter 7.6 a harmonic potential. The quantised ion motion is therefore described by the vibrational eigenstates $|n\rangle$ of the harmonic oscillator, where n is the vibrational quantum number corresponding to the energy $(\frac{1}{2} + n)\hbar\omega_z$, where $\omega_z/2\pi \approx 0.5$ MHz is the axial oscillation frequency of the ion in the trap. With more than one ion in the trap different vibrational modes can be excited [110]. Ions cooled to the Doppler temperature $T_D = 0.5$ mK have a mean vibrational quantum number, $\langle n \rangle = 20$, found from the relation $k_B T_D = (\frac{1}{2} + n)\hbar\omega_z$. Confining the ion stronger by an increment of ω_z will decrease $\langle n \rangle$, but to reach the vibrational ground state, $|0\rangle$, Doppler cooling is not sufficient.

One efficient method is sideband cooling [35, 111] relying on the resolved sidebands appearing in the absorption profile of an internal transition, when its linewidth is much smaller than the trap oscillation frequency, $\Gamma \ll \omega_z$. In this regime the sidebands can by application of clever laser combinations be used to cool the ion to the vibrational ground state. Using dipole transitions for sideband cooling is not feasible because Γ is on the order of MHz and will therefore require extremely strong confinement of the ions. Instead dipole-forbidden quadrupole transitions [112–114] or two-photon Raman transitions [115, 116] have been used in experimental implementations. In our experiments we intend to use Raman transitions between the two Zeeman sublevel of $|S_{1/2}\rangle$ for sideband cooling of the trapped ions. This scheme was implemented in [116] and thoroughly described for our experiments in [29]. An alternative to sideband cooling relies on electromagnetically induced transparency [117] and cools the ion to nearly the vibrational ground state, $\langle n \rangle = 0.1$ [118, 119]. For large scale quantum computation and to avoid decoherence, sympathetic cooling can be applied [120, 121]. The ion used for quantum logic is now not laser cooled, but cooled via its Coulomb interaction with another ion, which is laser cooled. The other ion can be either a different ion specie [122] or a different ion isotope [123].

7.3 Photoionisation

Ionising the calcium loaded into the trap can be done using either electron bombardment or a two-photon ionisation process. As mentioned, only the latter was used in this work, because it is a very clean process that makes it possible to load ions in small ion traps, as the one used for our experiments, without depositing calcium on the electrodes. It furthermore has the advantage that the ionisation and thus the loading is isotope selective. This resonance-enhanced two-photon ionisation was presented in [124] and is shown schematically in Fig. 7.5. One 272 nm photon excites an electron from the

$4s^2\ ^1S_0$ -state to the $4s5p\ ^1P_1$ -state. Subsequently, the atom can be ionised by either a 272 nm or 397 nm (applied for doppler cooling) photon transferring the excited electron to the continuum. If the electron decays to the metastable $4s3d\ ^1D_2$ -state a 272 nm photon can still ionise the atom. Another two-photon

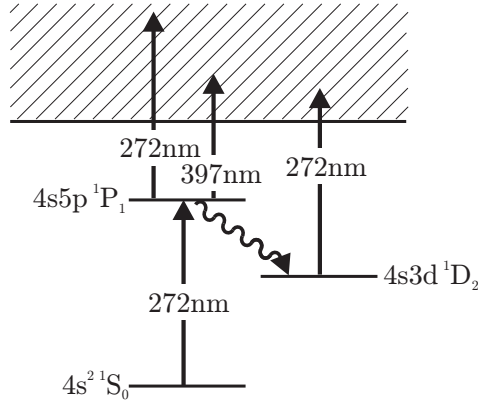


Figure 7.5: Simplified energy levels of neutral calcium. The hatched area indicates the continuum.

ionisation scheme was presented in [125] exciting to the $4s4p\ ^1P_1$ -state with a 423 nm and subsequently exciting an auto-ionising state with a 389 nm photon. This process has the advantage of a higher loading rate because of a high oscillation strength of the first excitation, but has the disadvantage of less isotope selectivity.

7.4 Laser systems

The STIRAP experiments require five laser systems. The calcium atoms are ionised in a process where two 272 nm photons are absorbed. For Doppler cooling and the first STIRAP sequence we use two lasers at 866 nm and 397 nm while the second STIRAP process is done by two lasers with wavelengths 850 nm and 854 nm. Figure 7.6 sketches the configuration of the beams on the trap table. For all lasers the wavelengths can be measured with a wavemeter⁵ with a seven-digit precision and the resonance frequencies can be found using optogalvanic spectroscopy with a hollow-cathode discharge lamp [127]. After measuring the power and waists of the lasers the Rabi frequency of each transition can be calculated from the formulas derived in Appendix B. We do not consider the phase of the Rabi frequencies and simply denote their strength by $\Omega(t)$.

⁵Standard tool for measuring laser wavelengths based on the interferometer design demonstrated first in [126].

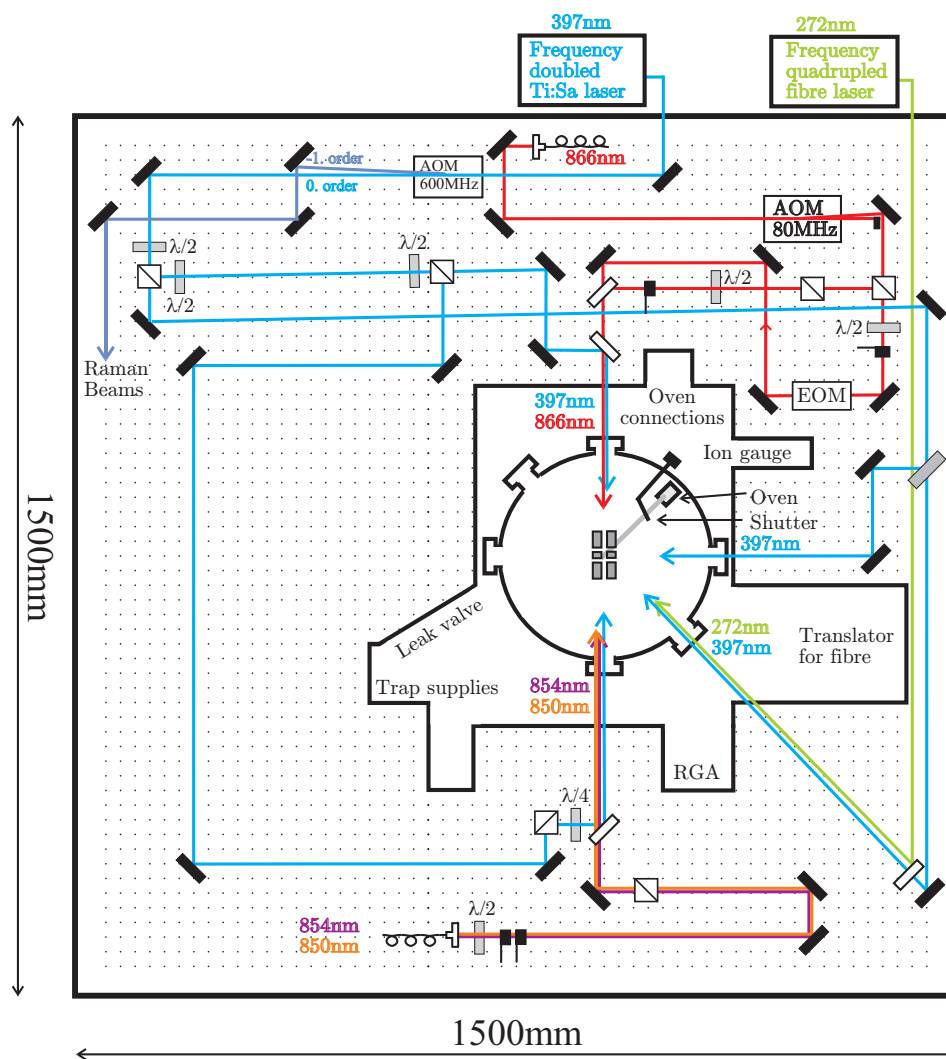


Figure 7.6: Sketch of beam configuration on the trap table. Only beams used in the experiments presented in this work are drawn.

7.4.1 397 nm lasersystem

In Fig. 7.7 a sketch of the 397 nm laser setup is seen. It consists of a Coherent 899 Titanium-Sapphire Ringlaser pumped by a Coherent Verdi V8 laser and frequency-doubled in a 12 mm LBO crystal placed in an external bowtie cavity. The Verdi laser has a maximal 8 W output power at 532 nm and usually pumps the Titanium-Sapphire laser with 6 W, which then produces approximately 400 mW at 794 nm. The 400 mW 794 nm light is then frequency doubled in the cavity creating ≈ 30 mW 397 nm light⁶. The cavity-length is locked using a Hänsch-Couillaud polarisation lock [129]. Frequency stabilisation is obtained by splitting of a small part of the Titanium-Sapphire laser to a temperature stabilised cavity and locking using the Pound-Drever-Hall technique [130,131]. The stabilisation cavity has a drift of ≈ 1 MHz/h [131]. The laser frequency can be scanned using an 220 MHz AOM in a double pass configuration placed in the beam used for frequency-locking. The 397 nm light is brought to the trap-table through air with negligible losses. In this work the 397 nm laser has only been used for Doppler cooling and for this purpose we split the beam in three parts. Two beams access the trap counter-propagating along the trap axis and one beam in a 45° angle with respect to the trap axis as sketched in Fig. 7.6. In future experiments a 600 MHz AOM will split the beam and the light on resonance (0. order) will be used for Doppler cooling, while the light shifted 600 MHz (1. order) will be used for the first STIRAP sequence as well as Raman beams for sideband cooling and gates.

7.4.2 Infrared lasersystems

The three diode lasers (850 nm, 854 nm and 866 nm) are anti-reflection coated diodes in homebuilt external cavities with gratings (1800 lines/mm) in Littrow configurations. Frequency locking and control are obtained as in the case of the 397 nm laser described above.

The 866 nm laser (Fig. 7.7) is sent through an optical fibre to the trap table. At the trap table (Fig. 7.6) the beam is split into two. One part is used to repump population that decays to the $D_{3/2}$ -state during Doppler cooling back into the $S_{1/2} \leftrightarrow P_{1/2}$ -cooling cycle. In order to avoid Zeeman sublevels in $D_{3/2}$ that do not couple to the 866 nm laser this part of the beam passes through an Electro Optical Modulator (EOM) used to scramble the polarisation. The other beam is used for optical pumping so we can force population into desired Zeeman sublevels of $D_{3/2}$. The two beams can be blocked independently by mechanical shutters.

The 850 nm and 854 nm lasers are pulsed using two 70 MHz AOM's and subsequently overlapped on a grating and sent to the trap table through the same fibre ensuring perfect overlap. The 850 nm and 854 nm lasers are locked

⁶With a new crystal and an optimised cavity 500 mW 794 nm-light has been shown to generate 150 mW 397 nm-light [128].

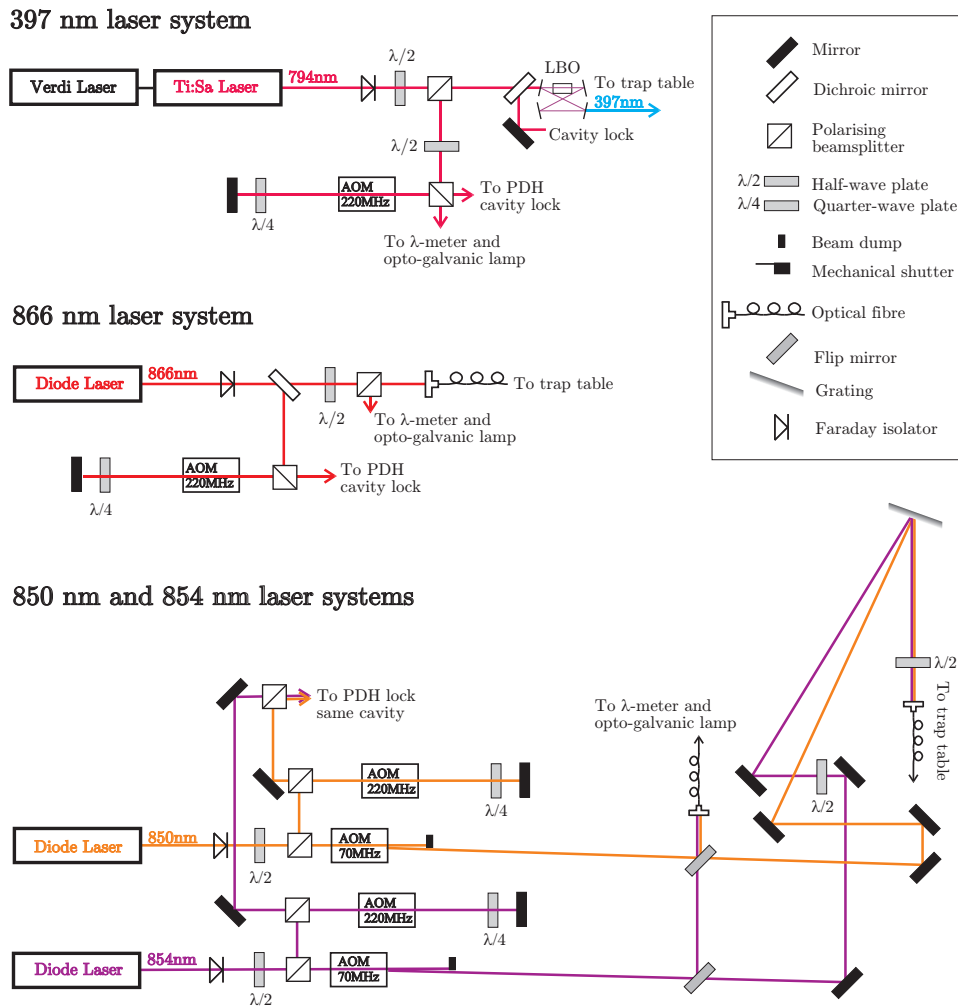


Figure 7.7: Sketch of the setup of the four laser systems used for Doppler cooling and STIRAP.

to the same reference cavity with a drift below 1 MHz/h, and when we use co-propagating beams the drift in two-photon detuning will be well below 1 MHz/h. The laser detunings will in the experiments be a whole free spectrum range of the reference cavity, which is approximately $2\pi \cdot 600$ MHz.

7.4.3 272 nm lasersystem

Until recently 544 nm light was produced by a Coherent CR-699 ring laser using the dye Pyrromethene and pumped by a Spectra Physics Argon Ion laser. The laser was frequency locked to a commercial stabilisation cavity. This system has been replaced by a frequency-doubled fibre laser system. The fibre laser is an ytterbium doped germanosilicate glass distributed feedback laser⁷ producing 1088 nm light coupled through a polarisation maintaining fibre. 544 nm light is then produced by second harmonic generation in a 15 mm LiNbO₃ crystal placed in an external bowtie cavity. To achieve non-critical phase matching the crystal is placed in a homebuilt oven where $T \approx 161$ °C is maintained. The cavity is frequency locked using the Pound-Drever-Hall technique. The fibre laser produces at most 2 W which is converted to 845 mW 544 nm light. Power levels above 700 mW are stable over several hours. The 544 nm light is frequency-doubled to achieve 272 nm light. This second harmonic generation takes place in another Bowtie cavity with a 8 mm BBO crystal locked with a Hänsch-Couillaud technique. 730 mW of 544 nm light gives rise to 115 mW at 272 nm. For further details on the setup and performance of the fibre laser system see [132].

7.4.4 Residual light

In the first generation of STIRAP experiments beams of atoms passed through two stationary laser beams [37, 40]. Here, the detection region was spatially well separated from the STIRAP region and no residual light was present. When we consider the situation with stationary ions and pulsed laser beams, the situation is less favourable. In the case of a constant background level of laser light, the ions do not start out in an exact dark state and hence population transfer may be limited by the resulting finite population of the short lived states $|P_{1/2}\rangle$ and $|P_{3/2}\rangle$. Moreover, since the residual light is able to excite the Raman resonance between the states $|D_{3/2}\rangle$ and $|D_{5/2}\rangle$, repumping of the transferred population can take place after the STIRAP pulse sequence. With a small background level of light this Raman resonance will be narrow and hence the limitation of population transfer is most severe near two-photon resonance and it may therefore be most efficient to perform STIRAP experiments slightly off two-photon resonance if residual light is present. One-photon excitations will not be severe because we use large one-photon detunings. In the experiments it is important to reduce the residual light and we do this in two

⁷Koheras BoostikTM

steps. The laser pulses are generated using AOM's as mentioned previously and to ensure a fast and efficient shut down of the RF-power delivered to the AOM's, an electronic RF-switch is build into the AOM RF-sources. With the switch the RF-power delivered to the AOM is suppressed with 100 dB. The RF-switch is fast, but it still allows for generation of a small amount of residual 1.order light. In addition, 0.order light scattered in the crystal also reach the ions, and we therefore shut the beams using two mechanical shutters (one for opening and one for shutting). These have an opening/closing time as well as a time jitter, such that they are open approximately 200 μs during which experiments take place in $\approx 10 \mu\text{s}$.

7.4.5 Laser phase fluctuations

Laser phase fluctuations lead to dephasing between the three states involved and may affect STIRAP. We have therefore measured the phase fluctuations of the involved lasers and explain the method and the results in appendix C. On small time scales (a few μs) the fluctuations were measured to be a few kHz increasing to a few hundred kHz on a 22 μs time scale. These measurements showed that the linewidth to a good approximation had a Lorentzian profile. The fluctuations can therefore be included as decay terms in the off-diagonal elements of the density matrix (see appendix A). Such simulations of the population in $|D_{5/2}\rangle$ after a STIRAP process from $|D_{3/2}\rangle$ when disturbed by phase fluctuations are shown in Fig. 7.8 (dashed and dotted curves).

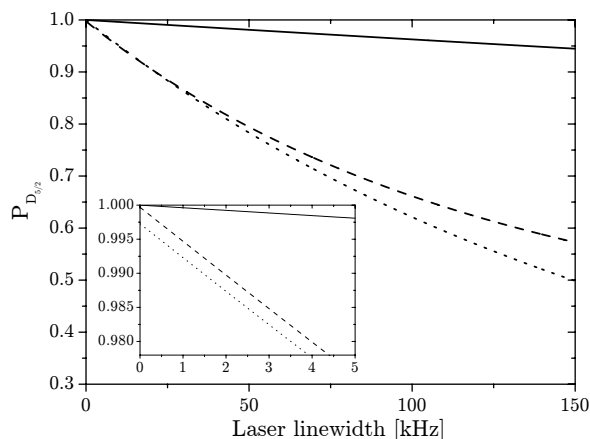


Figure 7.8: Transfer efficiency as a function of the linewidth of the 850 nm and 854 nm laser fields for different choices of Rabi frequencies. The simulations use Gaussian pulses (2.22) with $\tau_{850} = \tau_{854} = 2 \mu\text{s}$, $\Delta t = 1.2 \mu\text{s}$ and $\Delta_{850}/2\pi = \Delta_{850}/2\pi = 600 \text{ MHz}$ and Rabi frequencies $\Omega_{850,\text{max}}/2\pi = \Omega_{854,\text{max}}/2\pi = 300 \text{ MHz}$ (---) or $\Omega_{850,\text{max}}/2\pi = \Omega_{854,\text{max}}/2\pi = 100 \text{ MHz}$ (···). Initially, all population is in $|D_{3/2}\rangle$. The simulations are compared with $P_{D_{5/2}}$ from (7.2) (—).

The dephasing effect was also studied in [133], where the STIRAP transfer efficiency was shown to depend only on the dephasing rate between $|D_{3/2}\rangle$ and $|D_{5/2}\rangle$, γ_D ,

$$P_{D_{5/2}} = \frac{1}{3} + \frac{2}{3}e^{-3\gamma_D\tau^2/16\Delta t}, \quad (7.2)$$

for Gaussian pulses within the adiabatic limit, not taking decay from $|P_{3/2}\rangle$ into account. We show this approximate result as the solid curve in Fig. 7.8, but it underestimates the effect of laser phase fluctuations because decay is not included. The curves show that the transfer efficiency is strongly limited by the laser phase fluctuations. The duration of experiments must therefore be only a few microseconds to ensure phase fluctuations below $1.5 \cdot 2\pi$ kHz (see appendix C). In this case the transfer efficiency will remain above 0.99 of the population.

7.5 Imaging system

The imaging system is constructed to measure the rate of 397 nm photons emitted by the ions. A sketch of the imaging system is shown in Fig. 7.9. The objective lens⁸ is mounted on a 3D translation stage about 5 cm above the chamber. It collects and focuses the emitted light from the ions. The collected photons are split on a 50/50 beamsplitter. One part is amplified by an image intensifier⁹ and detected on a charged coupled device (CCD) camera¹⁰. The principle of the image intensifier is that photons hit a photocathode where they cause the emission of electrons. These electrons are accelerated by a DC voltage towards a phosphorscreen where the electron signal is converted back into light. Between the photocathode and the phosphor-screen the electrons pass microchannel plates that increases the number of electrons that reach the screen. The CCD-camera yields a position dependent picture of the emitted photons. The other part of the photons are detected by a photo multiplier tube (PMT)¹¹ measuring the total 397 nm fluorescence. With the camera we detect the fluorescence of the single ions individually while the PMT has the advantage that the signal can be analysed fast and efficient during experiments.

7.6 Ion storage

In the theoretical description so far the manipulations of single ions are simplified by considering ions that do not move and are not subject to external

⁸Nikon, 10x magnification and f-number ≈ 1.7 .

⁹Proxitronic, model BV 2581 BY-V 1N.

¹⁰Sensicam system from PCO.

¹¹Hamamatsu H5783P-06.

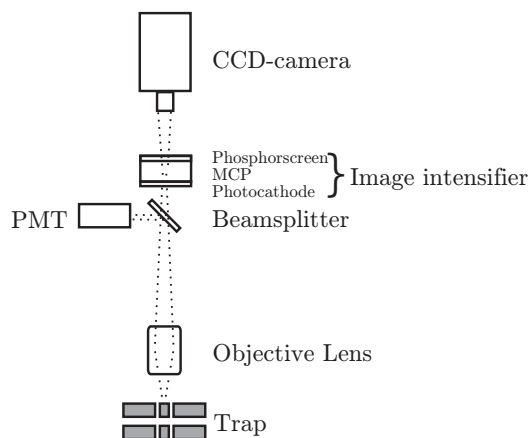


Figure 7.9: Sketch of imaging system.

forces beside the applied laser fields. Experimentally, we prefer a similar situation. This is obtained by confining the ions using electromagnetic fields and slowing them down using laser cooling. In all experiments presented here the ions are confined in the linear Paul trap [107, 134] and Doppler laser cooled as described previously in chapter 7.2. The Paul traps are based on the quadrupole mass filter [135] invented by Wolfgang Paul, and the linear version makes it possible to confine many ions strongly on strings and even create large crystals of ions [136–138]. For the linear Paul trap the three dimensional harmonic pseudo potential created by the trap and the very well isolated ions are important features for quantum logic. As shown in the following the ion motion is not strictly harmonic. The harmonic motion is superimposed by a small-amplitude motion, due to the RF-field used to trap the ions, called micromotion. This chapter describes the theory of ion storage in the linear Paul trap used for the experiments. For large scale quantum computation segmented traps [89], ion traps integrated on a chip [139] and surface traps [140] are being developed.

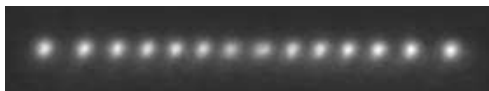


Figure 7.10: Fluorescence from ionstring confined in the linear Paul trap and Doppler laser cooled.

7.6.1 Trapping ions in the linear Paul trap

To confine charged particles in three dimensions, static electric fields are not sufficient as stated in Earnshaw's theorem [141]. In the linear Paul trap this is solved using a combination of static and Radio-Frequency (RF) electric fields to create an effective confining potential.

The ion trap used for the quantum logic project is sketched in Fig. 7.11 and consists of four plates. On the light blue plates an oscillating RF-field with frequency Ω_{RF} is applied. The other two plates consist of three electrodes each. To these electrodes static fields (U_a and U_{end}) are applied. U_a is applied to all electrodes, while U_{end} is only applied to the four end electrodes creating axial confinement. The alternating RF-field gives rise to a radial potential [29],

$$\varphi_{RF}(x, y, t) = (U_a - U_{RF} \cos(\Omega_{RF}t)) \frac{x^2 - y^2}{2Lr_0^2} + (U_a + U_{RF} \cos(\Omega_{RF}t)) \frac{1}{2L}, \quad (7.3)$$

where L is called "the loss factor" [142]. The static fields contribute to an

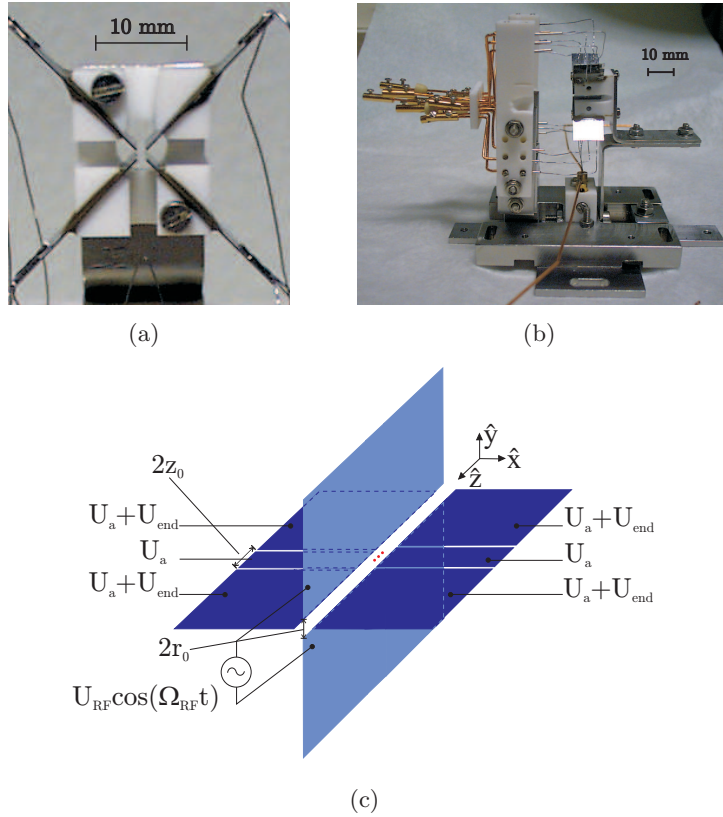


Figure 7.11: Linear Paul Trap used for quantum logic experiments. r_0 is the distance from the electrode surface to the trap center. $2z_0$ is the width of the central electrode pieces.

axial as well as a radial potential [29],

$$\varphi_{\text{end}}(x, y, z) = \kappa U_{\text{end}} \left(z^2 - \frac{1}{2}(1 - \chi)x^2 - \frac{1}{2}(1 + \chi)y^2 \right), \quad (7.4)$$

where the geometric factor $\kappa \approx (2z_0)^{-2}$. χ is an asymmetry parameter that accounts for U_{end} only being applied to the dark blue plates thus creating an asymmetry. For an ion of mass, m , and charge, Q , we can describe the motion in the resulting potential. On the z -axis the potential is static and harmonic at frequency,

$$\omega_z = \sqrt{\frac{2Q\kappa U_{\text{end}}}{m}}. \quad (7.5)$$

The resulting radial potential gives rise to equations of motion on Mathieu form [143],

$$\begin{aligned} \frac{\partial^2 x}{\partial \tau^2} + [a + a_z(1 - \chi) - 2q \cos(2\tau)] &= 0, \\ \frac{\partial^2 y}{\partial \tau^2} + [-a + a_z(1 + \chi) + 2q \cos(2\tau)] &= 0, \end{aligned} \quad (7.6)$$

where the following dimensionless parameters have been introduced

$$q = \frac{2QU_{RF}}{mLr_0^2\Omega_{RF}}, \quad a = \frac{4QU_a}{mLr_0^2\Omega_{RF}}, \quad \tau = \frac{\Omega_{RF}t}{2} \quad \text{and} \quad a_z = -2\left(\frac{w_z}{\Omega_{RF}}\right)^2. \quad (7.7)$$

Mathieu equations defined by $\frac{\partial^2 x}{\partial \tau^2} + [a - 2q \cos(2\tau)] = 0$ have stable and unstable solutions depending on a and q as shown in Fig. 7.12(a) [144]. There exists an infinite number of configurations allowing for stable motion. In the experiments the trap is operated in the region depicted in Fig. 7.12(b). Defining $a_x = a + a_z(1 - \chi)$ and $a_y = -a + a_z(1 + \chi)$ (7.6) is brought on Mathieu form,

$$\begin{aligned} \frac{\partial^2 x}{\partial \tau^2} + [a_x - 2q \cos(2\tau)] &= 0, \\ \frac{\partial^2 y}{\partial \tau^2} + [a_y + 2q \cos(2\tau)] &= 0. \end{aligned} \quad (7.8)$$

Since the stability diagram is symmetric around the a -axis, the Mathieu equations have stable solutions for both $\{a_x, q\}$ and $\{a_y, q\}$ in the shaded region of Fig. 7.12(b),

$$\begin{aligned} x(t) &= x_0 \left[1 - \frac{q}{2} \cos(\Omega_{RF}t) \right] \cos(\omega_x t), \\ y(t) &= y_0 \left[1 + \frac{q}{2} \cos(\Omega_{RF}t) \right] \cos(\omega_y t), \\ z(t) &= z_0 \cos(\omega_z t), \end{aligned} \quad (7.9)$$

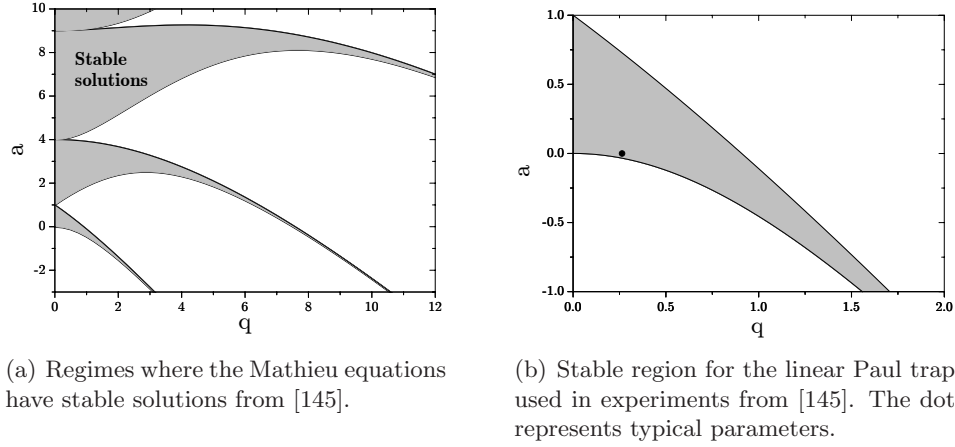


Figure 7.12

where $x(t)$ and $y(t)$ are 1.order solutions to (7.8) assuming $|a_x|, |a_y|, |q| \ll 1$ [29, 145] and $z(t)$ completes the picture. The radial ion-motion is thus described by a secular motion along the x-axis and y-axis with frequencies,

$$\omega_x = \frac{1}{2} \sqrt{\frac{q}{2} + a + a_z(1 - \chi)\Omega_{RF}}, \quad \omega_y = \frac{1}{2} \sqrt{\frac{q}{2} - a + a_z(1 + \chi)\Omega_{RF}} \quad (7.10)$$

superimposed by a fast oscillation at the RF-frequency of small amplitude, the ion micromotion. Neglecting micromotion, the ion undergoes harmonic motion in all three dimensions with frequencies $\omega_x, \omega_y, \omega_z$. The trap is operated at $\Omega_{RF}/2\pi = 11.5$ MHz or $\Omega_{RF}/2\pi = 16.7$ MHz and is constructed to have $\chi = 0.269$ and $L = 1.23$ [29]. For $\Omega_{RF}/2\pi = 16.7$, a typical choice of voltages ($U_{RF} = 400V$, $U_{end} = 7V$ and $U_a = 0V$) leads to parameters $q = 0.26$, $a_z = -0.0016$, $a_x = -0.0012$, $a_y = -0.0020$ and frequencies $\omega_z/2\pi = 0.47$ MHz, $\omega_y/2\pi = 1.51$ MHz and $\omega_x/2\pi = 1.53$ MHz. For more than one ion in the trap, the equations of motion and the stability regions are modified. For a detailed discussion see [145].

7.6.2 Micromotion

Ion micromotion induces time dependent Doppler-shifts in the rest frame of the ion and thereby alter the excitation spectrum of its atomic transitions. Experiments may therefore be affected by micromotion. In the description above the RF-field only modulates the radial motion, but if a small amount of RF-field is also produced on the end electrodes, axial micromotion can occur. The amplitude of axial micromotion, though, will be much smaller than the radial.

In the experiments presented in this thesis only course micromotion compensation was used, placing the ion in the centre of the trap where micromotion

is minimal. The coarse adjustment is done radially by observing the position of the ion on the CCD-camera when the RF-potential is lowered and moving the ion with the compensations voltages until its position is independent of the strength of the RF-potential. The same procedure with U_{end} places the ion in the centre of the axial confining potential. Fine compensation of micromotion will be implemented using the correlation method presented in [146]. Here a measurement of the correlation between the emission of photons and the RF-field is made. The correlations arise from the time dependent Doppler-shifts in the rest frame of the ion and can be used to estimate the micromotion velocity.

In the STIRAP experiments the laser beams are parallel to the axis and STIRAP is only sensitive to axial micromotion. The Doppler shift induced by a micromotion velocity, v ($\Delta_i/2\pi = \frac{1}{\lambda_i}v$) will imply a change in two-photon detuning. For the second STIRAP sequence the two wavelengths lie very close and the induced two-photon detuning will always be negligible. In the first, allowing for two-photon detunings below 0.5 MHz, we require an axial velocity below 0.4 m/s. This should be possible to reach even without fine compensation, but to ensure that this is the case, the correlation method will be used to measure the micromotion velocity. In future experiments with side-band cooling and gates, Raman transitions between the two Zeeman sublevels of $|S_{1/2}\rangle$ will be used. As described in [29] this will be achieved with lasers perpendicular to the trap axis. In this case radial micromotion will also be critical and fine compensation of micromotion necessary.

7.7 Magnetic fields

An external magnetic field will shift the Zeeman sublevels of the ion. It is desirable to be able to control this splitting and we try to minimise the magnetic fields from the environment experienced by the ions. The experimental chamber is therefore shielded by μ -metal¹². The μ -metal does not shield external magnetic fields completely and in order to control the magnetic field, a Hall-probe placed just outside the chamber, but inside the μ -metal shield measures the magnetic field in three dimensions. A non-zero field can be compensated with three coils placed outside the chamber. A time-dependent magnetic field is compensated by a continuous measurement of the magnetic field and a subsequent feedback-current to the coils. This enables us to maintain zero field within 1 mG, corresponding to a Larmor-frequency $\omega_L = g_i \cdot 1.4$ kHz, where the Landé factors (g_i) for Ca can be found in appendix B. The highest Larmor frequency is found for the $S_{1/2}$ with $g_i = 2$ and $\omega_L = 2.8$ kHz, which should not be critical for STIRAP. With the coils we can also create a non-zero magnetic field in any given direction.

¹² nickel-iron alloy with very high magnetic permeability

Chapter 8

STIRAP experiments

The first STIRAP experiments were presented in 1990 [40], where a beam of atoms, as mentioned earlier, passed two stationary laser beams effectively creating laser pulses seen by the atom. These experiments showed high transfer efficiencies and had the advantage that no residual light was present. When considering using STIRAP for different aspects of quantum logic single non-moving atoms are preferable. Experiments with non-moving atoms or molecules have been demonstrated [45,147,148], but all with ensembles of particles. This chapter describes an experiment where single ions are transferred with high efficiency using STIRAP. We present results on the second STIRAP sequence in the internal state detection scheme described in chapter 6.2, where population is transferred from the $|D_{3/2}\rangle$ state to the $|D_{5/2}\rangle$ state in $^{40}\text{Ca}^+$. Instead of the first STIRAP sequence we optically pump the population from $|S_{1/2}\rangle$ to $|D_{3/2}\rangle(m = \pm 3/2)$. The results were published in [I].

8.1 Optical pumping

The population initially in the ground state is optically pumped to the extreme Zeeman sublevels ($m = \pm 3/2$) of the $|D_{3/2}\rangle$ state, which is then the starting point for the experiments. We have chosen the Zeeman sublevels yielding the highest Clebsch-Gordan coefficients. As shown in Fig. 8.1 the 397 nm laser excites all population from $|S_{1/2}\rangle$ to $|P_{1/2}\rangle$, from where it decays either back to $|S_{1/2}\rangle$ or to $|D_{3/2}\rangle$. Population in $|D_{3/2}\rangle(m = \pm 1/2)$ is then pumped out with the 866 nm laser polarised along the direction of an applied magnetic field (the x-direction in Fig. 8.1). After some cycles all population therefore ends up in $|D_{3/2}\rangle(m = \pm 3/2)$. We investigate our ability to optically pump by loading a small Coulomb crystal into the trap. We apply the 397 nm and 866 nm lasers as described above in order to achieve that only $|D_{3/2}\rangle(m = \pm 3/2)$ is populated and we turn on the 850 nm and 854 nm with low power during 100 μs with polarisations along the direction of the magnetic field, so that only π -transitions are coupled as shown in Fig. 8.1. We use a magnetic field

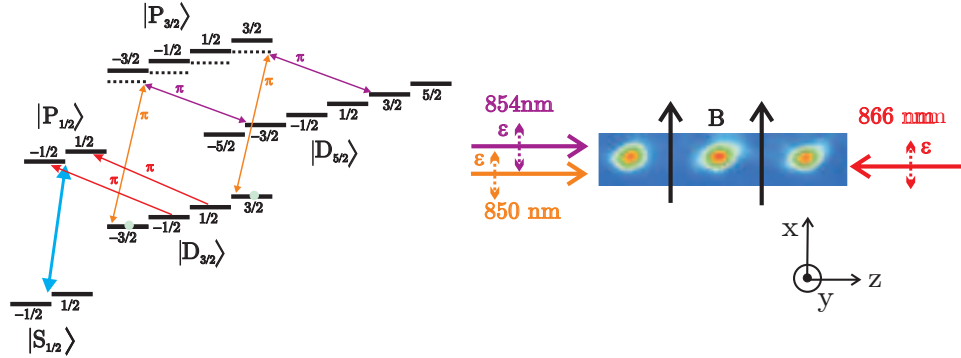


Figure 8.1: Laser fields applied during optical pumping from $|S_{1/2}\rangle$ to $|D_{3/2}\rangle$ ($m = \pm 3/2$). The 866 nm laser is polarised along the direction of a bias magnetic field, B , ensuring that the population is optically pumped to the $|D_{3/2}\rangle$ ($m = \pm 3/2$) Zeeman sublevels, because only two transitions are coupled. Subsequently, the 850 nm and 854 nm lasers are also applied with polarisations along the magnetic field and therefore only π transitions between $|D_{3/2}\rangle$, $|P_{3/2}\rangle$ and $|D_{5/2}\rangle$ are coupled.

of approximately 3 G and the Zeeman sublevels are therefore split, such that we can control which Zeeman level the lasers couple by an adjustment of the two photon resonance $\Delta_{\text{two}} = \Delta_{854} - \Delta_{850}$. Finally, we measure if some population is transferred from $|D_{3/2}\rangle$ to $|D_{5/2}\rangle$, by applying the 397 nm laser

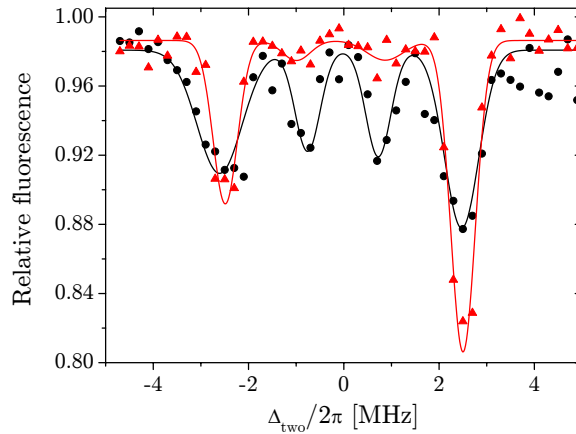


Figure 8.2: Relative fluorescence measured by the PMT as a function of the two-photon detuning Δ_{two} in the case where we populate all Zeeman sublevels in $|D_{3/2}\rangle$ (black) and in the case where we optically pump to the $|D_{3/2}\rangle$ ($m = \pm 3/2$) (red). The solid lines show a fit to Gaussian line-shapes. The smaller line width in the case with optical pumping is due to a smaller Rabi frequency. The strengths of the lines are not symmetric because the 397 nm laser does not populate the Zeeman sublevels of $P_{1/2}$ equally.

and the 866 nm laser with its polarisation scrambled to drive all $|D_{3/2}\rangle$ - $|P_{1/2}\rangle$ transitions. Simultaneously, we measure fluorescence.

We see a drop in fluorescence if population was transferred to the $|D_{5/2}\rangle$ state and show this as a function of the two-photon detuning in Fig. 8.2. The results show that when we do not optically pump (black dots) all four Zeeman sublevels are populated, while optical pumping (red dots) reduces the population in the ($m = \pm 1/2$) sublevels significantly and we estimate that less than 15% of the population is in ($m = \pm 1/2$) after optical pumping.

8.2 Setup and timing of STIRAP experiments

After optical pumping we perform STIRAP experiments with both lasers polarised along the bias magnetic field so we have effectively only two π -transitions as shown in Fig. 8.1. To analyse the results using the PMT we need three detection periods - one with all ions non-fluorescent, one with all ions fluorescent and one after the STIRAP experiment. The whole sequence used is shown in Fig. 8.3 and consists of four parts:

- In the first detection period we apply the Doppler cooling lasers (397 nm and polarisation scrambled 866 nm) and for repumping shelved popula-

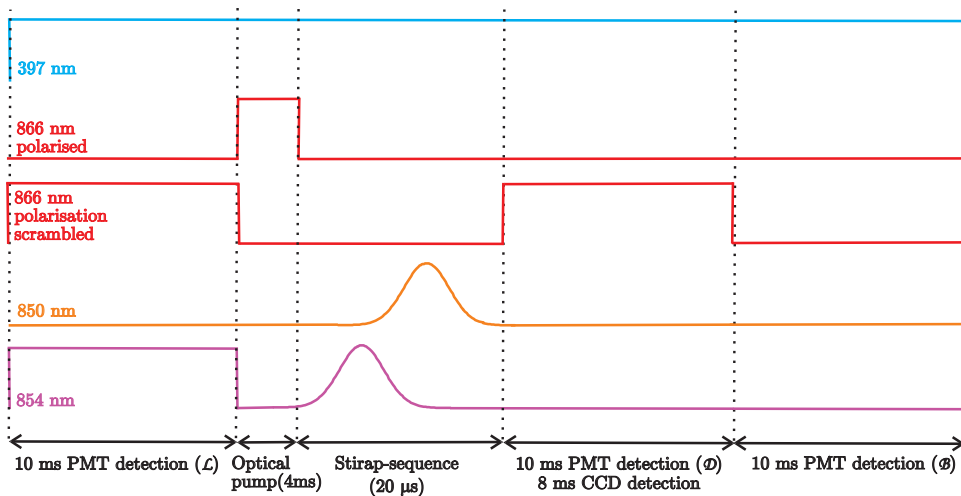


Figure 8.3: Laser sequence used in STIRAP experiments. First period is a detection period where all ions are in the fluorescent cooling cycle. This is followed by optical pumping, the two STIRAP pulses and then another period with the cooling lasers applied measuring fluorescent population remaining in the $|D_{3/2}\rangle$ -state. The final period is used to measure the background level of scattered light when all population is trapped in the $|D_{3/2}\rangle$ state, because the 866 nm laser is not applied to repump population back into the cooling cycle.

tion in $|D_{5/2}\rangle$ also the 854 nm is applied. In this period all ions will therefore be fluorescent (\mathfrak{L}).

- We then optically pump with the π -polarised 866 nm laser and the 397 nm laser and apply two STIRAP pulses. If the process is efficient all population is now in the $|D_{5/2}\rangle$ state.
- The second detection period again applies the two Doppler cooling lasers and ions remaining in $|D_{3/2}\rangle$ will fluoresce (\mathfrak{D}).
- To measure a background fluorescence level from for example scattered light, we apply only the 397 nm laser. Ions that are not already in $|D_{5/2}\rangle$ are then shelved in $|D_{3/2}\rangle$ and no ions fluoresce (\mathfrak{B}).

We name the three measured levels of fluorescence \mathfrak{L} (light), \mathfrak{D} (dark), \mathfrak{B} (background) and calculate the transfer efficiency as $\frac{\mathfrak{D}-\mathfrak{B}}{\mathfrak{L}-\mathfrak{B}}$.

Experimental parameters

The 850 nm and 854 nm lasers are focused to a 60 μm waist in the trap centre. We measure their power level, $P_{850} = 2.4$ mW, $P_{854} = 3.6$ mW and calculate the Rabi frequencies on the $m = \pm 3/2 \rightarrow m = \pm 3/2$ transitions from the formula derived in appendix B,

$$\begin{aligned}\Omega_{850,3/2}/2\pi &\approx 100 \text{ MHz}, \\ \Omega_{854,3/2}/2\pi &\approx 250 \text{ MHz}.\end{aligned}$$

With the RF-switch in the AOM open, the residual Rabi frequencies were measured to

$$\begin{aligned}\Omega_{850,3/2,\text{off}}/2\pi &\approx 0.9 \text{ MHz}, \\ \Omega_{854,3/2,\text{off}}/2\pi &\approx 4.4 \text{ MHz}\end{aligned}$$

With the RF-switch in the AOM closed, the residual Rabi frequencies were measured to

$$\begin{aligned}\Omega_{850,3/2,\text{off}}/2\pi &\approx 0.2 \text{ MHz}, \\ \Omega_{854,3/2,\text{off}}/2\pi &\approx 0.3 \text{ MHz}.\end{aligned}$$

The RF-switch suppresses the RF-power with 100 dB, but a part of the residual light originates from scattered 0.order light in the AOM crystal and is therefore not reduced by the RF-switch. Both lasers are red-detuned from resonance to avoid one-photon excitations: $\Delta_{850}/2\pi \approx \Delta_{854}/2\pi \approx 600$ MHz and we use Gaussian pulses as defined in (2.22). The magnetic field in all STIRAP experiments was $B_x \approx 1$ G.

8.3 Delay scan

We first investigate the transfer efficiency when we vary the delay between pulses with width $\tau = 3 \mu\text{s}$. The detunings are adjusted so the two-photon detuning is $\Delta_{\text{two}}/2\pi = -0.9 \text{ MHz}$, and not exactly on two-photon resonance as explained in chapter 7.4.4. For each delay we run the sequence 50 times.

8.3.1 Single atom analysis with CCD camera

With the CCD-camera we take pictures of the ions after the STIRAP pulses with an 8 ms exposure time and determine if an ion fluoresces or not. An example of such pictures for different delays are shown in Fig. 8.4, where the effect of STIRAP can be observed on single ion level. Note that only for counter intuitive pulse sequences (positive pulse delays) ions are transferred to the non-fluorescent $|D_{5/2}\rangle$ -state. The transfer efficiency is determined from investigations of the 50 sequences for each delay and Fig. 8.5 shows delay scans for the ion string with nine ions pictured in Fig. 8.4. Fig. 8.5 shows that the transfer efficiency is independent of the ion position in the trap. These delay scans show that for intuitive pulse order and well separated pulses no population is transferred, and as the pulses begin to overlap the transfer

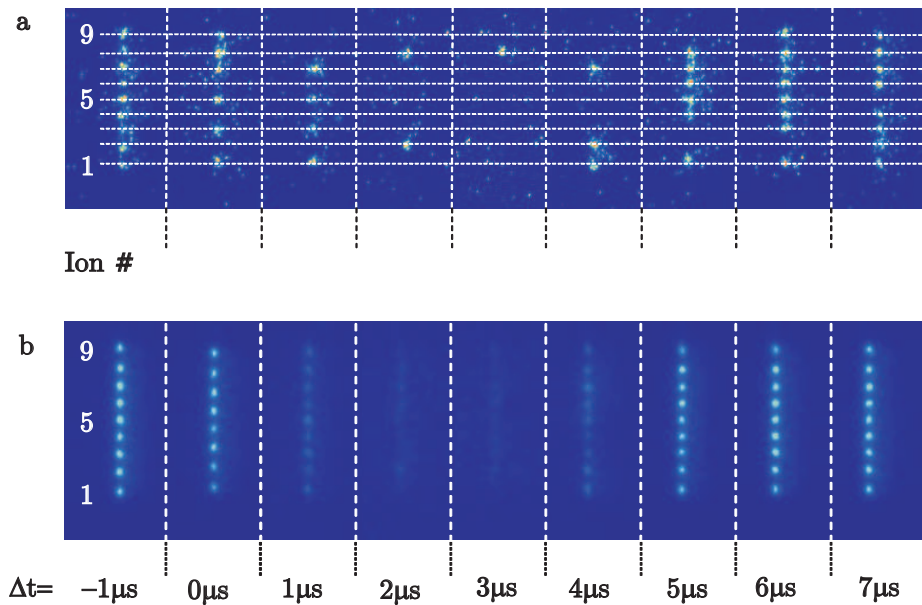


Figure 8.4: Pictures from CCD camera at increasing time delays between pulses. The upper panel shows pictures from individual runs while the lower shows an average over 50 runs.

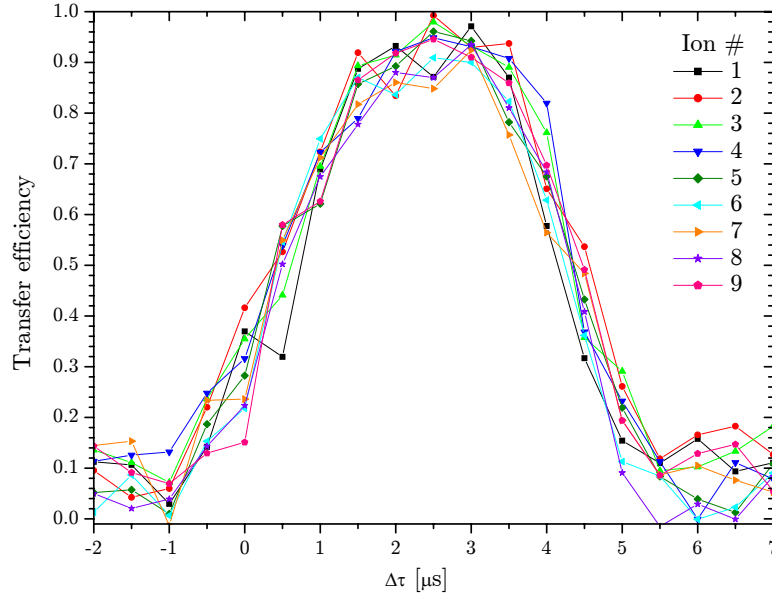


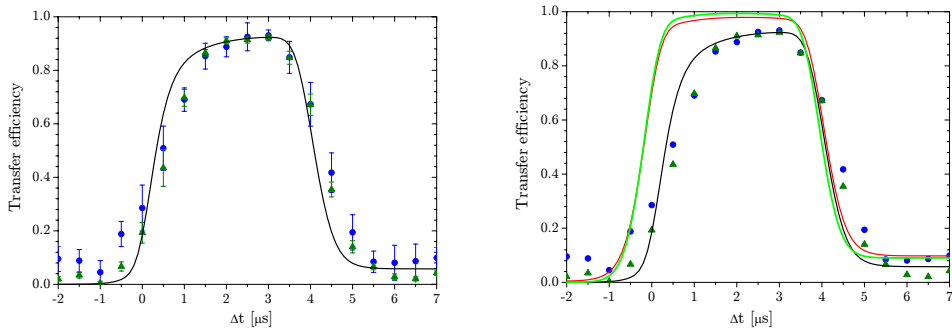
Figure 8.5: STIRAP transfer efficiency as a function of delay between pulses for individual ions analysed with CCD-camera and averaged over 50 sequences.

efficiency increases because of the creation of a Raman transition, but first when the pulse order is counter intuitive the transfer rises above 0.5 because STIRAP becomes efficient. For counter intuitive but separated pulses the efficiency drops to a constant level at 0.05 due to a off-resonant one-photon excitation induced by the 850 nm pulse.

8.3.2 Average of more atoms

Averaging over and finding the standard deviation of the nine ions in Fig. 8.5 gives a final estimation of the transfer efficiency as depicted with blue circles in Fig. 8.6(a). The results obtained from the CCD-pictures are compared with the PMT measurements. The PMT measures the fluorescence level in the three periods indicated in Fig. 8.3. For each experiment with 50 sequences we find the transfer efficiency, $\frac{\mathcal{D}-\mathcal{B}}{\mathcal{C}-\mathcal{B}}$, and from the 50 sequences we calculate the average and standard deviation as shown with the green circles in Fig. 8.6(a). The PMT and CCD results show good agreement.

The experimental results are compared with a theoretical simulation solving the density matrix master equation for the five level system in Fig. 6.1 neglecting the Zeeman structure. The simulations are made with Rabi frequencies, laser phase fluctuations and residual light levels that optimises the agreement between theory and experiment. We find $\Omega_{850}/2\pi = 90$ MHz, $\Omega_{854}/2\pi = 225$ MHz, 10 kHz phase fluctuations for both lasers and residual Rabi frequencies at 1% of the peak value for the 850 nm laser and 2% for the 854 nm when



(a) Average and standard deviation of 50 sequences and 9 ions measured with CCD (blue) and PMT (green). The solid black line is a numerical simulation with laser phase fluctuations and residual light included.

(b) Comparison between measured results (blue circles and green triangles) and numerical simulations. The black curve is as in (a). The efficiency is optimised by first neglecting the laser phase fluctuations (red) and further by disregarding the residual light as well (light green curve).

Figure 8.6: STIRAP transfer efficiency as a function of delay between pulses measured with CCD camera, PMT and compared with the a numerical propagation of the density matrix master equation using parameters $\Omega_{850,3/2}/2\pi = 90$ MHz, $\Omega_{854,3/2}/2\pi = 225$ MHz, $\Delta_{850}/2\pi = 600$ MHz, $\Delta_{854}/2\pi = 600 - 0.9$ MHz and 2 kHz phase fluctuations of all lasers. The residual light levels used were 1% of the peak value for the 850 nm laser and 2% for the 854 nm during the 20 μ s where the RF-switch is open and 0.1% for both lasers during the 200 μ s where the RF-switch is closed. All simulations are with $\Omega_{397}/2\pi = 100$ MHz. The light green curve in (b) where residual light is neglected is calculated on two-photon resonance where the efficiency then is optimal.

the RF-switch is open and 0.1% for both lasers when the RF-switch is closed. There is a discrepancy between the Rabi frequencies measured and the ones used in the simulations, which we explain by a non-perfect overlap between the ion-string and the focused laser beam as well as the fact that the optical pumping was not perfect and therefore a part of the transfer takes place on the $m = \pm 1/2 \leftrightarrow m = \pm 1/2$ transitions, where the coupling is weaker. The residual light levels are approximately as measured. The 3 μ s wide pulses used in the experiment indicate that coherence must be kept for approximately ten microseconds and hence longer than the 2 μ s timescale, where 2 kHz phase fluctuations were measured as shown in appendix C. The 10 kHz phase fluctuations are thus a realistic assumption.

The optimal delay between the pulses is approximately 3.0 μ s where we achieve a transfer efficiency of $93 \pm 2\%$. The two main error sources are the laser phase fluctuations and the residual light. We show this in Fig. 8.6(b), where the red curve neglects the laser phase fluctuations and the light green curve also disregards residual light. The transfer efficiency can be improved

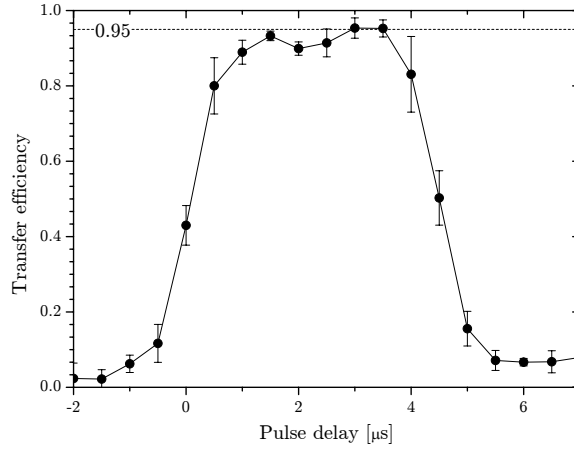


Figure 8.7: Delay scan with two ions. The transfer efficiency is measured with the PMT. The average and standard deviation is found from 50 sequences.

significantly by a better phase stabilisation of the lasers combined with a more efficient shut down of the laser light. We achieve a higher transfer efficiency with only two ions in the string, where $95 \pm 2\%$ was obtained as shown in Fig. 8.7. The slightly lower transfer efficiency in the nine ion case may be due to a higher RF-heating rate.

8.4 Frequency scan

The STIRAP efficiency depends significantly on the two-photon detuning and with a fixed delay ($\Delta t = 2 \mu\text{s}$) between pulses with pulse width, $\tau = 3 \mu\text{s}$ we measure the dependence scanning the frequency of the 854 nm laser as shown in Fig. 8.8. The experimental results arise from eight scans (each averaged over 50 sequences) of ion strings with between one and ten ions measured with the PMT. The average and the standard deviation are calculated from these eight results and compared with a simulation solving the density matrix master equation with the same parameters as in the simulations presented in Fig. 8.6. The asymmetry of the spectrum is due to the unbalanced Rabi frequencies as described in chapter 2.3.2. The residual light gives rise to a parasitic Raman resonance (see chapter 7.4.4) and the best transfer efficiency is therefore not achieved on two-photon resonance, but with a small negative two-photon detuning, $\Delta_{\text{two}}/2\pi = -0.9 \text{ MHz}$. Here we achieve a transfer efficiency of $91.8 \pm 0.7\%$.

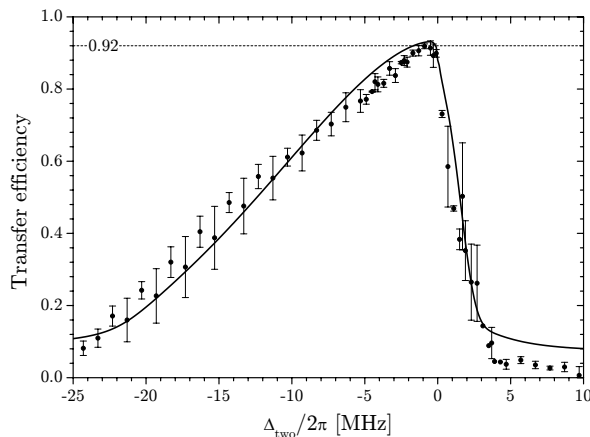


Figure 8.8: STIRAP transfer efficiency as a function of the two-photon detuning. The experimental results are an average over the PMT results for 8 consecutive scans. The solid line is a simulation propagating the density matrix using the same parameters as in Fig. 8.6(a).

8.5 The first STIRAP process

In order to complete the internal state detection, the first STIRAP process transferring population from $|\downarrow\rangle = |S_{1/2}\rangle(m = -1/2)$ to $|D_{3/2}\rangle$ must also be efficiently implemented, and this process is more complicated than the second.

The two laser fields involved in the first STIRAP process have very different wavelengths and they are locked to different cavities. Each cavity have a maximal drift of 2 MHz/h and the drift in two-photon resonance can therefore become as high as 4 MHz/h. It will therefore be advantageous to lock the 866 nm and 794 nm (source to the 397 nm) lasers to the same cavity. In this case the drift in two-photon detuning will be below 1 MHz/h. The wavelength difference of the two fields also entail that axial micromotion must be kept below $v = 0.5$ m/s, as discussed in chapter 7.6.2.

Another aspect is the purity of the polarisation of the 397 nm laser, which we use to make the shelving state selective. The 397 nm laser should have a pure σ^+ polarisation (see Fig. 8.9), but might also have small components of σ^- and π polarisations due to magnetic field errors. In [III] we investigate the detection error due to the unwanted polarisation components and conclude that in order to achieve errors below 1% we require less than 2% of π polarised and less than 4% of σ^- polarised light for parameters similar to the ones used for the second STIRAP experiment. These requirements should be achievable using Glan polarisers.

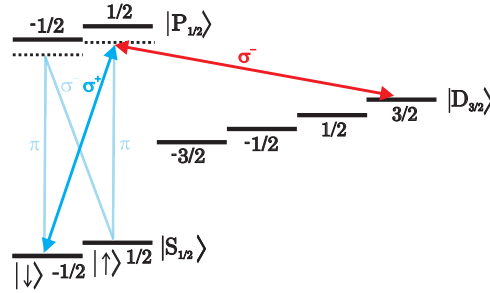


Figure 8.9: Zeeman sublevels of the three states involved in the first STIRAP process. Ideally, the $|S_{1/2}\rangle$ and $|P_{1/2}\rangle$ states are coupled by a purely σ_+ polarised 397 nm laser (blue) and the $|P_{1/2}\rangle$ and $|D_{3/2}\rangle$ states are coupled by a purely σ_- polarised 866 nm laser (red). The light blue arrows indicate parasitic σ_- and π components of the 397 nm field.

8.6 Conclusion

We have demonstrated how STIRAP can be used to transfer population efficiently between internal states of cold trapped ions and find a maximum transfer efficiency of $95 \pm 2\%$. We have argued that the limitations are due to the laser phase fluctuations and the residual light. Reducing these two error sources should make it possible to achieve transfer efficiencies above 99%. The transfer is proposed as a part of an internal state detection of the Zeeman sublevels of the ground state, where another STIRAP process is used to transfer the population from $|S_{1/2}\rangle$ to $|D_{3/2}\rangle$. This first STIRAP process will be more complicated to implement, but there is no fundamental limit to the achievable efficiency.

Chapter 9

Summary and Outlook

Quantum computation is still far from the goal of implementing algorithms with a large number of qubits that can outperform their classical counterparts. An important challenge is not only to implement initialisation, gates and read out, but also to perform each step with high fidelity. To achieve this, it may be advantageous to use adiabatic processes with their potential robustness. This thesis have considered different ways of employing adiabaticity in quantum computation as well as for creation of many-particle entangled states.

Chapter 3 and 5 presented quantum gates based on adiabatic following of dark states acquiring geometric phases. The system remains in the dark states when STIRAP processes are used and adiabaticity maintained. The gates are quite insensitive to fluctuations in the controlling parameters and are in that respect robust. Robustness against noise is a more complicated question. Chapter 4 showed how the geometric phases acquired in the implementation of the Hadamard gate become complex and cause a decrease in fidelity. The fidelity, though, is still above 0.99 for realistic experimental dephasing rates and apart from the influence of noise it depends on our ability to maintain adiabaticity and on the robustness of the geometric phases. Adiabaticity is achieved using high Rabi frequencies and long pulses, but it is on the other hand preferable to use the shortest possible pulses to achieve fast gates that are less sensitive to decoherence. Choosing the optimal pulse width will be a trade-off. When adiabaticity is ensured, the pulse shapes, the delay between pulses, the relative field strengths and relative phases of the applied laser fields must be controlled in order to achieve the desired geometric phases. Of these only control of the relative phase is challenging and it is preferable to implement the gates in systems where all involved lasers originate from the same source implying the use of Zeeman or hyperfine sublevels coupled to the same excited state.

The one-qubit gates can be implemented in various systems such as optically trapped neutral atoms, trapped ions and rare-earth ions doped into crystals, while the two-qubit gate presented in chapter 5 is based on the long

range dipole-dipole interaction in Rydberg atoms. It is an open question to what extent the geometric gates are more robust than the dynamic and further theoretical investigations including comparative studies are needed to shed light on the benefits of geometric gates. In spite of this, we conclude that the one-qubit gate of chapter 3 and the two-qubit gate of chapter 5 combined yield a universal set of quantum gates that can be implemented experimentally with high fidelities.

The experimental investigations of adiabatic transfer between internal states of trapped laser cooled $^{40}\text{Ca}^+$ ions in chapter 8 showed a 95% efficiency and comparison with numerical studies revealed that the limiting factor was a combination of residual light and laser phase fluctuations. These are not fundamental limitations, but must be improved in order to achieve an efficiency of the qubit detection scheme proposed in chapter 6 that is high enough to make it a true candidate for read out of the ion trap quantum computer.

The Rydberg atoms are not only a candidate for quantum computation, but as we show in chapter 5 a single STIRAP sequence applied to tens of atoms will entangle them with high fidelity. Apart from being of fundamental interest the produced entangled states are important for precision metrology. The work showed how the Rydberg blockade in conjunction with the adiabatic processes produces a Jaynes-Cummings dynamics, that is sufficient to produce a variety of interesting states and it could be interesting to investigate this further.

9.1 Dansk resumé

Kvantecomputeren begyndte som en fascinerende ide, hvor smarte algoritmer udnytter kvantemekanikkens parallelitet til at løse problemer, som er utilgængelige på klassiske computere. I løbet af de sidste årtier har eksperimentelle fremskridt muliggjort manipulation af enkelte atomer og ioner, som bruges til at realisere kvantegates. Udfordringen i dag er at skalere computeren, hvilket kræver at alle manipulationer skal udføres med høj præcision, fordi fejlene ellers vil akkumulere og ødelægge slutresultatet. For at opnå dette kan det være en fordel at bruge adiabatisk processer.

I den teoretiske del af afhandlingen præsenteres kvantegates baseret på adiabatisk processer, som er robuste i forhold til fluktuationer i parametre og det diskuteres, hvordan de påvirkes af støj. De adiabatisk processer anvendes også til at entangle mange neutrale atomer, som vekselvirker på grund af deres store dipolmomenter. Den eksperimentelle del viser, hvordan population effektivt kan overføres fra en intern tilstand til en anden i fangede laserkølede $^{40}\text{Ca}^+$ -ioner og vi demonstrerer en effektivitet på 95%. Afvigelsen fra 100% effektivitet tilskrives fluktuationer i lasernes relative fase, og at ioner utilsigtet bliver belyst af laserne også før og efter den adiabatisk proces, hvilket kan ødelægge sluttstanden.

Appendices

Appendix A

Principles of numerical simulations

The purpose of this appendix is to give an overview of the different numerical simulations used throughout the thesis. We demonstrate the methods on the three level lambda system shown in Fig. A.1, but the principles are directly extended to systems with more than three levels as well as more than one atom.

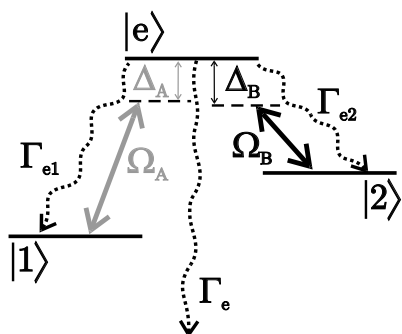


Figure A.1: Three level lambda-system coupled by two laser fields with Rabi frequencies Ω_A and Ω_B detuned Δ_A and Δ_B with respect to resonance. Decay rates from the excited state and out of the system is indicated with Γ_e , decay to $|1\rangle$ with Γ_{e1} and decay to $|2\rangle$ with Γ_{e2} . $|1\rangle$ and $|2\rangle$ are assumed stable.

A.1 The Schrödinger equation

We first describe only the Schrödinger equation neglecting decay and other decoherence sources. We consider external laser fields as plane monochromatic waves and in the dipole approximation the field interacts with an electron via the potential,

$$V = -e\bar{r}\left(\frac{1}{2}\hat{\epsilon}E_0e^{-i\omega t} + c.c.\right), \quad (\text{A.1})$$

Using the enumeration of the levels and laser fields shown in Fig. A.1 we can write all nonzero couplings,

$$\begin{aligned}
V_{1e} &= -e\bar{r}_{1e}\left(\frac{1}{2}\hat{\varepsilon}E_0e^{-i\omega t} + c.c.\right)_A, \\
V_{e1} &= -e\bar{r}_{e1}\left(\frac{1}{2}\hat{\varepsilon}E_0e^{-i\omega t} + c.c.\right)_A, \\
V_{2e} &= -e\bar{r}_{2e}\left(\frac{1}{2}\hat{\varepsilon}E_0e^{-i\omega t} + c.c.\right)_B, \\
V_{e2} &= -e\bar{r}_{e2}\left(\frac{1}{2}\hat{\varepsilon}E_0e^{-i\omega t} + c.c.\right)_B.
\end{aligned} \tag{A.2}$$

Solving the Schrödinger equation corresponds to solving a set of coupled equations for the probability amplitudes $\{a_i\}$,

$$\begin{aligned}
i\hbar\dot{a}_1 &= E_1a_1 - \frac{1}{2}e\bar{r}_{1e}(\hat{\varepsilon}E_0e^{-i\omega t} + c.c.)_Aa_e, \\
i\hbar\dot{a}_e &= E_ea_e - \frac{1}{2}e\bar{r}_{e1}(\hat{\varepsilon}E_0e^{-i\omega t} + c.c.)_Aa_1 - \frac{1}{2}e\bar{r}_{e2}(\hat{\varepsilon}E_0e^{-i\omega t} + c.c.)_Ba_2, \\
i\hbar\dot{a}_2 &= E_2a_2 - \frac{1}{2}e\bar{r}_{2e}(\hat{\varepsilon}E_0e^{-i\omega t} + c.c.)_Ba_e,
\end{aligned} \tag{A.3}$$

where $\{E_i\}$ are energies of the atomic levels. We define Rabi frequencies,

$$\begin{aligned}
\Omega_A &= \frac{eE_0}{\hbar}\bar{r}_{e1} \cdot \hat{\varepsilon}, \\
\Omega_B &= \frac{eE_0}{\hbar}\bar{r}_{e2} \cdot \hat{\varepsilon},
\end{aligned} \tag{A.4}$$

and detunings,

$$\begin{aligned}
\Delta_A &= \frac{E_1 - E_e}{\hbar} - \omega_A, \\
\Delta_B &= \frac{E_2 - E_e}{\hbar} - \omega_B.
\end{aligned} \tag{A.5}$$

Choosing $E_1 = 0$ and introducing convenient phase shifted probability amplitudes,

$$\begin{aligned}
a_1 &= c_1, \\
a_e &= c_e e^{-i\omega_A t}, \\
a_2 &= c_2 e^{-i(\omega_A - \omega_B)t},
\end{aligned} \tag{A.6}$$

we can rewrite (A.3) in the rotating wave approximation,

$$\begin{aligned}
i\dot{c}_1 &= -\frac{1}{2}\Omega_A^*c_e, \\
i\dot{c}_e &= \Delta_Ac_e - \frac{1}{2}\Omega_Ac_1 - \frac{1}{2}\Omega_Bc_2, \\
i\dot{c}_2 &= (\Delta_A - \Delta_B)c_2 - \frac{1}{2}\Omega_B^*c_e.
\end{aligned} \tag{A.7}$$

These differential equations correspond exactly to the Hamiltonian in (2.14) and when we in the thesis show numerical solutions of the Schrödinger equation we refer to propagating these equations using a Runge-Kutta routine in Matlab. When the systems become large, as in the many-atom calculations in chapter 5.3, it is convenient to calculate the propagation by,

$$|\psi(t + dt)\rangle = \exp\left(\frac{-iHdt}{\hbar}\right) |\psi(t)\rangle, \tag{A.8}$$

where H is assumed constant during the small time step, dt .

Spontaneous emission out of the system can be included as imaginary decay terms in (A.7), but when we wish to investigate decay and decoherence the density matrix is more suitable.

A.2 Density matrix

For the closed system the density matrix is defined as $\rho_{ij} = c_i c_j^*$ and its time evolution given by $\dot{\rho}_{ij} = \dot{c}_i c_j^* + c_i \dot{c}_j^*$ and we find,

$$\begin{aligned}
\dot{\rho}_{11} &= -\frac{1}{2}i(\Omega_A\rho_{1e} - \Omega_A^*\rho_{e1}), \\
\dot{\rho}_{ee} &= \frac{1}{2}i(\Omega_B\rho_{2e} - \Omega_B^*\rho_{e2}) + \frac{1}{2}i(\Omega_B\rho_{2e} - \Omega_B^*\rho_{e2}), \\
\dot{\rho}_{22} &= -\frac{1}{2}i(\Omega_B\rho_{2e} - \Omega_B^*\rho_{e2}), \\
\dot{\rho}_{1e} &= i\Delta_A\rho_{1e} + \frac{1}{2}i\Omega_A^*(\rho_{ee} - \rho_{11}) - \frac{1}{2}i\Omega_B^*\rho_{12}, \\
\dot{\rho}_{12} &= i(\Delta_A - \Delta_B)\rho_{12} + \frac{1}{2}i\Omega_A^*\rho_{e2} - \frac{1}{2}i\Omega_B^*\rho_{1e}, \\
\dot{\rho}_{2e} &= i\Delta_B\rho_{2e} + \frac{1}{2}i\Omega_B^*(\rho_{ee} - \rho_{22}) - \frac{1}{2}i\Omega_A^*\rho_{21}.
\end{aligned} \tag{A.9}$$

The diagonal elements now directly display the population in the three atomic states, while the off-diagonal elements express the coherence among the different states and give the relative phases between them. The closed atomic

system is first extended to include spontaneous emission, where the decay rates (Γ_e , Γ_{e1} and Γ_{e2}) changes the populations as well as the coherences [108],

$$\begin{aligned}
\dot{\rho}_{11} &= -\frac{1}{2}i(\Omega_A\rho_{1e} - \Omega_A^*\rho_{e1}) + \Gamma_{e1}\rho_{ee}, \\
\dot{\rho}_{ee} &= \frac{1}{2}i(\Omega_B\rho_{2e} - \Omega_B^*\rho_{e2}) + \frac{1}{2}i(\Omega_B\rho_{2e} - \Omega_B^*\rho_{e2}) - (\Gamma_e + \Gamma_{e1} + \Gamma_{e2})\rho_{ee}, \\
\dot{\rho}_{22} &= -\frac{1}{2}i(\Omega_B\rho_{2e} - \Omega_B^*\rho_{e2}) + \Gamma_{e2}\rho_{ee}, \\
\dot{\rho}_{1e} &= i\Delta_A\rho_{1e} + \frac{1}{2}i\Omega_A^*(\rho_{ee} - \rho_{11}) - \frac{1}{2}i\Omega_B^*\rho_{12} - \frac{1}{2}(\Gamma_e + \Gamma_{e1} + \Gamma_{e2})\rho_{1e}, \\
\dot{\rho}_{12} &= i(\Delta_A - \Delta_B)\rho_{12} + \frac{1}{2}i\Omega_A^*\rho_{e2} - \frac{1}{2}i\Omega_B^*\rho_{1e}, \\
\dot{\rho}_{2e} &= i\Delta_B\rho_{2e} + \frac{1}{2}i\Omega_B^*(\rho_{ee} - \rho_{22}) - \frac{1}{2}i\Omega_A^*\rho_{21} - \frac{1}{2}(\Gamma_e + \Gamma_{e1} + \Gamma_{e2})\rho_{2e}.
\end{aligned} \tag{A.10}$$

Phase fluctuations are introduced as stochastic phases $\phi_i(t)$ on the electric fields and taking these into account (A.3) is modified to

$$\begin{aligned}
i\hbar\dot{a}_1 &= E_1a_1 - \frac{1}{2}e\bar{r}_{1e}(\hat{\varepsilon}E_0e^{-i\omega t}e^{-i\phi(t)} + c.c.)_Aa_e, \\
i\hbar\dot{a}_e &= E_ea_e - \frac{1}{2}e\bar{r}_{e1}(\hat{\varepsilon}E_0e^{-i\omega t}e^{-i\phi(t)} + c.c.)_Aa_1 - \frac{1}{2}e\bar{r}_{e2}(\hat{\varepsilon}E_0e^{-i\omega t}e^{-i\phi(t)} + c.c.)_Ba_2, \\
i\hbar\dot{a}_2 &= E_2a_2 - \frac{1}{2}e\bar{r}_{2e}(\hat{\varepsilon}E_0e^{-i\omega t}e^{-i\phi(t)} + c.c.)_Ba_e.
\end{aligned} \tag{A.11}$$

We now go into the rotating wave approximation also with respect to these phases,

$$\begin{aligned}
a_1 &= c_1, \\
a_e &= c_e e^{-i\omega_A t} e^{-i\phi_A(t)}, \\
a_2 &= c_2 e^{-i(\omega_A - \omega_B)t} e^{-i(\phi_A(t) - \phi_B(t))},
\end{aligned} \tag{A.12}$$

and find the populations unaffected, but the coherences are modified,

$$\begin{aligned}
\dot{\rho}_{1e} &= i(\Delta_A + \dot{\phi}_A(t))\rho_{1e} + \frac{1}{2}i\Omega_A^*(\rho_{ee} - \rho_{11}) - \frac{1}{2}i\Omega_B^*\rho_{12} - \frac{1}{2}(\Gamma_e + \Gamma_{e1} + \Gamma_{e2})\rho_{1e}, \\
\dot{\rho}_{12} &= i(\Delta_A - \Delta_B + \dot{\phi}_A(t) - \dot{\phi}_B(t))\rho_{12} + \frac{1}{2}i\Omega_A^*\rho_{e2} - \frac{1}{2}i\Omega_B^*\rho_{1e}, \\
\dot{\rho}_{2e} &= i(\Delta_B + \dot{\phi}_B(t))\rho_{2e} + \frac{1}{2}i\Omega_B^*(\rho_{ee} - \rho_{22}) - \frac{1}{2}i\Omega_A^*\rho_{21} - \frac{1}{2}(\Gamma_e + \Gamma_{e1} + \Gamma_{e2})\rho_{2e}.
\end{aligned} \tag{A.13}$$

Now, if we assume that the process leading to the phase fluctuations is Markovian the spectrum of the laser will be Lorentzian and its first order correlation function is [149]

$$\langle e^{\phi_i(t)} e^{\phi_i(t')} \rangle = e^{-\Gamma_i(t-t')}, \quad (\text{A.14})$$

where Γ_i is the bandwidth of the Lorentzian spectrum for the i 'th laser field. It was shown in [149] that in this situation (A.13) can be averaged over the stochastic fluctuations of the phase to yield,

$$\begin{aligned} \dot{\rho}_{11} &= -\frac{1}{2}i(\Omega_A \rho_{1e} - \Omega_A^* \rho_{e1}) + \Gamma_{e1} \rho_{ee}, \\ \dot{\rho}_{ee} &= \frac{1}{2}i(\Omega_B \rho_{2e} - \Omega_B^* \rho_{e2}) + \frac{1}{2}i(\Omega_B \rho_{2e} - \Omega_B^* \rho_{e2}) - (\Gamma_e + \Gamma_{e1} + \Gamma_{e2}) \rho_{ee}, \\ \dot{\rho}_{22} &= -\frac{1}{2}i(\Omega_B \rho_{2e} - \Omega_B^* \rho_{e2}) + \Gamma_{e2} \rho_{ee}, \\ \dot{\rho}_{1e} &= (i\Delta_A - \Gamma_A) \rho_{1e} + \frac{1}{2}i\Omega_A^* (\rho_{ee} - \rho_{11}) - \frac{1}{2}i\Omega_B^* \rho_{12} - \frac{1}{2}(\Gamma_e + \Gamma_{e1} + \Gamma_{e2}) \rho_{1e}, \\ \dot{\rho}_{12} &= (i\Delta_A - i\Delta_B - \Gamma_A - \Gamma_B) \rho_{12} + \frac{1}{2}i\Omega_A^* \rho_{e2} - \frac{1}{2}i\Omega_B^* \rho_{1e}, \\ \dot{\rho}_{2e} &= (i\Delta_B - \Gamma_B) \rho_{2e} + \frac{1}{2}i\Omega_B^* (\rho_{ee} - \rho_{22}) - \frac{1}{2}i\Omega_A^* \rho_{21} - \frac{1}{2}(\Gamma_e + \Gamma_{e1} + \Gamma_{e2}) \rho_{2e}. \end{aligned} \quad (\text{A.15})$$

As discussed in chapter 4.1.1 the density matrix including decay and decoherence as described above can be written as a Lindblad master equation, with suitable Lindblad operators, and with these operators the quantum Monte Carlo method introduced in chapter 4.1.2 can also be used.

Appendix B

Properties of $^{40}\text{Ca}^+$

B.1 Characteristics

The five dipole allowed transitions in $^{40}\text{Ca}^+$ are characterised by the wavelengths and linewidths [110], from which the saturation intensities can be calculated.

Transition	λ [nm]	I_{sat} [mW/cm ²]	$\Gamma/2\pi$
$S_{1/2} - P_{1/2}$	396.847	43.3	20.7
$S_{1/2} - P_{3/2}$	393.366	46.2	21.5
$D_{3/2} - P_{1/2}$	866.241	0.34	1.69
$D_{3/2} - P_{3/2}$	849.802	0.038	0.177
$D_{5/2} - P_{3/2}$	854.209	0.33	1.58

The $D_{5/2}$ and $D_{3/2}$ states are metastable and their lifetimes have been investigated in several experiments. The most precise measurements have been performed with a single trapped ion yielding: $\tau_{D_{3/2}} = 1176 \pm 11$ ms and $\tau_{D_{5/2}} = 1168 \pm 9$ ms [80].

B.1.1 Zeeman structure

A magnetic field introduces a Zeeman structure of the energy levels. The Zeeman splitting in $^{40}\text{Ca}^+$ is given by

$$\Delta_i/2\pi = \frac{g_i m_i \mu_B B}{\hbar} = g_i m_i B \times 1.4 \text{ MHz/G} \quad (\text{B.1})$$

where the Landé factors are:

State	$S_{1/2}$	$P_{1/2}$	$P_{3/2}$	$D_{3/2}$	$D_{5/2}$
g	2	2/3	4/3	4/5	6/5

B.2 Rabi frequencies

In a two-level atom with transition frequency ω coupled by a laser field with field strength E_0 and decay rate from the upper level Γ , the Rabi frequency (χ) is simply [108],

$$\chi^2 = \frac{\Gamma^2}{2} \frac{I}{I_{\text{sat}}}, \quad (\text{B.2})$$

where the intensity $I = \frac{1}{2}c\epsilon_0 E_0^2$ and the saturation intensity

$$I_{\text{sat}} = \frac{\hbar\Gamma\omega^3}{12\pi c^2}, \quad (\text{B.3})$$

yields

$$\chi^2 = \frac{3\pi\Gamma c^3 \epsilon_0 E_0^2}{\hbar\omega^3}. \quad (\text{B.4})$$

This Rabi frequency only describes the coupling in a two-level atom and we call it the two-level Rabi frequency.

In an atom with fine structure, the Rabi frequency for a one-photon transition between a lower state $|J, m\rangle$ and an upper state $|J', m'\rangle$ is defined from the atomic dipole moment operator coupled to the electric field

$$\Omega_{f,i} = \frac{eE_0}{\hbar} \langle J', m' | \hat{\epsilon} \cdot \bar{r} | J, m \rangle \quad (\text{B.5})$$

where $\hat{\epsilon}$ represents the polarisation of the electric field. In order to calculate the dipole matrix elements we expand in polarisation components denoted by $q = 0, \pm 1$, where $q = 0$ corresponds to linear polarised light and $q = \pm 1$ to circular polarised light,

$$\langle J', m' | \hat{\epsilon} \cdot \bar{r} | J, m \rangle = \sum_{q=0,\pm 1} \langle J', m' | r_q | J, m \rangle, \quad (\text{B.6})$$

and calculate the matrix element for a given polarisation of the light using the Wigner-Eckart theorem [150]

$$\begin{aligned} \langle J', m' | r_q | J, m \rangle &= (-1)^{J'-m'} \begin{pmatrix} J' & 1 & J \\ -m' & q & m \end{pmatrix} \langle J' || r || J \rangle \\ &= (-1)^{J'-m'} (-1)^{J'+J+1} \begin{pmatrix} J & 1 & J' \\ m & q & -m' \end{pmatrix} \langle J' || r || J \rangle. \end{aligned} \quad (\text{B.7})$$

where we have used the symmetries of the $3j$ -symbols. The reduced matrix elements are connected to the decay rates [150]

$$\Gamma = \frac{\omega^3 e^2}{3\pi\epsilon_0 \hbar c^3} \frac{1}{2J'+1} |\langle J' || r || J \rangle|^2, \quad (\text{B.8})$$

and the $3j$ -symbol can be rewritten as Clebsch-Gordan coefficients,

$$\begin{pmatrix} J & 1 & J' \\ m & q & -m' \end{pmatrix} = (-1)^{J-1+m'} \frac{1}{\sqrt{2J'+1}} \langle Jm1q | J'm' \rangle. \quad (\text{B.9})$$

Substituting (B.7), (B.8) and (B.9) into (B.5) we find the Rabi frequency for a given polarisation,

$$\begin{aligned} \Omega_q &= \chi \langle Jm1q | J'm' \rangle (-1)^{2J+2J'} \\ &= \chi \langle Jm1q | J'm' \rangle, \end{aligned} \quad (\text{B.10})$$

as a modification of the two-level Rabi frequency. Below we show the Clebsch-Gordan coefficient for selected transitions.

	$m' = -1/2$	$m' = 1/2$
$m = -1/2$	$-\sqrt{1/3}$	$-\sqrt{2/3}$
$m = 1/2$	$\sqrt{2/3}$	$\sqrt{1/3}$

Table B.1: Clebsch-Gordan coefficients for the $S_{1/2}$ - $P_{1/2}$ transition with $J = J' = 1/2$ coupled with the 397 nm laser.

	$m' = -1/2$	$m' = 1/2$
$m = -3/2$	$\sqrt{1/2}$	-
$m = -1/2$	$-\sqrt{1/3}$	$\sqrt{1/6}$
$m = 1/2$	$\sqrt{1/6}$	$-\sqrt{1/3}$
$m = 3/2$	-	$\sqrt{1/2}$

Table B.2: Clebsch-Gordan coefficients for the $D_{3/2}$ - $P_{1/2}$ transition with $J = 3/2$ and $J' = 1/2$ coupled with the 866 nm laser.

	$m' = -3/2$	$m' = -1/2$	$m' = 1/2$	$m' = 3/2$
$m = -3/2$	$-\sqrt{3/5}$	$-\sqrt{2/5}$	-	-
$m = -1/2$	$\sqrt{2/5}$	$-\sqrt{1/15}$	$-\sqrt{8/15}$	-
$m = 1/2$	-	$\sqrt{8/15}$	$\sqrt{1/15}$	$-\sqrt{2/5}$
$m = 3/2$	-	-	$\sqrt{2/5}$	$\sqrt{3/5}$

Table B.3: Clebsch-Gordan coefficients for the $D_{3/2}$ - $P_{3/2}$ transition with $J = J' = 3/2$ coupled with the 850 nm laser.

	$m' = -3/2$	$m' = -1/2$	$m' = 1/2$	$m' = 3/2$
$m = -5/2$	$\sqrt{2/3}$	-	-	-
$m = -3/2$	$-\sqrt{4/15}$	$\sqrt{2/5}$	-	-
$m = -1/2$	$\sqrt{1/15}$	$-\sqrt{2/5}$	$\sqrt{1/5}$	-
$m = 1/2$	-	$\sqrt{1/5}$	$-\sqrt{2/5}$	$\sqrt{1/15}$
$m = 3/2$	-	-	$\sqrt{2/5}$	$-\sqrt{4/15}$
$m = 5/2$	-	-	-	$\sqrt{2/3}$

Table B.4: Clebsch-Gordan coefficients for the $D_{5/2}$ - $P_{3/2}$ transition with $J = 5/2$ and $J' = 3/2$ coupled with the 854 nm laser.

Appendix C

Measurements of laser phase fluctuations

Phase fluctuations of the lasers involved in STIRAP lead to a decay of the coherences and thereby limits the transfer efficiency. The phase fluctuations are measured with a delayed self-heterodyne interferometer as first proposed in [151]. The laser beam is split on a 50/50 beamsplitter, changing the frequency of one beam with an AOM and delaying the other in a fibre. The delay time is nL/c , where L is the fibre length and $n = 1.5$ the typical refraction index for an optical fibre. The two beams are subsequently superimposed in a fibre

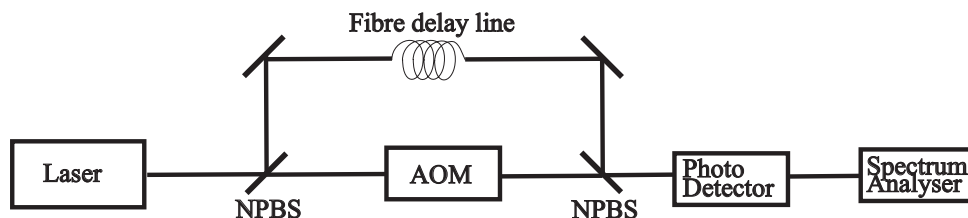


Figure C.1: Setup for measurement of laser phase fluctuations. The laser beam is split on a non-polarising beamsplitter (NPBS). One part pass through an AOM, the other is delayed in a fibre. Subsequently, they are reunited on another non-polarising beamsplitter and the interference beat-note between them is measured.

coupled beamsplitter creating a beat-signal, which is analysed in a spectrum analyser. If two lasers with optical frequencies ω_1 and ω_2 are superimposed on a photodetector a beat-note can be observed at the difference in the optical frequencies of the two laser beams - in our case the frequency change made by the AOM is around 400 MHz.

In our setup both beams have the same source so in order to consider these as two independent laser sources we need to delay one beam beyond the coherence time ($\tau_{coh} = \frac{1}{2\pi\delta\nu}$) of the laser. To make measurements far beyond

the coherence time of the lasers we use a 4.3 km optical fibre¹ corresponding to a $22\mu\text{s}$ delay time. This was done for the 850 nm and 854 nm lasers as shown in Fig. C.2. A fit of the results to a Lorentz distribution yields FWHM of 390 kHz and 208 kHz, respectively, and assuming the laser phase fluctuations are Lorentz-distributed, the FWHM width of the measured beat-notes are twice the FWHM-Lorentz linewidth of the lasers [152,153] yielding linewidths $\delta_{850} = 195$ kHz and $\delta_{854} = 104$ kHz.

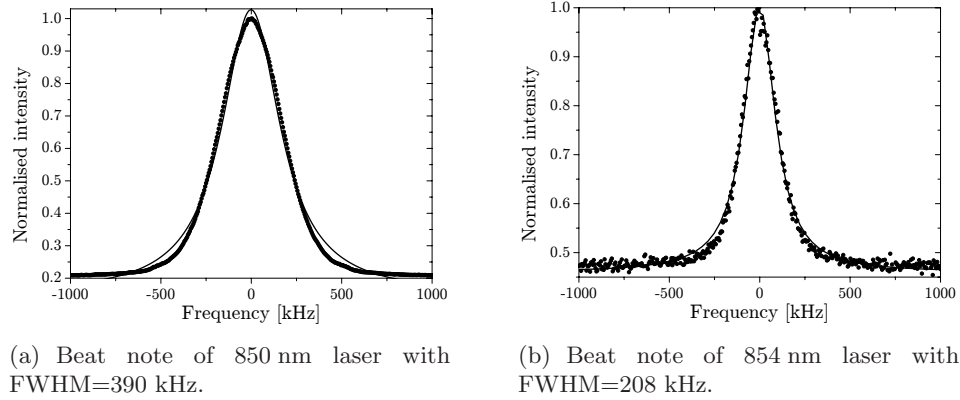
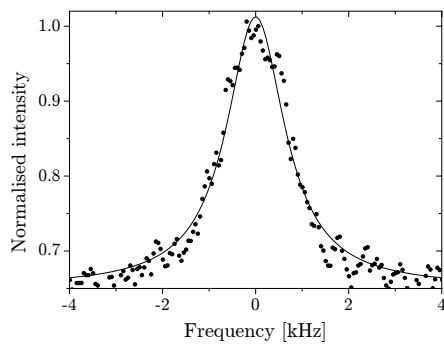


Figure C.2: Linewidth measurements with 4.3 km fibre delay line. Both measurements are assumed to be Lorentzian.

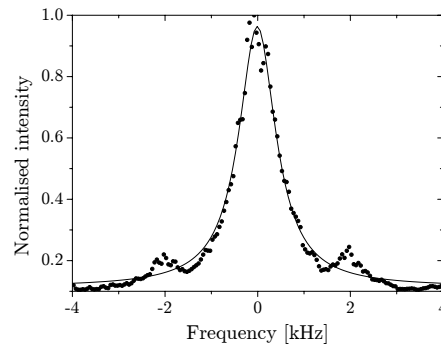
For all four lasers (850 nm, 854 nm, 866 nm and 794 nm, which is frequency doubled to 397 nm), measurements were also done with fibre lengths² 300 m and 518 m corresponding to $1.5\mu\text{s}$ and $2.6\mu\text{s}$ delay between the two beams. This gives us measurements of the dephasing rates due to laser phase fluctuations on the time scales we use in the STIRAP-sequences. In this case the two beams can not be considered independent and the measured phase fluctuations are estimates of the phase fluctuations experienced by the ions during a STIRAP process. The results are shown for all four lasers with a 518 m fibre delay in Fig. C.3 yielding phase fluctuations below 1.5 kHz for all lasers involved in STIRAP - measured as the FWHM of a fit to a Lorentz distribution. For a 300 m delay line the fluctuations are just a little below the 518 m result as shown in the same figure for the 854 nm laser. The measurements of the phase fluctuations are to a good approximation Lorentzian and can therefore be included as decay terms in the off-diagonal density matrix elements as in the simulations presented in chapter 7.4.5.

¹4300 m optical telecom fibre.

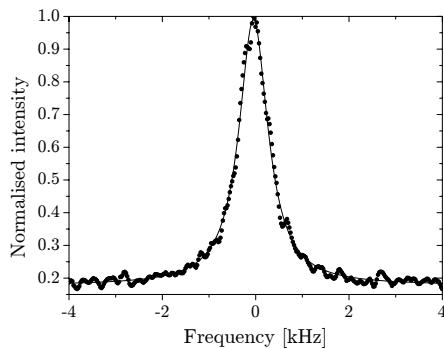
²300 m single mode optical fibre with operating wavelength at 830 nm (sm800-5.6-125 from Thorlabs). The 518 m fibre consists of the 300 m fibre connected with a 218 m telecom fibre single mode at 1089 nm.



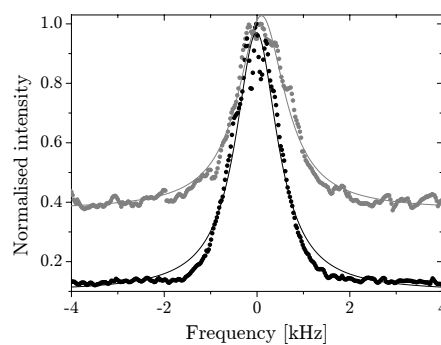
(a) Beat note of 866 nm laser with FWHM=1.5 kHz measured with 518 m fibre delay line.



(b) Beat note of 794 nm laser with FWHM=0.9 kHz measured with 518 m fibre delay line.



(c) Beat note of 866 nm laser with FWHM=0.7 kHz measured with 518 m fibre delay line.



(d) Beat notes of 854 nm laser delayed with 518 m fibre delay line (grey) yielding FWHM=1.2 kHz and 300 m fibre (black) yielding FWHM=1.1 kHz.

Figure C.3: Measurements of phase fluctuations with 300 m and 518 m fibre delay lines. The solid lines are fits to Lorentz distributions.

Bibliography

- [1] R. P. Feynman, *Quantum-Mechanical Computers*, Found. Phys. **16**, 507 (1986).
- [2] P. Benioff, *Quantum-Mechanical Hamiltonian Models of Turing-Machines*, J. Stat. Phys. **29**, 515 (1982).
- [3] L. K. Grover, *Quantum mechanics helps in searching for a needle in a haystack*, Phys. Rev. Lett. **79**, 325 (1997).
- [4] P. W. Shor, *Polynomial-time algorithms for prime factorization and discrete logarithms on a quantum computer*, SIAM J. Comput. **26**, 1484 (1997).
- [5] M. A. Nielsen and I. L. Chuang, *Quantum Computation and Quantum Information* (Cambridge University Press, 2000).
- [6] N. A. Gershenfeld and I. L. Chuang, *Bulk Spin-Resonance Quantum Computation*, Science **275**, 350 (1997).
- [7] L. M. K. Vandersypen and I. L. Chuang, *NMR techniques for quantum control and computation*, Rev. Mod. Phys. **76**, 1037 (2004).
- [8] P. Kok, W. J. Munro, K. Nemoto, T. C. Ralph, J. P. Dowling and G. J. Milburn, *Linear optical quantum computing with photonic qubits*, Rev. Mod. Phys. **79**, 135 (2007).
- [9] H. J. Briegel, T. Calarco, D. Jaksch, J. I. Cirac and P. Zoller, *Quantum computing with neutral atoms*, J. Mod. Optic. **47**, 415 (2000).
- [10] I. H. Deutsch, G. K. Brennen and P. S. Jessen, *Quantum Computing with Neutral Atoms in an Optical Lattice*, Fortschr. Phys. **48**, 925 (2000).
- [11] J. I. Cirac and P. Zoller, *Quantum Computations with Cold Trapped Ions*, Phys. Rev. Lett. **74**, 4091 (1995).
- [12] A. Imamoglu, *Quantum Computation Using Quantum Dot Spins and Microcavities*, Fortschr. Phys. **48**, 987 (2000).

-
- [13] Y. Makhlin, G. Schön and A. Shnirman, *Quantum-state engineering with Josephson-junction devices*, Rev. Mod. Phys. **73**, 357 (2001).
- [14] D. P. DiVincenzo, *The Physical Implementation of Quantum Computation*, Fortschr. Phys. **48**, 771 (2000).
- [15] R. Hughes and T. Heinrichs, *A Quantum Information Science and Technology Roadmap* (2004), http://qist.lanl.gov/qcomp_map.shtml.
- [16] D. J. Griffiths, *Introduction to Quantum Mechanics* (Prentice-Hall, 1995).
- [17] A. Messiah, *Quantum Mechanics*, volume 2 (North-Holland publishing company, 1961).
- [18] M. Born and V. Fock, *Beweis des Adiabatensatzes*, Z. Phys. **51**, 165 (1928).
- [19] M. V. Berry, *Quantal Phase-Factors Accompanying Adiabatic Changes*, Proc. R. Soc. London, Ser. A **392**, 45 (1984).
- [20] J. H. Hannay, *Angle variable holonomy in adiabatic excursion of an integrable Hamiltonian*, J. Phys. A **18**, 221 (1985).
- [21] F. Wilczek and A. Zee, *Appearance of Gauge Structure in Simple Dynamical-Systems*, Phys. Rev. Lett. **52**, 2111 (1984).
- [22] R. G. Unanyan, B. W. Shore and K. Bergmann, *Laser-driven population transfer in four-level atoms: Consequences of non-Abelian geometrical adiabatic phase factors*, Phys. Rev. A **59**, 2910 (1999).
- [23] P. Solinas, P. Zanardi and N. Zanghì, *Robustness of non-Abelian holonomic quantum gates against parametric noise*, Phys. Rev. A **70**, 042316 (2004).
- [24] S.-L. Zhu and P. Zanardi, *Geometric quantum gates that are robust against stochastic control errors*, Phys. Rev. A **72**, 020301 (2005).
- [25] G. De Chiara and G. M. Palma, *Berry Phase for a Spin 1/2 Particle in a Classical Fluctuating Field*, Phys. Rev. Lett. **91**, 090404 (2003).
- [26] A. Nazir, T. P. Spiller and W. J. Munro, *Decoherence of geometric phase gates*, Phys. Rev. A **65**, 042303 (2002).
- [27] P. Zanardi and M. Rasetti, *Holonomic quantum computation*, Phys. Lett. A **264**, 94 (1999).
- [28] L. M. Duan, J. I. Cirac and P. Zoller, *Geometric manipulation of trapped ions for quantum computation*, Science **292**, 1695 (2001).

-
- [29] P. Staantum, *Quantum Optics with Trapped Calcium Ions*, Ph.D. thesis, University of Aarhus (2004).
- [30] A. Sørensen and K. Mølmer, *Entanglement and quantum computation with ions in thermal motion*, Phys. Rev. A **62**, 022311 (2000).
- [31] A. Recati, T. Calarco, P. Zanardi, J. I. Cirac and P. Zoller, *Holonomic quantum computation with neutral atoms*, Phys. Rev. A **66**, 032309 (2002).
- [32] J. Pachos and S. Chountasis, *Optical holonomic quantum computer*, Phys. Rev. A **62**, 052318 (2000).
- [33] J. A. Jones, V. Vedral, A. Ekert and G. Castagnoli, *Geometric quantum computation using nuclear magnetic resonance*, Nature **403**, 869 (2000).
- [34] P. Solinas, P. Zanardi, N. Zanghì and F. Rossi, *Nonadiabatic geometrical quantum gates in semiconductor quantum dots*, Phys. Rev. A **67**, 052309 (2003).
- [35] D. Leibfried, R. Blatt, C. Monroe and D. Wineland, *Quantum dynamics of single trapped ions*, Rev. Mod. Phys. **75**, 281 (2003).
- [36] G. Falci, R. Fazio, G. M. Palma, J. Siewert and V. Vedral, *Detection of geometric phases in superconducting nanocircuits*, Nature **407**, 355 (2000).
- [37] K. Bergmann, H. Theuer and B. W. Shore, *Coherent population transfer among quantum states of atoms and molecules*, Rev. Mod. Phys. **70**, 1003 (1998).
- [38] B. W. Shore, *The Theory of Coherent Atomic Excitation* (Wiley, New York, 1990).
- [39] M. P. Fewell, B. W. Shore and K. Bergmann, *Coherent population transfer among three states: Full algebraic solutions and the relevance of non adiabatic processes to transfer by delayed pulses*, Aust. J. Phys. **50**, 281 (1997).
- [40] U. Gaubatz, P. Rudecki, S. Schiemann and K. Bergmann, *Population Transfer between Molecular Vibrational Levels by Stimulated Raman-Scattering with Partially Overlapping Laserfields - a New Concept and Experimental Results*, J. Chem. Phys. **92**, 5363 (1990).
- [41] D. Jaksch, J. I. Cirac, P. Zoller, S. L. Rolston, R. Côte and M. D. Lukin, *Fast quantum gates for neutral atoms*, Phys. Rev. Lett. **85**, 2208 (2000).

-
- [42] N. Ohlsson, R. K. Mohan and S. Kröll, *Quantum computer hardware based on rare-earth-ion-doped inorganic crystals*, Opt. Commun. **201**, 71 (2002).
- [43] I. Bouchoule and K. Mølmer, *Spin squeezing of atoms by the dipole interaction in virtually excited Rydberg states*, Phys. Rev. A **65**, 041803 (2002).
- [44] D. D. Yavuz, P. B. Kulatunga, E. Urban, T. A. Johnson, N. Proite, T. Henage, T. G. Walker and M. Saffman, *Fast ground state manipulation of neutral atoms in microscopic optical traps*, Phys. Rev. Lett. **96**, 063001 (2006).
- [45] J. Deiglmayr, M. Reetz-Lamour, T. Amthor, S. Westermann, A. L. de Oliveira and M. Weidemüller, *Coherent excitation of Rydberg atoms in an ultracold gas*, Opt. Commun. **264**, 293 (2006).
- [46] F. de Seze, F. Dahes, V. Crozatier, I. Lorgeré, F. Bretenaker and J. L. Le Gouët, *Coherent driving of Tm^{3+} : YAG ions using a complex hyperbolic secant optical field*, Eur. Phys. J. D **33**, 343 (2005).
- [47] H. Goto and K. Ichimura, *Expectation-value approach to photon statistics in cavity QED*, Phys. Rev. A **74**, 069901 (2006).
- [48] E. Sjöqvist, *On geometric phases for quantum trajectories*, Acta Phys. Hung. B **26**, 195 (2006).
- [49] S. Dasgupta and D. A. Lidar, *Decoherence-induced geometric phase in a multilevel atomic system*, J. Phys. B **40**, S127 (2007).
- [50] A. Carollo, I. Fuentes-Guridi, M. F. Santos and V. Vedral, *Geometric Phase in Open Systems*, Phys. Rev. Lett. **90**, 160402 (2003).
- [51] K. Mølmer, Y. Castin and J. Dalibard, *Monte-Carlo Wave-Function Method in Quantum Optics*, J. Opt. Soc. Am. B **10**, 524 (1993).
- [52] K. Mølmer and Y. Castin, *Monte Carlo wavefunctions in quantum optics*, Quantum Semiclass. Opt. **8**, 49 (1996).
- [53] S. Haroche and J.-M. Raimond, *Exploring the Quantum* (Oxford University Press, Oxford, 2006), chapter 4.
- [54] J. C. Garrison and E. M. Wright, *Complex Geometrical Phases for Dissipative Systems*, Phys. Lett. A **128**, 177 (1988).
- [55] F. H. M. Faisal, *Theory of multiphoton processes* (Plenum Press, New York, 1987), chapter 11.2.

-
- [56] A. Uhlmann, *The "transition probability" in the state space of a^* -algebra*, Rep. Math. Phys. **9**, 273 (1976).
- [57] M. D. Bowdrey, D. K. L. Oi, A. J. Short, K. Banaszek and J. A. Jones, *Fidelity of single qubit maps*, Phys. Lett. A **294**, 258 (2002).
- [58] T. F. Gallagher, *Rydberg atoms* (University Press, Cambridge, 1994).
- [59] R. Dumke, M. Volk, T. Mütther, F. B. J. Buchkremer, G. Birkl and W. Ertmer, *Micro-optical Realization of Arrays of Selectively Addressable Dipole Traps: A Scalable Configuration for Quantum Computation with Atomic Qubits*, Phys. Rev. Lett. **89**, 097903 (2002).
- [60] J. Beugnon, C. Tuchendler, H. Marion, A. Gaëtan, Y. Miroshnychenko, Y. R. P. Sortais, A. M. Lance, M. P. A. Jones, G. Messin, A. Browaeys and P. Grangier, *Two-dimensional transport and transfer of a single atomic qubit in optical tweezers*, Nat. Phys. **3**, 696 (2007).
- [61] M. P. A. Jones, J. Beugnon, A. Gaëtan, J. Zhang, G. Messin, A. Browaeys and P. Grangier, *Fast quantum state control of a single trapped neutral atom*, Phys. Rev. A **75**, 040301 (2007).
- [62] T. A. Johnson, E. Urban, T. Henage, L. Isenhower, D. D. Yavuz, T. G. Walker and M. Saffman, *Rabi Oscillations between Ground and Rydberg States with Dipole-Dipole Atomic Interactions*, Phys. Rev. Lett. **100**, 113003 (2008).
- [63] M. Saffman, *Private communication* (2008).
- [64] M. D. Lukin, M. Fleischhauer, R. Côte, L. M. Duan, D. Jaksch, J. I. Cirac and P. Zoller, *Dipole Blockade and Quantum Information Processing in Mesoscopic Atomic Ensembles*, Phys. Rev. Lett. **87**, 037901 (2001).
- [65] M. Saffman and T. G. Walker, *Analysis of a quantum logic device based on dipole-dipole interactions of optically trapped Rydberg atoms*, Phys. Rev. A **72**, 022347 (2005).
- [66] T. G. Walker and M. Saffman, *Consequences of Zeeman degeneracy for the van der Waals blockade between Rydberg atoms*, Phys. Rev. A **77**, 032723 (2008).
- [67] I. E. Protsenko, G. Reymond, N. Schlosser and P. Grangier, *Operation of a quantum phase gate using neutral atoms in microscopic dipole traps*, Phys. Rev. A **65**, 052301 (2002).
- [68] E. Brion, K. Mølmer and M. Saffman, *Quantum Computing with Collective Ensembles of Multilevel Systems*, Phys. Rev. Lett. **99**, 260501 (2007).

- [69] D. Tong, S. M. Farooqi, J. Stanojevic, S. Krishnan, Y. P. Zhang, R. Côté, E. E. Eyler and P. L. Gould, *Local Blockade of Rydberg Excitation in an Ultracold Gas*, Phys. Rev. Lett. **93**, 063001 (2004).
- [70] K. Singer, M. Reetz-Lamour, T. Amthor, L. G. Marcassa and M. Weidemüller, *Suppression of Excitation and Spectral Broadening Induced by Interactions in a Cold Gas of Rydberg Atoms*, Phys. Rev. Lett. **93**, 163001 (2004).
- [71] R. Heidemann, U. Raitzsch, V. Bendkowsky, B. Butscher, R. Löw, L. Santos and T. Pfau, *Evidence for coherent collective Rydberg excitation in the strong blockade regime*, Phys. Rev. Lett. **99**, 163601 (2007).
- [72] F. W. Cummings, *Stimulated Emission of Radiation in a Single Mode*, Phys. Rev. **140**, A1051 (1965).
- [73] A. Auffeves, P. Maioli, T. Meunier, S. Gleyzes, G. Nogues, M. Brune, J. M. Raimond and S. Haroche, *Entanglement of a Mesoscopic Field with an Atom Induced by Photon Graininess in a Cavity*, Phys. Rev. Lett. **91**, 230405 (2003).
- [74] D. M. Meekhof, C. Monroe, B. E. King, W. M. Itano and D. J. Wineland, *Generation of Nonclassical Motional States of a Trapped Atom*, Phys. Rev. Lett. **76**, 1796 (1996).
- [75] D. Leibfried, D. M. Meekhof, B. E. King, C. Monroe, W. M. Itano and D. J. Wineland, *Experimental Determination of the Motional Quantum State of a Trapped Atom*, Phys. Rev. Lett. **77**, 4281 (1996).
- [76] M. J. Holland and K. Burnett, *Interferometric Detection of Optical-Phase Shifts at the Heisenberg Limit*, Phys. Rev. Lett. **71**, 1355 (1993).
- [77] P. Bouyer and M. A. Kasevich, *Heisenberg-limited spectroscopy with degenerate Bose-Einstein gases*, Phys. Rev. A **56**, R1083 (1997).
- [78] B. Yurke and D. Stoler, *Generating quantum mechanical superpositions of macroscopically distinguishable states via amplitude dispersion*, Phys. Rev. Lett. **57**, 13 (1986).
- [79] D. Greenberger, M. Horne and A. Zeilinger, *Bell's theorem, Quantum Theory, and Conceptions of the Universe* (Kluwer Academics, Dordrecht, The Netherlands, 1989), pp. 73-76.
- [80] A. Kreuter, C. Becher, G. P. T. Lancaster, A. B. Mundt, C. Russo, H. Häffner, C. Roos, W. Hänsel, F. Schmidt-Kaler, R. Blatt and M. S. Safronova, *Experimental and theoretical study of the $3d^2D$ -level lifetimes of $^{40}\text{Ca}^+$* , Phys. Rev. A **71**, 032504 (2005).

- [81] H. C. Nägerl, C. Roos, D. Leibfried, H. Rohde, G. Thalhammer, J. Eschner, F. Schmidt-Kaler and R. Blatt, *Investigating a qubit candidate: Spectroscopy on the $S_{1/2}$ to $D_{5/2}$ transition of a trapped calcium ion in a linear Paul trap*, Phys. Rev. A **61**, 023405 (2000).
- [82] C. Monroe, D. M. Meekhof, B. E. King, W. M. Itano and D. J. Wineland, *Demonstration of a Fundamental Quantum Logic Gate*, Phys. Rev. Lett. **75**, 4714 (1995).
- [83] L. Deslauriers, P. C. Haljan, P. J. Lee, K. A. Brickman, B. B. Blinov, M. J. Madsen and C. Monroe, *Zero-point cooling and low heating of trapped $^{111}\text{Cd}^+$ ions*, Phys. Rev. A **70**, 043408 (2004).
- [84] J. Benhelm, G. Kirchmair, U. Rapol, T. Körber, C. F. Roos and R. Blatt, *Measurement of the hyperfine structure of the $S_{1/2} - D_{5/2}$ transition in $^{43}\text{Ca}^+$* , Phys. Rev. A **75**, 032506 (2007).
- [85] D. M. Lucas, B. C. Keitch, J. P. Home, G. Imreh, M. J. McDonnell, D. N. Stacey, D. J. Szwer and A. M. Steane, *A long-lived memory qubit on a low-decoherence quantum bus*, arXiv: quant-ph/0710.4421v1 (2008).
- [86] R. J. Hughes, D. F. V. James, E. H. Knill, R. Laflamme and A. G. Petschek, *Decoherence Bounds on Quantum Computation with Trapped Ions*, Phys. Rev. Lett. **77**, 3240 (1996).
- [87] D. Leibfried, E. Knill, S. Seidelin, J. Britton, R. B. Blakestad, J. Chiaverini, D. B. Hume, W. M. Itano, J. D. Jost, C. Langer, R. Ozeri, R. Reichle and D. J. Wineland, *Creation of a six-atom ‘Schrödinger cat’ state*, Nature **438**, 639 (2005).
- [88] H. Häffner, W. Hänsel, C. F. Roos, J. Benhelm, D. Chek-al kar, M. Chwalla, T. Körber, U. D. Rapol, M. Riebe, P. O. Schmidt, C. Becher, O. Gühne, W. Dür and R. Blatt, *Scalable multiparticle entanglement of trapped ions*, Nature **438**, 643 (2005).
- [89] D. Kielpinski, C. Monroe and D. J. Wineland, *Architecture for a large-scale ion-trap quantum computer*, Nature **417**, 709 (2002).
- [90] D. Hucul, M. Yeo, W. Hensinger, J. Rabchuk, S. Olmschenk and C. Monroe, *On the Transport of Atomic Ions in Linear and Multidimensional Ion Trap Arrays*, arXiv:quant-ph/0702175v3 (2007).
- [91] W. K. Hensinger, S. Olmschenk, D. Stick, D. Hucul, M. Yeo, M. Acton, L. Deslauriers, C. Monroe and J. Rabchuk, *T-junction ion trap array for two-dimensional ion shuttling, storage, and manipulation*, Appl. Phys. Lett. **88**, 034101 (2006).

- [92] H. C. Nägerl, D. Leibfried, H. Rohde, G. Thalhammer, J. Eschner, F. Schmidt-Kaler and R. Blatt, *Laser addressing of individual ions in a linear ion trap*, Phys. Rev. A **60**, 145 (1999).
- [93] A. Sørensen and K. Mølmer, *Quantum Computation with Ions in Thermal Motion*, Phys. Rev. Lett. **82**, 1971 (1999).
- [94] C. A. Sackett, D. Kielpinski, B. E. King, C. Langer, V. Meyer, C. J. Myatt, M. Rowe, Q. A. Turchette, W. M. Itano, D. J. Wineland and I. C. Monroe, *Experimental entanglement of four particles*, Nature **404**, 256 (2000).
- [95] F. Schmidt-Kaler, H. Häffner, M. Riebe, S. Gulde, G. P. T. Lancaster, T. Deuschle, C. Becher, C. F. Roos, J. Eschner and R. Blatt, *Realization of the Cirac-Zoller controlled-NOT quantum gate*, Nature **422**, 408 (2003).
- [96] D. Leibfried, B. DeMarco, V. Meyer, D. Lucas, M. Barrett, J. Britton, W. M. Itano, B. Jelenkovic, C. Langer, T. Rosenband and D. J. Wineland, *Experimental demonstration of a robust, high-fidelity geometric two ion-qubit phase gate*, Nature **422**, 412 (2003).
- [97] J. Benhelm, G. Kirchmair, C. F. Roos and R. Blatt, *Towards fault-tolerant quantum computing with trapped ions*, Nature Physics **4** (2008).
- [98] A. M. Steane, *Efficient fault-tolerant quantum computing*, Nature **399**, 124 (1999).
- [99] E. Knill, *Quantum computing with realistically noisy devices*, Nature **434**, 39 (2005).
- [100] K. A. Brickman, P. C. Haljan, P. J. Lee, M. Acton, L. Deslauriers and C. Monroe, *Implementation of Grover's quantum search algorithm in a scalable system*, Phys. Rev. A **72**, 050306 (2005).
- [101] S. Gulde, M. Riebe, G. P. T. Lancaster, C. Becher, J. Eschner, H. Häffner, F. Schmidt-Kaler, I. L. Chuang and R. Blatt, *Implementation of the Deutsch-Jozsa algorithm on an ion-trap quantum computer*, Nature **421**, 48 (2003).
- [102] J. Chiaverini, J. Britton, D. Leibfried, E. Knill, M. D. Barrett, R. B. Blakestad, W. M. Itano, J. D. Jost, C. Langer, R. Ozeri, T. Schaetz and D. J. Wineland, *Implementation of the Semiclassical Quantum Fourier Transform in a Scalable System*, Science **308**, 997 (2005).
- [103] D. Kielpinski, V. Meyer, M. A. Rowe, C. A. Sackett, W. M. Itano, C. Monroe and D. J. Wineland, *A Decoherence-Free Quantum Memory Using Trapped Ions*, Science **291**, 1013 (2001).

- [104] H. Häffner, F. Schmidt-Kaler, W. Hänsel, C. F. Roos, T. Körber, M. Chwalla, M. Riebe, J. Benhelm, U. D. Rapol, C. Becher and R. Blatt, *Robust entanglement*, Appl. Phys. B **81**, 151 (2005).
- [105] C. Langer, R. Ozeri, J. D. Jost, J. Chiaverini, B. DeMarco, A. Ben-Kish, R. B. Blakestad, J. Britton, D. B. Hume, W. M. Itano, D. Leibfried, R. Reichle, T. Rosenband, T. Schaetz, P. O. Schmidt and D. J. Wineland, *Long-Lived Qubit Memory Using Atomic Ions*, Phys. Rev. Lett. **95**, 060502 (2005).
- [106] M. J. McDonnell, J. P. Stacey, S. C. Webster, J. P. Home, A. Ramos, D. M. Lucas, D. N. Stacey and A. M. Steane, *High-Efficiency Detection of a Single Quantum of Angular Momentum by Suppression of Optical Pumping*, Phys. Rev. Lett. **93**, 153601 (2004).
- [107] P. K. Ghosh, *Ion Traps* (Oxford University Press Inc., New York, 1995).
- [108] H. J. Metcalf and P. Straten, *Laser Cooling and Trapping* (Springer, 2002).
- [109] R. J. Hendricks, J. L. Sørensen, C. Champenois, M. Knoop and M. Drewsen, *Doppler cooling of calcium ions using a dipole-forbidden transition*, Phys. Rev. A **77**, 021401 (2008).
- [110] D. F. V. James, *Quantum dynamics of cold trapped ions with application to quantum computation*, Appl. Phys. B **66**, 181 (1998).
- [111] D. Wineland and H. Dehmelt, *Proposed 1014 Delta Upsilon Less Than Upsilon Laser Fluorescence Spectroscopy on T1+ Mono-Ion Oscillator Iii*, Bull. Am. Phys. Soc. **20**, 637 (1975).
- [112] F. Diedrich, J. C. Bergquist, W. M. Itano and D. J. Wineland, *Laser Cooling to the Zero-Point Energy of Motion*, Phys. Rev. Lett. **62**, 403 (1989).
- [113] C. Roos, T. Zeiger, H. Rohde, H. C. Nägerl, J. Eschner, D. Leibfried, F. Schmidt-Kaler and R. Blatt, *Quantum State Engineering on an Optical Transition and Decoherence in a Paul Trap*, Phys. Rev. Lett. **83**, 4713 (1999).
- [114] E. Peik, J. Abel, T. Becker, J. von Zanthier and H. Walther, *Sideband cooling of ions in radio-frequency traps*, Phys. Rev. A **60**, 439 (1999).
- [115] C. Monroe, D. M. Meekhof, B. E. King, S. R. Jefferts, W. M. Itano, D. J. Wineland and P. Gould, *Resolved-Sideband Raman Cooling of a Bound Atom to the 3D Zero-Point Energy*, Phys. Rev. Lett. **75**, 4011 (1995).

- [116] S. Webster, *Raman Sideband Cooling and Coherent Manipulation of Trapped Ions*, Ph.D. thesis, Oxford University (2005).
- [117] G. Morigi, J. Eschner and C. H. Keitel, *Ground State Laser Cooling Using Electromagnetically Induced Transparency*, Phys. Rev. Lett. **85**, 4458 (2000).
- [118] C. F. Roos, D. Leibfried, A. Mundt, F. Schmidt-Kaler, J. Eschner and R. Blatt, *Experimental Demonstration of Ground State Laser Cooling with Electromagnetically Induced Transparency*, Phys. Rev. Lett. **85**, 5547 (2000).
- [119] F. Schmidt-Kaler, J. Eschner, G. Morigi, C. F. Roos, D. Leibfried, A. Mundt and R. Blatt, *Laser cooling with electromagnetically induced transparency: application to trapped samples of ions or neutral atoms*, Appl. Phys. B **73**, 807 (2001).
- [120] D. J. Larson, J. C. Bergquist, J. J. Bollinger, W. M. Itano and D. J. Wineland, *Sympathetic Cooling of Trapped Ions - a Laser-Cooled 2-Species Nonneutral Ion Plasma*, Phys. Rev. Lett. **57**, 70 (1986).
- [121] D. Kielpinski, B. E. King, C. J. Myatt, C. A. Sackett, Q. A. Turchette, W. M. Itano, C. Monroe, D. J. Wineland and W. H. Zurek, *Sympathetic cooling of trapped ions for quantum logic*, Phys. Rev. A **61**, 032310 (2000).
- [122] M. D. Barrett, B. DeMarco, T. Schaetz, V. Meyer, D. Leibfried, J. Britton, J. Chiaverini, W. M. Itano, B. Jelenković, J. D. Jost, C. Langer, T. Rosenband and D. J. Wineland, *Sympathetic cooling of $^9\text{Be}^+$ and $^{24}\text{Mg}^+$ for quantum logic*, Phys. Rev. A **68**, 042302 (2003).
- [123] B. B. Blinov, L. Deslauriers, P. Lee, M. J. Madsen, R. Miller and C. Monroe, *Sympathetic cooling of trapped Cd^+ isotopes*, Phys. Rev. A **65**, 040304 (2002).
- [124] N. Kjærgaard, L. Hornekær, A. M. Thommesen, Z. Videsen and M. Drewsen, *Isotope selective loading of an ion trap using resonance-enhanced two-photon ionization*, Appl. Phys. B **71**, 207 (2000).
- [125] S. Gulde, D. Rotter, P. Barton, F. Schmidt-Kaler, R. Blatt and W. Hogervorst, *Simple and efficient photo-ionization loading of ions for precision ion-trapping experiments*, Appl. Phys. B **73**, 861 (2001).
- [126] J. L. Hall and S. A. Lee, *Interferometric real-time display of cw dye laser wavelength with sub-Doppler accuracy*, Appl. Phys. Lett. **29**, 367 (1976).
- [127] R. Ohmukai, M. Watanabe, H. Imajo, K. Hayasaka and S. Urabe, *Doppler-Free Optogalvanic Spectroscopy of Ca^+ and Ca* , Japan. J. Appl. Phys. **33**, 311 (1994).

- [128] C. D. Bruun, *Effektiv anden harmonisk generation i ekstern kavitet*, Master thesis, University of Aarhus (1998).
- [129] T. W. Hansch and B. Couillaud, *Laser frequency stabilization by polarization spectroscopy of a reflecting reference cavity*, Opt. Commun. **35**, 441 (1980).
- [130] R. W. P. Drever, J. L. Hall, F. V. Kowalski, J. Hough, G. M. Ford, A. J. Munley and H. Ward, *Laser Phase and Frequency Stabilization Using an Optical-Resonator*, Appl. Phys. B **31**, 97 (1983).
- [131] F. K. Jensen, *Laser Frequency Stabilization for use in STIRAP Experiments*, Master thesis, University of Aarhus (2004).
- [132] P. Herskind, J. Lindballe, C. Clausen, J. L. Sørensen and M. Drewsen, *Second-harmonic generation of light at 544 and 272 nm from an ytterbium-doped distributed-feedback fiber laser*, Opt. Lett. **32**, 268 (2007).
- [133] P. A. Ivanov, N. V. Vitanov and K. Bergmann, *Effect of dephasing on stimulated Raman adiabatic passage*, Phys. Rev. A **70**, 063409 (2004).
- [134] J. D. Prestage, G. J. Dick and L. Maleki, *New ion trap for frequency standard applications*, J. Appl. Phys. **66**, 1013 (1989).
- [135] W. Paul, *Electromagnetic traps for charged and neutral particles*, Rev. Mod. Phys. **62**, 531 (1990).
- [136] D. J. Wineland, J. C. Bergquist, W. M. Itano, J. J. Bollinger and C. H. Manney, *Atomic-Ion Coulomb Clusters in an Ion Trap*, Phys. Rev. Lett. **59**, 2935 (1987).
- [137] F. Diedrich, E. Peik, J. M. Chen, W. Quint and H. Walther, *Observation of a Phase Transition of Stored Laser-Cooled Ions*, Phys. Rev. Lett. **59**, 2931 (1987).
- [138] M. Drewsen, C. Brodersen, L. Hornekær, J. S. Hangst and J. P. Schifffer, *Large Ion Crystals in a Linear Paul Trap*, Phys. Rev. Lett. **81**, 2878 (1998).
- [139] D. Stick, W. K. Hensinger, S. Olmschenk, M. J. Madsen, K. Schwab and C. Monroe, *Ion trap in a semiconductor chip*, Nat. Phys. **2**, 36 (2006).
- [140] S. Seidelin, J. Chiaverini, R. Reichle, J. J. Bollinger, D. Leibfried, J. Britton, J. H. Wesenberg, R. B. Blakestad, R. J. Epstein, D. B. Hume, W. M. Itano, J. D. Jost, C. Langer, R. Ozeri, N. Shiga and D. J. Wineland, *Microfabricated Surface-Electrode Ion Trap for Scalable Quantum Information Processing*, Phys. Rev. Lett. **96**, 253003 (2006).

-
- [141] C. J. Foot, *Atomic Physics* (Oxford University Press, New York, 2005).
- [142] C. A. Schrama, E. Peik, W. W. Smith and H. Walther, *Novel miniature ion traps*, Opt. Commun. **101**, 32 (1993).
- [143] M. Abramowitz and I. A. Stegun, *Handbook of Mathematical Functions* (Dover Publications, New York, 1965), 9th edition.
- [144] M. Drewsen and A. Brøner, *Harmonic linear Paul trap: Stability diagram and effective potentials*, Phys. Rev. A **62**, 045401 (2000).
- [145] A. Brøner, *Molekylær dynamiske simulationer af få-ion Coulomb krystaller i radiofrekvente fælder*, Master thesis, University of Aarhus (2000).
- [146] D. J. Berkeland, J. D. Miller, J. C. Bergquist, W. M. Itano and D. J. Wineland, *Minimization of ion micromotion in a Paul trap*, J. Appl. Phys. **83**, 5025 (1998).
- [147] B. Broers, H. B. van Linden van den Heuvell and L. D. Noordam, *Efficient population transfer in a three-level ladder system by frequency-swept ultrashort laser pulses*, Phys. Rev. Lett. **69**, 2062 (1992).
- [148] T. Cubel, B. K. Teo, V. S. Malinovsky, J. R. Guest, A. Reinhard, B. Knuffman, P. R. Berman and G. Raithel, *Coherent population transfer of ground-state atoms into Rydberg states*, Phys. Rev. A **72**, 023405 (2005).
- [149] T. Haslwanter, H. Ritsch, J. Cooper and P. Zoller, *Laser-noise-induced population fluctuations in two- and three-level systems*, Phys. Rev. A **38**, 5652 (1988).
- [150] I. I. Sobelman, *Atomic Spectra and Radiative Transitions* (Springer, 1992), 2nd edition.
- [151] T. Okoshi, K. Kikuchi and A. Nakayama, *Novel Method for High-Resolution Measurement of Laser Output Spectrum*, Electron. Lett. **16**, 630 (1980).
- [152] M. Han and A. Wang, *Analysis of a loss-compensated recirculating delayed self-heterodyne interferometer for laser linewidth measurement*, Appl. Phys. B **81**, 53 (2005).
- [153] P. B. Gallion and G. Debarge, *Quantum Phase Noise and Field Correlation in Single Frequency Semiconductor-Laser Systems*, IEEE J. Quantum Electron. **20**, 343 (1984).